The Pennsylvania State University

The Graduate School

CTENOPHORE SWIMMING: UNDERSTANDING METACHRONAL ROWING AT MILLIMETER SCALES

A Dissertation in

Mechanical Engineering

by

Adrian Herrera-Amaya

Submitted in Partial Fulfillment
of the Requirements
for the Degree of

Doctor of Philosophy

August 2023

The dissertation of Adrian Herrera-Amaya was reviewed and approved by the following:

Margaret L. Byron
Assistant Professor of Mechanical Engineering
Dissertation Advisor
Chair of Committee

Robert Kunz
Professor of Mechanical Engineering
Chair of the Graduate Program

Bo Cheng
Associate Professor of Mechanical Engineering

Timothy J. Jegla
Associate Professor of Biology

ABSTRACT

The hydrodynamics of swimming at the millimeter-to-centimeter scale often present the challenge of having both viscous and inertial effects playing nontrivial roles. Inertial forces arise from the momentum of a moving fluid, while viscous forces come from friction within the flow. The non-dimensional Reynolds number (Re) compares the magnitudes of the inertial and viscous forces within a flow. At low Re ($\ll 1$), viscous forces dominate; at higher Re ($\gg 1$), inertial forces are more important. Efforts to understand the hydrodynamics of swimming have mainly focused on the extremes of fully viscous-dominated ($Re \ll 1$) or inertia-dominated flow ($Re \gg 1$). However, many animals swim in an intermediate regime, where inertia and viscosity are both significant. As an impactful and generalizable case study, we focus on ctenophores (comb jellies), a type of marine zooplankton. Ctenophores swim *via* the coordinated rowing of numerous highly flexible appendages (ctenes), with Reynolds numbers on the order of 10-100. Their locomotory dynamics present a unique opportunity to study the scaling of rowing (drag-based propulsion) across the low to intermediate Reynolds number range. With a combination of animal experiments, reduced-order analytical modeling, and physical-robotic modeling, we investigate how the kinematic and geometric variables of beating ctenes vary across Re, and how they affect swimming (including force production, speed, and maneuverability). Using animal experiments, we quantify the spatiotemporal asymmetry of beating ctenes across a wide range of animal sizes and Re. With our reduced-order model—the first to incorporate adequate formulations for the viscous-inertial nature of this regime—we explore the maneuverability and agility displayed by ctenophores, and show that by controlling the kinematics of their distributed appendages, ctenophores are capable of nearly omnidirectional swimming. Finally, we use a compliant robotic model that mimics ctenophore rowing kinematics to study rowing performance with direct calculation of thrust and lift forces distributed along the propulsor. These experiments shed new light on the relationship between motion asymmetries and thrust and lift production. This combination of animal experiments, analytical modeling, and physical modeling is the most detailed study of low to intermediate Re rowing to date, and provides a foundation for future applications in bio-inspired design.

TABLE OF CONTENTS

LIST OF FIGURES

LIST OF TABLES

ACKNOWLEDGEMENTS

I would like to express my sincere gratitude to everyone who has supported me throughout my journey of completing this dissertation. First and foremost, I would like to thank my advisor for her invaluable guidance and encouragement. I would also like to extend my thanks to the members of my committee for their time and effort in reviewing my work and providing insightful feedback. I feel honored to have such prestigious researchers as members of my doctoral committee.

I am grateful to my colleagues and friends who have supported me throughout this process. Their encouragement and motivation have been instrumental in keeping me focused and motivated. Finally, I would like to thank my family for their love and support. Their unwavering encouragement and belief in me have been a constant source of inspiration. In conclusion, I am grateful to all those who have contributed to the completion of this dissertation. Your support has been invaluable, and I could not have done it without you.

This material is based upon work supported by the National Science Foundation, CONAHCYT, and the National Academies Keck Futures Initiative under the award numbers NSF CBET-2120689, 2019-000021-01EXTF-00633, and DBS5. Any opinions, findings, and conclusions or recommendations expressed in this publication are those of the author(s) and do not necessarily reflect the views of the National Science Foundation, CONAHCYT, and the National Academies Keck Futures Initiative.

Chapter 1

Introduction

1.1 Motivation: rowing at intermediate Reynolds numbers

One of the most notable parameters in fluid mechanics is the Reynolds number (Re), which appears across virtually all problems and is often a centerpiece for swimming studies. The Reynolds number is a nondimensional grouping of variables that compares the magnitudes of the inertial and viscous forces within a flow. The Reynolds number is defined as $Re = Ul/\upsilon$, where the numerator (characteristic speed and length of the flow) quantifies the inertial forces and denominator (kinematic viscosity) the viscous forces. The inertial forces are associated with the momentum of a moving fluid, while the viscous forces arise from the fluid's resistance to being sheared. In simple terms, inertia keeps the fluid moving; viscosity brings it to a stop. This interplay has strong implications for the nature of a given flow; for example, high inertial forces (relative to viscous forces) can trigger the development of turbulence (chaotic vortices or eddies) because they will overwhelm the ability of viscosity to damp out perturbations. In a highly viscous environment, sharp gradients in fluid momentum are quickly smoothed. At low Re (<1), viscous forces dominate; at higher Re, inertial forces take on more importance. Efforts to understand the physics of swimming have mainly focused on the extremes of fully viscous-dominated or inertia-dominated flow. However, many animals swim at intermediate Re, where both inertia and viscosity are important. We can roughly separate these animals into two categories based on their propulsion mechanism: those that use whole-body motions to swim (Costello et al., 2015; Gemmell et al., 2015; Jastrebsky et al., 2016; Webb & Fairchild, 2001) and those that use oscillating propulsors (Fish & Nicastro, 2003; Karakas et al., 2018; Murphy et al., 2016; Sutherland et al., 2014). In this work, we consider the second category—oscillating propulsors which can produce both drag and lift as contributions to overall thrust.

Drag- and lift-based thrust are achieved depending on the motion of the propulsor relative to the animal's body. Rowing happens when the propulsor moves back and forth primarily along an axis aligned with the progression axis (swimming direction); this is the "drag-based swimming" case (Figure 1-1A). For this reciprocal motion to produce net thrust, the power stroke and the recovery stroke must be asymmetric in either space or time (so that there is a drag imbalance). When this reciprocal action primarily creates forces directed parallel to the direction of motion, the propulsor is known as a paddle. In contrast, thrust can also be generated by the reciprocal motion of a propulsor moving primarily orthogonally to the progression axis (Figure 1-1B). In this case, the propulsors are known as hydrofoils and must rotate to maintain a lift-generating angle of attack ("lift-based swimming"). For animals swimming at very low Re (<1), drag-based rowing is the only option since the circulation needed to create lift is difficult to achieve in this viscous-dominated regime (Walker & Westneat, 2000). Lift-based swimming appears at Re as low as 300 in animals such as *Cuvierina atlantica*, a pteropod whose motion resembles that of tiny flying insects (Karakas et al., 2020). We are interested in studying rowing through the spectrum of low to intermediate Re and will therefore focus on drag-based rowing mechanisms.

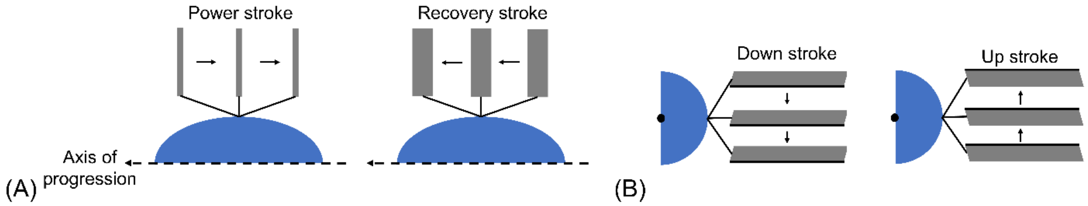

Figure **1-1.** Simplified schematic of the reciprocal motion of a paddle (drag-based) *vs.* a hydrofoil (lift-based). (A) Top view of drag-based propulsion (*i.e.,* rowing), where the asymmetry between power and recovery strokes is represented by the rotation of the rectangular paddle (increasing the flow-normal area on the power stroke relative to the recovery stroke). (B) Front view of lift-based propulsion, with the axis of progression pointing out of the page. The leading edge (black line) motion shows that lift-based propulsors must rotate over the stroke cycle to maintain a lift-generating angle of attack.

The simplest rowers are animals that use only one paddle or a single pair of opposing paddles. This configuration is efficient for accelerating from rest, but imposes a limit on the maximum speed of the animal: the animal cannot swim faster than the speed of its paddles (Vogel, 1994). This velocity restriction is one reason why drag-based rowers tend to have multiple appendages and metachronal coordination, strategies that increase speed and/or maneuverability. By "metachronal coordination," we refer to the movement of fluid via the sequential, coordinated motion of a row or carpet of closely spaced appendages (Barlow et al., 1993; Caldwell et al., 2012; J. L. Lim & DeMont, 2009; Murphy et al., 2011). This swimming strategy maintains a phase lag between adjacent paddles, which creates a "metachronal wave" traveling through the appendage row (see section 1.2). This behavior, classically exemplified by cilia ($Re{\sim}10^{-2}$) (Brennen & Winet, 1977), occurs in a variety of organisms at Re up to several thousand for large shrimp or krill, which metachronally coordinate their legs and pleopods to swim (J. L. Lim & DeMont, 2009). In this work, we study ctenophores, a group of gelatinous marine zooplankton that are the world's largest animals to swim using cilia (Tamm, 2014). In ctenophores, thousands of millimeter-long cilia are bundled into an appendage known as a ctene (Figure 1-2A). Ctenes are spaced in rows along the body of the ctenophore, and metachronally coordinated to produce flows for swimming and feeding (Tamm, 1980). Ctenes have a Re of 10-200, making them an ideal candidate to bridge the knowledge gap between the low and intermediate Re regimes for metachronal swimming and drag-based propulsion.

Ctenophores also exhibit remarkable three-dimensional locomotion, driven *via* eight rows of paddles (instead of the one or two rows found in crustaceans and other organisms that use metachronal locomotion). The coordination between ctene rows allows ctenophores to turn tightly around many axes. This is not the case for all swimmers: animals that rely on paired appendages or a single row of appendages tend to display maximum turning performance around a single axis, depending on the appendages' positions along the body (Murphy et al., 2016; Niimoto et al., 2020; Webb & Fairchild, 2001). Some swimmers exploit the flexibility of their bodies to turn, but these usually have anisotropic bending characteristics and thus have a preferential turning direction (Dabiri et al., 2020; Jastrebsky et al., 2016). Only a few animals have completely axisymmetric bending characteristics; jellyfish are one example (Gemmell et al., 2015). However, the single-jet propulsion used by jellyfish medusae has a notable disadvantage: an animal cannot easily reverse its swimming direction with this strategy. Ctenophores, by contrast, can quickly switch their swimming direction by reversing the power stroke direction of their ctenes (Mackie et al., 1992).

The implications of our study of ctenophore rowing can be broadly categorized into biological and technological. Elucidating the role of hydrodynamic forces at this scale can help us understand crucial animal behaviors like swimming or feeding (Colin et al., 2010; Kiørboe et al., 2014). This work also has the potential to identify physical-mechanical constraints on the evolution and development of ciliary arrays. Ctenophores are, evolutionary speaking, among the oldest animals on the planet (Li et al., 2020; Moroz et al., 2014; Whelan et al., 2017); they are likely the sister group for all other animals (Schultz et al., 2023) . Further knowledge of their swimming mechanics may help us understand how this ancient rowing system has been preserved over evolutionary time. On the technological/engineering side, a more comprehensive description of ctene hydrodynamics will provide source material for new bioinspired sensors, devices, and vehicles (Asadnia et al., 2016; C. Liu, 2007; Sitti, 2018). Cilia arrays have been a major source of inspiration for microfluidic devices (Hanasoge et al., 2020; Sareh et al., 2013; Toonder & Onck, 2013); as we approach the intermediate Reynolds number regime, ctene-inspired devices may also provide promising new approaches for pumping or mixing fluid (Rockenbach et al., 2015; Rockenbach & Schnakenberg, 2017). In addition, the near-omnidirectional swimming capabilities of the ctenophore body plan show the potential of metachronal swimming as a source of design inspiration for robotic vehicles (particularly those that must navigate complex environments). However, our understanding of how such devices will interact with the surrounding fluid environment (intermediate Re) is neither systemic nor general, despite the importance of fluid dynamics in determining their performance.

1.2 Background and literature review

1.2.1 Metachronal coordination

In this section, we will explore key concepts and definitions in metachronal rowing by describing 1) a paddle as a single unit, 2) a row of multiple paddles, and 3) the metachronal coordination between them. To start, we define the appendage-based oscillatory Reynolds number as $Re_\omega \equiv 2\pi f l^2/\nu$, where f is the beat frequency in Hz, l is the paddle length, and ν is the kinematic viscosity of the surrounding fluid. Figure 1-2 shows three characteristic examples of metachronal paddles from a ctenophore, an Antarctic krill, and an American lobster, spanning three orders of magnitude of Re_ω. Noticeably, the paddle flexibility decreases as Re_ω increases: the ctene (Figure 1-2A) is a highly flexible cilia-based structure, while the pleopods (Figures 1-2B and C) resemble a two-link mechanism. Even between krill and lobster pleopods, we notice differences in rigidity: the distal part of the krill paddle is flexible, while the distal portion of the lobster is more rigid. Despite these structural differences, they all undergo similar rowing kinematics. Figure 1-2A shows the ctene tip trajectory, where dots represent equal time intervals. The top part of the trajectory, where the paddle is extended and moving quickly, is the power stroke, followed by the recovery stroke, where the paddle is bent and moving slowly. By inspecting the ctene trajectory, we can conclude that in addition to its geometry, we need at least four parameters to describe the oscillation kinematics: the beat frequency f, the stroke amplitude Φ, and a description of the time-varying tip speed and tip trajectory, which together quantify the spatiotemporal asymmetry of the beating cycle. In this work, we propose two quantifiable, nondimensional parameters to describe the temporal (Ta) and spatial asymmetry (Sa) ($e.g.$, the tip speed and trajectory shape; Ta and Sa are fully defined in section 2.1). These parameters also apply to other metachronal paddles, such as those shown in Figures 1-2B and C. The work presented in this document frequently refers to the spatiotemporal asymmetry parameters Sa and Ta, since they have proven to play crucial roles in thrust generation for the low to intermediate Reynolds number regime.

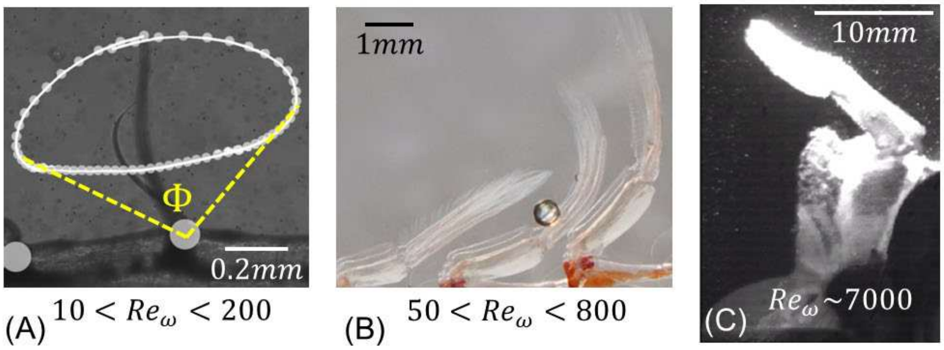

Figure **1-2.** Examples of metachronal paddles, showing how paddles shift from flexible to rigid/hinged structures as Re increases. (A) The ctenophore paddle (ctene) is a highly flexible cilia-based structure. White dots overlaid on the tip trajectory indicate equal time intervals, and the dotted yellow line indicates the stroke amplitude (Φ); reprinted from (Herrera-Amaya et al., 2021). (B) Antarctic krill paddle (pleopod), resembling a two-link mechanism where the proximal part is rigid and the distal part is flexible; reprinted with permission from (Santos et al., 2022). (C)

American lobster paddle (pleopod), similar in construction to the krill but with a more rigid distal part; reprinted with permission from (J. L. Lim & DeMont, 2009).

In metachronal rowing, the appendages are found in rows (or carpets, in the case of cilia; here, we consider only rows). Figure 1-3 shows a typical row. The row geometry is defined by the spacing ratio $s = l/\delta$, where δ is the distance between appendages and l is the paddle length. Because appendages are metachronally coordinated, each appendage completes a beat cycle (power-recovery stroke) at a fixed phase lag (P_L) from one another. For example, if the paddles in Figure 1-3 have a phase lag of 25%, this means that paddle 2 is 25% ahead in its beat cycle with respect to paddle 1, paddle 3 is 25% ahead of paddle 2, and so forth. From this coordination, a traveling "metachronal wave" whose wavelength λ is governed by P_L and s appears in the row. Figure 1-3 shows an example of antiplectic metachrony, in which the metachronal wave travels in the opposite direction of the power stroke. Antiplectic metachrony is the dominant coordination mode in swimming; other types of metachrony include symplectic, dexioplectic, and laeoplectic (Blake & Sleigh, 1974; Brennen & Winet, 1977).

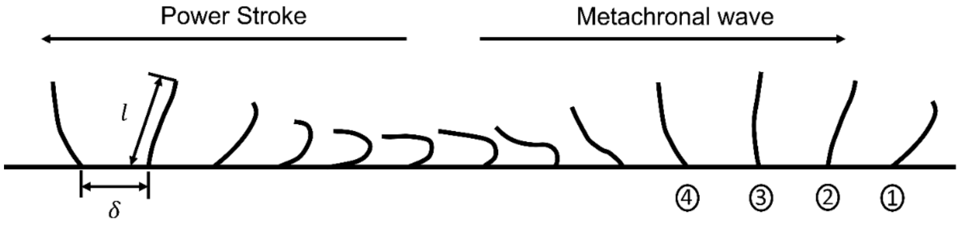

Figure **1-3.** Schematic of a row of metachronally coordinated paddles, in which paddles are separated by a distance δ and have length l.

In summary, we can describe metachronal rowing with the following parameters: beat frequency f, temporal asymmetry Ta, spatial asymmetry Sa, stroke amplitude Φ, spacing ratio s, and phase lag P_L (if the paddles are finite, we also consider their width w). Metachronal coordination has many desirable features, as previously discussed: it lifts the constraint that body speed cannot be higher than paddle speed (Murphy et al., 2011), and is more efficient than synchronous rowing (Elgeti & Gompper, 2013; Ford & Santhanakrishnan, 2020). Metachronal coordination also has an advantage in viscous-dominated, time-reversible flows. At $Re_\omega < 1$, flow is time-reversible and spatial asymmetry is necessary for a single oscillating appendage to produce net fluid displacement (Purcell, 1977). However, metachronal coordination can remove this constraint (Takagi, 2015)—if appendages beat with a nonzero phase-lag, spatially symmetric stroking can produce net flow even at low Re. Such performance has inspired recent research on the role of the phase-lag on the propulsive efficiency of metachronal swimming. Measurements from a krill-inspired robot place the optimal P_L between 16.7% and 25% (Ford et al., 2019), while a krill-inspired numerical model found it to be $20\% < P_L < 25\%$ (Granzier-Nakajima et al., 2020). Interestingly, this level of phase lag ($P_L = 25\%$) also yields the most robust coordination pattern that can be controlled by crustacean neural circuits (C. Zhang et al., 2014). Other studies have focused on the role of beat frequency and the spacing ratio (Barlow & Sleigh, 1993; Dauptain et al., 2008). However, the stroke spatiotemporal asymmetry has not been studied in the context of metachronal coordination. We seek to explore these parameters and their effects on swimming performance more fully.

At $Re_\omega < 1$, it is evident that a spatially asymmetric beat increases the net propulsion force (due to the higher drag imbalance between the power and recovery stroke). However, a fast power stroke and a slow recovery stroke (high Ta) would be energetically expensive without necessarily increasing the net fluid displacement. At intermediate Re, the role of spatiotemporal asymmetry is still unclear. Recently, (Saffaraval & Goudarzi, 2021) experimentally explored the roles of spatial and temporal asymmetries in a single oscillating long plate at intermediate Re, finding that increasing temporal asymmetry increased pumping performance and the presence of spatial asymmetry increased the pumping efficiency. However, experimental constraints in this study did not allow for continuous variation of spatial asymmetry, nor varying levels of both asymmetries simultaneously. Our experiments on living ctenophores show decreased spatial asymmetry and increased temporal asymmetry as the Reynolds number rises (see section 2.1). Our results also show significantly different flows in ctene rows with varying levels of spatial asymmetry at approximately equivalent Re_{ω}, hinting the importance of ctene kinematics to change the flow directionality (further discussed in section 2.1).

1.2.2 Ctenophore morphology

This section describes the morphology and physiology of ctenophores to the extent that it is of significant importance for their swimming (including parts of the organism that we will use as markers for tracking in section 2.2). Ctenophores (comb jellies) are gelatinous marine zooplankton, with bodies mainly composed of water (97%) (Hernandez-Nicaise, 1991). Ctenophores swim using eight rows of paddles called ctenes, circumscribing a spheroidal body (Figure 1-4A). Each ctene comprises thousands of long cilia which move as a unit (Heimbichner Goebel et al., 2020) (Figure 1-4C). These cilia are structurally similar to those found at the micron scale (low Re), but are much longer at approximately 1 mm in length (Afzelius, 1961). Ctenophores are carnivorous, feeding on crustaceans, other comb jellies, eggs, and fish larvae. Figure 1-4 shows *Bolinopsis vitrea,* a lobate ctenophore, so-called for the two muscle structures surrounding the mouth (Figure 1-4B). As larvae, *B. vitrea* use long retractable tentacles (Figure 1-4B), covered with specialized sticky cells called colloblasts, to capture their prey. Tentacles are no longer used for feeding when mature, but the tentacular bulbs remain (Figure 1-4A). Because the tentacular bulbs are visually prominent, we will use those two points as reference markers for kinematic tracking. The apical organ (or statocyst) is at the aboral end of the animal, opposite to the mouth; it serves as a gravity sensor (Figure 1-4B). When swimming, ctenophores often assume vertical positions where the principal body (oral-aboral) axis is aligned with gravity. This organ is the primary sensory interface (Hernandez-Nicaise, 1991) that enables that alignment. Like the tentacular bulbs, its visual prominence allows us to use it as a kinematic tracking marker (see section 2.2).

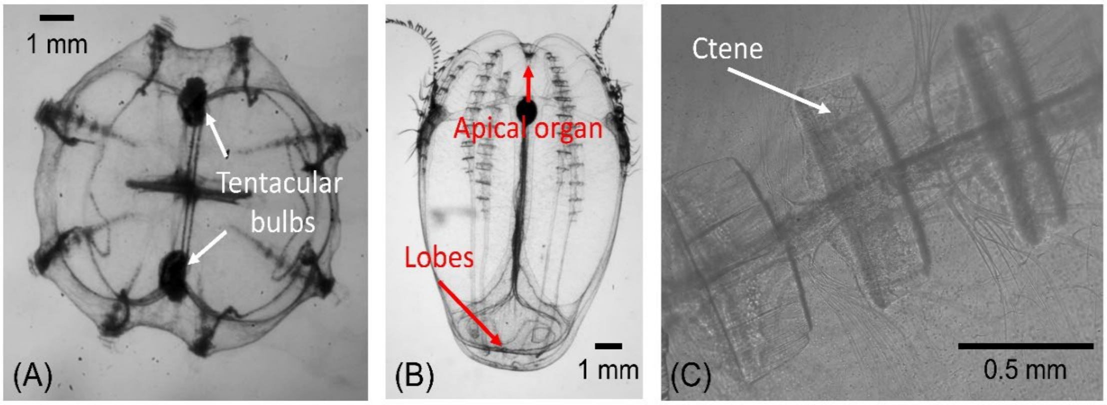

Figure **1-4.** A brief overview of relevant morphology of *Bolinopsis vitrea.* (A) top view showing the eight ctene rows and their radial symmetry, (B) lateral view of ctene rows circumscribing the body, and (C) close top view showing component cilia of each ctene. Reprinted with permission from (Herrera-Amaya et al., 2021).

1.3 Dissertation outline

This dissertation explores the following question: **how do ciliary kinematics scale from low to intermediate Reynolds numbers, and what are the implications for drag-based swimming in this regime?** We will combine animal experiments with physical and reduced-order analytical modeling to quantify the physics of ctene-generated flows across a range of Re. Studying ctenophore swimming is challenging due to the range of scales involved. Ctenophore appendages are one or two orders of magnitude smaller than their bodies (Figure 1-4); appendage-scale

Reynolds numbers are 10-200, and body-scale Reynolds numbers are 100-6000 (Matsumoto, 1991). Simultaneously measuring fluid velocity and swimming kinematics from the ctene scale to the body scale is a herculean task requiring high spatial and temporal resolution. We approach this difficulty by separating the problem into two behavioral experiments. We use high-speed 3D videography to analyze the maneuvering performance of freely swimming ctenophores, and Particle Shadow Velocimetry (PSV) to study ctene kinematics and flow production. We also measure variables involving the coordination of neighboring cilia (e.g., phase lag, spacing, and beat frequency). We use these experimental data to develop and verify a reduced-order analytical model, which serves as a numerical tool to explore the kinematic parameter space more fully than would be feasible with animal experiments alone. Finally, we create a dynamically scaled physical-robotic model of a single ctene, both as proof-of-concept for bioinspired design principles and as an additional tool to explore the parameter space of spatiotemporal asymmetry. We use the results of the animal experiments to verify both models' accuracy, and to inform the physical model's geometric and kinematic parameters. These two (non-behavioral) approaches will allow us to perform parametric studies of the effect of important variables across the range of Reynolds numbers observed in freely swimming ctenophores. This full sweep of the parameter space would be difficult to impossible to perform in natural systems, where variables of interest often cannot be controlled or prescribed.

This dissertation is organized as follows: Chapter 2 describes our experiments with living ctenophores. We first describe ctenophore swimming mechanics to help frame our research questions. We then present three-dimensional swimming data demonstrating ctenophores' excellent maneuverability and motivating our interest in their rowing mechanics. This is followed by a thorough description of the appendage kinematics and the observed changes of ctene/paddle kinematics as a function of Re, which is a core question of this work. Chapter 3 presents a reduced-order mathematical model, our first non-behavioral approach to elucidate the role of beat kinematics in a viscous-inertial fluid environment across the intermediate Re range. Such models help estimate the propulsion forces and provide a first-pass, high-level view of the role of the different parameters on animal swimming. However, this model does not solve the complete flow generated by the appendages, a crucial component in fully understanding the problem. Chapter 4 presents the rowing performance of bioinspired flexible and rigid robotic paddles, and explores the role of spatiotemporal asymmetries on thrust and lift production across the intermediate Reynolds number range. In this chapter, we also describe the adaptation of Particle Shadow Velocimetry (a flow quantification technique) to our experimental needs with live ctenophores (Chapter 2) as well as the dynamically scaled physical-robotic model. Chapter 5 summarizes our conclusions and proposes future avenues of exploration in bio-inspired aquatic locomotion. Finally, Appendix A contains specific details of the reduced-order model: appendage kinematics, geometrical derivations, and drag coefficient expressions, Appendix B contains a force sensitivity analysis for the experimental pressure calculations described in Chapter 4.

Chapter 2

Animal experiments

Two sampling sites and species were used for the experiments outlined in this chapter (summarized in Table 2-1). Both species are lobate ctenophores, with muscular extensions (lobes) on the body that project beyond the mouth (Figure 1-4B). This family of ctenophores uses lobes in conjunction with cilia to form a filter-feeding mechanism capable of outcompeting other species (Colin et al., 2010), enabling them to thrive across (and invade) many habitats (Kideys, 2002; Shiganova et al., 2001).

Bolinopsis vitrea were collected at Flatt's Inlet, Bermuda, in May 2018 and transported to the Bermuda Institute of Ocean Sciences (BIOS). Larger animals were maintained in a flow-through planktonkreisel tank with filtered seawater. At the same time, smaller specimens were kept in glass jars partially submerged in an open sea table with a continuous flow of filtered seawater. Animals were fed *ad libitum* on freshly hatched nauplii of *Artemia* sp. All experiments were conducted at ambient temperature (21-23°C) and completed within 12 hours of animal collection.

Bolinopsis infundibulum were sampled from existing cultures at the Monterey Bay Aquarium (MBA), Monterey, CA, in August 2019. Cultured animals were maintained in planktonkreisels with flow-through filtered seawater at 12-13°C and fed *Artemia* nauplii twice daily. Animals were removed from one kreisel, immediately used in experiments, and replaced in a second kreisel to avoid re-use.

Table **2-1**. Morphometric characteristics of observed animals (mean ± one standard deviation).

Data set	**Sample size***	**Body length (mm)**	**Ctene length (mm)**
BIOS	8	18.43±14.01	0.42±0.11
MBA	4	24.01±8.12	0.87±0.1

*Number of animals; for some analyses, multiple recordings per animal were used.

Section 2.1 has been published in *Integrative and Comparative Biology* (Herrera-Amaya et al., 2021), and section 2.2 is under review at the time of dissertation submission.

2.1 Propulsion mechanics: ctene row kinematics and flow production

This section focuses on the kinematics and fluid dynamics of the propulsion system employed by ctenophores. We use high-speed video and velocimetry to measure the kinematics and fluid dynamics of the beating ctene rows of two species of lobate ctenophores across a range of body sizes and Re. This work is the first to focus on spatiotemporal asymmetry in the beating of metachronal appendages, quantifying temporal asymmetry (Ta) as defined by (Gauger et al., 2009) and proposing a new non-dimensional parameter (Sa) to quantify spatial asymmetry. In this section, we use data collected from both BIOS and MBA (section 2.2 uses only the BIOS dataset, as the MBA dataset does not include 3D swimming trajectory data).

2.1.1 Imaging facilities

To obtain both flow velocities and ctene kinematics, we used a micro-scale Particle Shadow Velocimetry (μPSV) system following (Gemmell et al., 2014). μPSV is also called "brightfield Particle Image Velocimetry" (Khodaparast et al., 2013). Collimated white light illuminates the entire filming vessel and produces sharply-defined shadows of tracer particles and the target organism, which are then imaged via an extra-long working distance (ELWD) microscope objective (Figure 2-1). After inverting and preprocessing raw images, they can be input into standard PIV algorithms to produce two-dimensional velocity fields (L. P. Goss et al., 2007). The imaging volume is controlled by the optical depth of correlation (Koutsiaris, 2012), such that strongly out-of-focus tracers do not contribute to the calculated flow field. Using ELWD objectives permits the focal plane to be centered in the filming vessel, thus avoiding wall effects. A detailed description of the working principles of PSV can be found in section 4.2.

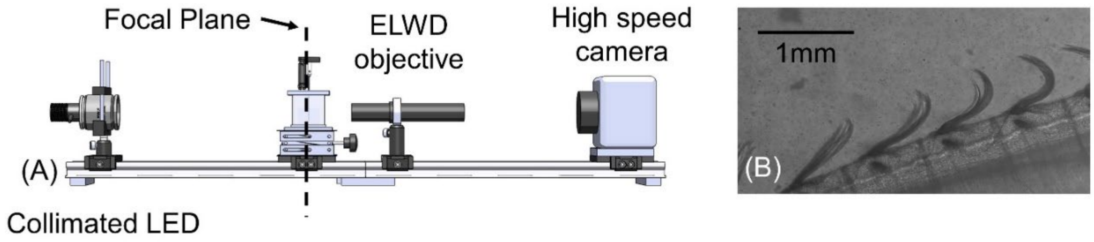

Figure **2-1.** (A) Schematic of experimental μPSV setup showing an in-line configuration of the camera, ELWD objective, filming vessel, and light source. (B) Example image collected via μPSV. Reprinted with permission from (Herrera-Amaya et al., 2021).

System components (MBA//BIOS) include a collimated white LED light source (Thorlabs, Newton, NJ, USA// Dolan-Jenner Industries, Lawrence, MA, USA), a transparent filming vessel, an ELWD objective (Achrovid, Centennial, CO, USA // Mitutoyo, Aurora, IL, USA), and a high-speed camera (Photron AX200, Photron USA Inc., San Diego, CA, USA // Phantom VEO 440, Vision Research Inc., Wayne, NJ, USA) (Figure 2-1A). In both experiments, images were collected at 1000 frames per second with an exposure time of 900 μs. To avoid adverse animal reactions to plastic or glass microbeads, the water was seeded with living phytoplankton, which served as approximately passive flow tracers since their swimming speed was much lower than the measured flow speeds (Gemmell et al., 2014). To accommodate differences in resolution between the two imaging systems, we used *Tetriselmis chuii* (average diameter of 10-12 μm) for the MBA dataset and *Nannochloropsis oculata* (2-3 μm) for the BIOS dataset. Tracer shadows were recorded in digital images with particle image diameters of 2-3 pixels, as appropriate for particle velocimetry (Raffel et al., 2018). We note that the brightfield imaging system used for the BIOS dataset is also described in (Karakas et al., 2020), and that those data are contemporary with the results presented here.

2.1.2 Velocimetry and kinematic analysis

We recorded image sequences when animals rested against the bottom of the filming vessel (zero forward swimming velocity). In some cases, we constrained animals using transparent acrylic plates. In all cases, the focal plane remained far from solid surfaces to avoid wall effects. We pursued kinematics analysis only if the ctenes were normal to the focal plane, and velocimetry analysis only if the plane of focus was roughly bisecting the ctene row. These restrictions yielded 12 image sequences for kinematics analysis and two for velocimetry analysis. The Depth of Correlation (DoC), or thickness of the useful measurement volume, is typically around 10 µm for µPSV, using magnifications of 10x – 40x (Gemmell et al., 2014). Our system required a 5x magnification to visualize several ctenes simultaneously (with a field of view of approximately 4 x 2.5 mm), leading to a DoC of ~ 130 µm (Koutsiaris, 2012). Standard PIV image prefilters retain significant noise from out-of-focus tracers at this magnification. We therefore developed a custom prefiltering algorithm that finds each focused particle and generates a new inverted image containing only the focused particles (section 4.2.1). The image preprocessing algorithm is described in detail in section 4.2. In these processed images, the average seeding density through the focal plane is $1.3x10^{-3}$ particles per pixel. We performed vector computation (two-pass iteration with subwindows of 128x128 px and 64x64 px, with 50% overlap) using the MATLAB-based tool PIVLab (Thielicke & Stamhuis, 2014). All image preprocessing and vector field postprocessing was conducted with MATLAB (Mathworks Inc., Natick, MA, USA).

Kinematic analysis was based on two-dimensional tracking data performed *via* the MATLAB-based tool DLTdv8 (Hedrick, 2008), including deep learning features. We tracked the base and tip of all fully visible ctenes for each image sequence. Figure 2-2 shows examples of two tracked ctene rows from two different animals. From the measured tip trajectory, we calculated the spatial asymmetry (degree of difference in flow-normal area between the power and recovery stroke) and temporal asymmetry (difference in duration of the power and recovery stroke). These parameters are defined in the next section.

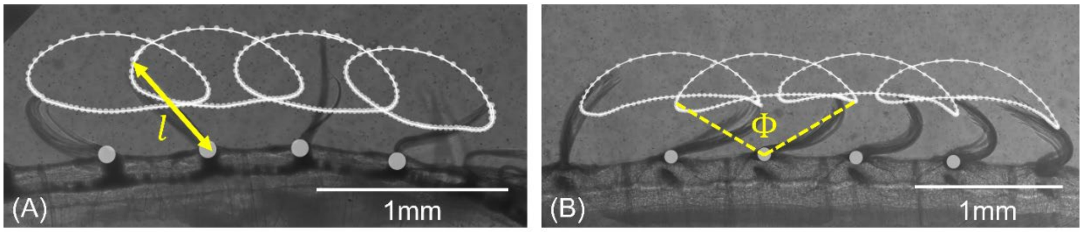

Figure **2-2.** Snapshots showing the tracked ctene base (circle) and ctene tip trajectories (solid white line). White dots overlaid on the tip trajectory indicate equal time intervals (Δt =0.001 s), showing the difference in tip speed between the power and recovery strokes. Ctene length (l) and stroke amplitude (Φ) are also marked. (A) shows an animal with $L_B = 11.56$ mm and $l = 0.62 \pm 0.02$ mm, with high spatial asymmetry; (B) shows an animal with $L_B = 40$ mm and $l = 0.76 \pm 0.01$ mm, with lower spatial asymmetry. Reprinted with permission from (Herrera-Amaya et al., 2021).

2.1.3 Morphological and metachronal parameters

As discussed in section 1.2.1, we describe the motion of a ctene row using seven parameters: three morphometric variables and five kinematic/coordination variables. Morphometric parameters include the ctene length (l), defined as the longest measured distance between the ctene base and tip during a beat cycle (Figure 2-2A), the ctene width (w), and the distance between appendages (δ). Coordination parameters include beat frequency (f), phase lag (P_L), stroke amplitude (Φ), and temporal asymmetry (Ta). Phase lag is the percentage of the cycle time that a ctene's beat cycle leads a neighboring ctene. Stroke amplitude (Φ) is the angle swept out by the ctene tip over one power stroke (Figure 2-2B). Temporal asymmetry (also known as the kinematic asymmetry parameter (Gauger et al., 2009)) is defined as:

$$Ta = \frac{t_r - t_p}{t_r + t_p} \qquad (1)$$

where t_r is the recovery stroke duration and t_p the power stroke duration. This parameter is zero for a time-symmetric beat cycle and one for an infinitely fast power stroke (Figure 2-3B).

To quantify the level of spatial asymmetry in each beat cycle for each ctene, we define a new parameter:

$$Sa = \frac{A_e}{A_o} \qquad (2)$$

where A_e is the area enclosed by the tip trajectory and A_o is the largest possible area of an ellipse inscribed within the reachable space of the ctene (that is, a half-circle with radius l), as shown in Figure 2-3A. Because of the ctene's flexibility, this ellipse represents a rough estimate of the theoretical maximum of the area that its tip could trace out. The ratio $Sa = A_e/A_o$ would therefore tend to one for highly asymmetric beat cycles, and zero for a rigid ctene moving symmetrically.

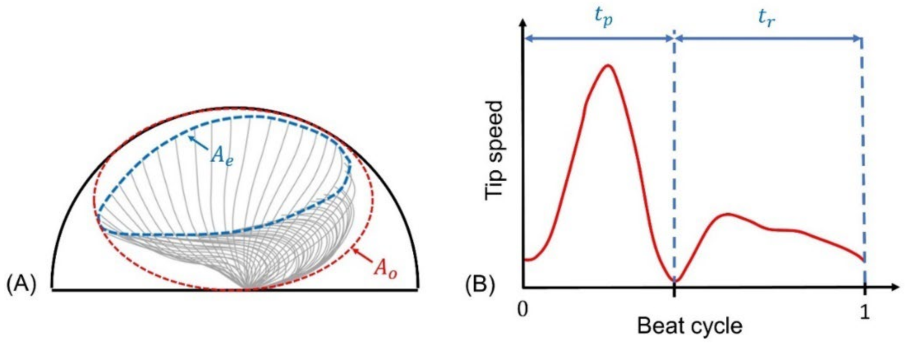

Figure **2-3.** (A) Graphical definition of spatial asymmetry parameter Sa overlaid on a time-series of ctene kinematics (gray lines). The black half-circle is the reachable space of a ctene with length l; the larger ellipse A_o (red dotted line) estimates the maximum area that could be enclosed by ctene tip over a complete cycle; inner shape A_e (blue dotted line) is the actual ctene tip trajectory. (B) Schematic of ctene tip speed over one beat cycle. The temporal asymmetry parameter Ta is a function of t_p (time between the first two minima of the tip speed curve) and t_r (remaining cycle time). Reprinted with permission from (Herrera-Amaya et al., 2021).

2.1.4 Results

To examine the flows generated by ctene rows beating across a range of body sizes, Reynolds numbers, and spatiotemporal asymmetries, we used μPSV as described in the previous section. Figures 2-4A and D show sample velocity fields from two specimens of *B. vitrea*. Flow shown in Figure 2-4A is similar to previous observations of ctenophores (Barlow et al., 1993), with no apparent vortices—the peak flow speed is co-located with the ctene tip as it reaches its maximum speed. Flow reversal is only present in the sub-ctene layer; the outer flow is primarily unidirectional and relatively steady. The animal shown in Figure 2-4D is larger in both body size and ctene length and generates a slightly more complex flow. The maximum flow speed is no longer attached to the ctene tip. A clear tip vortex is present, indicating the growing importance of fluid inertia. A tip vortex such as that seen in Figure 2-4D has not been previously seen in ctenophores, but is consistent with observations of metachronal swimmers operating at slightly larger Re (250-1000) (Colin et al., 2020; Ford et al., 2019; Murphy et al., 2013). Figures 2-4B and E show the radial velocity magnitude, averaged over seven beat cycles, while Figures 2-4C and F show the time-averaged tangential velocity magnitude, with the angular decomposition based on the center of a circular arc fitted to the body wall. The flow is tangentially dominated; however, the average radial velocity component close to the ctenes is noticeably higher for the larger animal, indicating increased two-dimensionality of the flow.

The animal shown in Figure 2-4D has a slightly higher Re_ω (see Table 2-2) and shows a lower degree of spatial asymmetry ($Sa = 0.29$) relative to the animal shown in Figure 2-4A ($Sa = 0.53$), which has a slightly lower Re_ω (see Table 2-2). It is likely that both the increased Re_ω and the lower degree of spatial asymmetry in the stroke contributes to the presence of vortices in Figure 2-4D. Though the Reynolds number is lower and the appendage is more deformable, the measured flows are similar to the well-characterized vortex-shedding behavior observed in flexible flapping foils (Dewey et al., 2013; Marais et al., 2012; Quinn et al., 2014).

Table **2-2**. Flow parameters for Figure 2-4 (mean $\pm$ one standard deviation of 30 (small animal) and 7 (large animal) cycles).

$\boldsymbol{L_b}$(mm)	$\boldsymbol{Re_\omega}$	$\boldsymbol{l}$(mm)	$\boldsymbol{f}$(Hz)	$\boldsymbol{Sa}$	$\boldsymbol{Ta}$	$\boldsymbol{P_L}$(%)	$\boldsymbol{\Phi}$(°)
11.56	23.93± 0.5	0.62± 0.02	16.74 ± 0.98	0.53 ± 0.01	0.04 ± 0.07	13.11 ± 1.22	101.76 ± 4.83
38.99	68.27± 3.39	0.93± 0.03	11.23 ± 0.23	0.29 ± 0.03	0.15 ± 0.04	13.04 ± 1.24	104.15 ± 2.49

We note that obtaining high-quality flowfields is technically challenging, as it requires delicate alignment between the ctene row and the focal plane of the imaging system. Furthermore, the ctene row must remain aligned for a nontrivial period of time to draw conclusions about the beat cycle. These quality standards resulted in only two video sequences suitable for µPSV analysis (out of 12 video sequences processed for ctene kinematics). While these sequences do show animals of different sizes and ctenes beating at slightly different Re_ω, the sample size is not large enough to draw definitive conclusions about the role of spatiotemporal asymmetry in flow generation across scales. We also note that these animals are somewhat constrained and measured with zero swimming speed, as discussed in the previous section. The velocity fields, particularly in the far field, will likely differ for a freely swimming animal. The ctene kinematics, particularly those driven by passive fluid-structure interactions, may also be different for this case. However, our qualitative observations of the general character of the velocity fields – a more two-dimensional flowfield for larger animals with higher beat frequencies – are likely to hold for the free-swimming case as well.

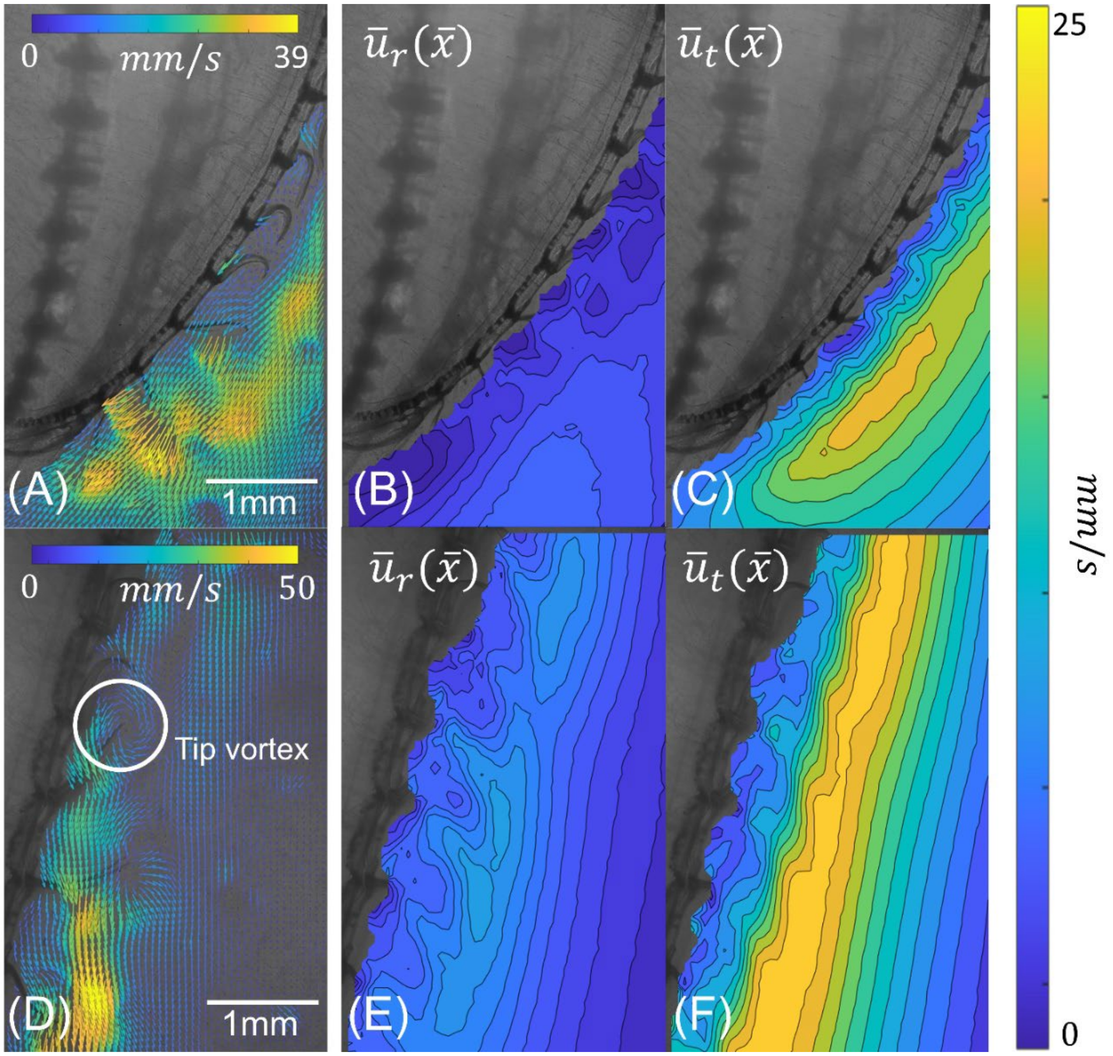

Figure **2-4.** (A) Instantaneous velocity field for a ctenophore with a body length $L_B = 11.56$ mm and average ctene length $l = 0.62 \pm 0.02$ mm. (B) Time-averaged radial velocity magnitude. (C) Time-averaged tangential velocity magnitude. (D) Instantaneous velocity field for a ctenophore with a body length $L_B = 38.99$ mm and average ctene length $l = 0.93 \pm 0.03$ mm. (E) Time-averaged radial velocity magnitude. (F) Time-averaged tangential velocity magnitude. Panels B, C, E, and F are averaged over seven beat cycles and share the color scale displayed on the right. Reprinted with permission from (Herrera-Amaya et al., 2021).

Of the previously defined kinematic/coordination parameters, several are commonly reported in published studies (stroke amplitude Φ, phase lag P_L, and beat frequency f). Table 2-3 shows these parameters for several ctenophore species; our results are consistent with previous observations. However, the degree of spatiotemporal asymmetry is not typically reported. In the current study, we measure spatial asymmetry Sa and temporal asymmetry Ta for ctenes engaged in idle, steady beating as previously defined (Figure 2-3).

Table **2-3.** Measured values for stroke amplitude, (Φ), phase-lag (P_L), and beat frequency (f) of ctene rows. Where margins are indicated, they are the mean plus or minus one standard deviation.

Species	$\boldsymbol{\Phi}$ (°)	$\boldsymbol{P_L}$ (%)	$\boldsymbol{f}$**(Hz)**	**Beating mode**	**Source**
B. vitrea	112.1 ± 8.9	13.2 ± 1.7	15.1 ± 2.2	Idle/Tethered	Current study
B. infundibulum	102.1 ± 5.2	13.9 ± 4.9	27.7 ± 1.9	Idle/Tethered	Current study
Mertensia ovum*	−	−	7	Active swimming	(Matsumoto, 1991)
Beroe artic*	−	−	15	Active swimming	(Matsumoto, 1991)
L. pulchra*	−	−	13	Active swimming	(Matsumoto, 1991)
P. pileus^{+}	135 ± 15.5	−	10, 27	Tethered	(Barlow & Sleigh, 1993)
P. pileus^{+}	−	7.07 ± 3.5	5 to 25	Tethered	(Barlow et al., 1993)
P. bachei	−	−	10.1 ± 5.1	Active swimming	(Heimbichner Goebel et al., 2020)

*Average of > 25 measurements (σ not reported), + Beat frequency controlled by a mechanical actuator.

Our results show that for *B. vitrea*, as Re_ω increases, Sa declines and Ta is nearly constant; for *B. infundibulum*, Sa is nearly constant, and Ta increases (Figure 2-5). All specimens of *B.*

infundibulum were observed to have higher Re_ω than that of *B. vitrea.* While these data are somewhat sparse, they indicate that the roles of spatial and temporal asymmetry may interact with one another. This interaction may change depending on the relative importance of viscosity and inertia. The drop in Sa is non-intuitive: since higher spatial asymmetry should correspond to greater force production, it is unclear why it would decrease with increasing Re_ω. To further investigate the relationship between Sa and Ta, we turn to a simple reduced-order analytical model (described in section 3.1). Using this simple model, we can qualitatively investigate how increasing or decreasing spatiotemporal asymmetry can affect swimming efficiency. The model is simple by design, meant to predict trends in force and power generation (and how they vary with spatiotemporal asymmetry) rather than the true values of these quantities. Due to its necessary simplifying assumptions, this model will not capture the full complexity of an actual ctene row; however, it serves as a useful tool for investigating the role of spatiotemporal asymmetry across a large parameter space, which would be computationally prohibitive for a higher-fidelity model.

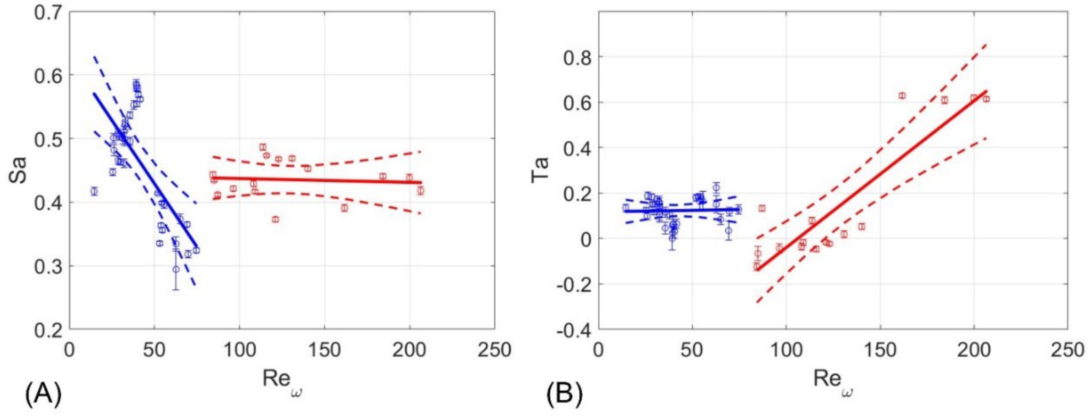

Figure **2-5.** (A) Spatial asymmetry Sa *vs*. oscillatory Reynolds number Re_ω. Lower Re_ω data (shown in blue) indicates *B. vitrea* (BIOS); higher Re_ω data (shown in red) indicates *B. infundibulum* (MBA). Linear regressions for each dataset (solid lines) have regression coefficients $R_{BIOS} = 0.4\ and\ R_{MBA} = 0.01$. (B) Temporal asymmetry Ta vs oscillatory Reynolds number

Re_ω. Linear regressions for each dataset (solid lines) have regression coefficients $R_{BIOS} = 0.01\ and\ R_{MBA} = 0.79$. Open circles represent the mean value for a single ctene; errorbars show 95% confidence interval based on measured cycles (>20). The dotted lines represent 95% confidence bands on the linear regressions. Reprinted with permission from (Herrera-Amaya et al., 2021).

2.1.5 Summary

Velocimetry and paddle kinematics of live animals show that a rowing appendage's spatial and temporal asymmetry levels play an important role at intermediate Reynolds numbers. Laboratory experiments on lobate ctenophores showed both qualitative and quantitative differences between the flows generated by two animals whose ctenes beat at different Reynolds numbers and different spatiotemporal asymmetries, including the presence of tip vortices and increased two-dimensionality for the higher Re_ω / lower Sa case. The higher Re_ω / lower Sa case also showed increased radial momentum production, which may also impact turning. However, the flowfields shown in Figure 2-4 are not enough to draw predictive conclusions. While the velocimetry analysis is limited, our observation of ctene kinematics in living animals revealed that as Re_ω increases, spatial asymmetry decreases and temporal asymmetry increases. We will employ the reduced-order model of section 3.1 to explore the consequences of this trend for force production and swimming performance.

2.2 Metachronal maneuverability

Metachronal coordination of appendages is seen in many aquatic organisms spanning a wide range of sizes and body plans, including shrimp, krill, polychaetes, and even aquatic insects

(Alben et al., 2010; Byron et al., 2021). The generated flow can be used for swimming or pumping to aid in feeding, clearance of wastes, and other functions (Garayev & Murphy, 2021; Larson et al., 2014). This technique is highly scalable, with metachronal coordinated appendages ranging from microns to centimeters in length. Studies of metachronal locomotion have thus focused primarily on unidirectional swimming ability (Daniels et al., 2021; Garayev & Murphy, 2021; Hayashi & Takagi, 2020; Matsumoto, 1991), but some metachronal swimmers are also capable of surprising agility. Though ctenophores are primarily planktonic, they also swim actively. Their natural environment has led them to become highly skilled intermediate Reynolds number swimmers, with a propulsion system that can maneuver against a range of background flow scales (Sutherland et al., 2014). However, their turning behavior has only been described qualitatively (Tamm, 2014). Existing quantitative information on ctenophore swimming trajectories comes from single-camera (2D) experiments focused on straight swimming (Gemmell et al., 2019; Heimbichner Goebel et al., 2020; Kreps et al., 1997; Matsumoto, 1991). There is no explicit quantitative data on ctenophores' turning, nor any direct measurements of ctene beating frequencies in the context of turning.

Therefore, we know little of the turning control strategies used by ctenophores (or other metachronal swimmers). We use multicamera high-speed videography and three-dimensional kinematic tracking to correlate overall trajectories with the beating frequencies of the ctene rows and identify three distinct turning modes. In this section, we introduce the Maneuverability-Agility Plot (MAP) to explore the observed turning performance of ctenophores, showing how they can sharply turn at high speeds relative to their top speed. In addition, by reconstructing *B. vitrea's* “reachable space,” also known as the Motor Volume (MV) (Snyder et al., 2007), we show that ctenophores have the potential to reorient around many directions within a small space over a short timeframe (omnidirectionality). Results from this section are drawn from 27 different recordings from eight ctenophores from the BIOS data set, with an average body length of $7.93 \pm 1.97mm$ (mean ± standard deviation).

2.2.1 Imaging facilities

For the BIOS dataset, freely swimming animals were simultaneously filmed from multiple angles at high speeds in order to provide three-dimensional swimming trajectories. The recording setup consists of three synchronized high-speed cameras (Edgertronic, Sanstreak Corp., San Jose, CA, USA), observing an experimental volume ($30 \times 30 \times 30mm^3$) from three orthogonal perspectives (Figure 2-6A). Cameras filmed at 600 Hz at a resolution of 1024x912 pixels and were equipped with $200mm$ Nikon macro lenses with apertures set to f/32 (depth of field $\sim 12mm$). Collimated LED light sources were used to backlight each camera (Dolan-Jenner Industries, Lawrence, MA, USA). Calibration was performed by translating a calibration wand with a micromanipulator through 27 pre-mapped points, creating a virtual 3x3x3 cube. Calibration coefficients were calculated by mapping the 2D camera coordinates into 3D space using the direct linear transform algorithms embedded in the software DLTdv8 (Hedrick, 2008). After calibration, we tracked three points (the apical organ and the two tentacular bulbs) on each ctenophore (Figure 2-6B) using the deep-learning features of DLTdv8. Figure 2-6C shows an example maneuver reconstructed from the described experimental setup. We note that the camera system is also described in (Karakas et al., 2020), which contains contemporary data with the results presented here.

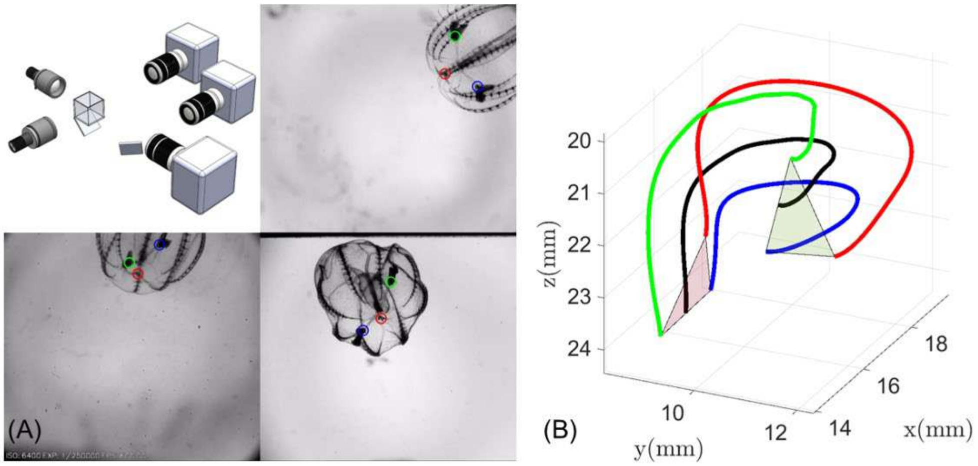

Figure **2-6.** (A) Schematic of the 3D recording system showing the three orthogonal camera views. (B) Tracked points: apical organ (red) and tentacular bulbs (blue and green). (C) Example of a reconstructed trajectory; black line is the midpoint of the line segment joining the two tentacular bulbs.

2.2.2 Ctenophore morphometric and kinematic parameters

We need nine morphometric and five kinematic parameters to describe the overall ctenophore propulsion system. These are listed in Table 2-4, along with a brief description, while Figure 2-7 shows a graphical description of some parameters. Lastly, Table 2-5 shows the average of the morphometric parameters as measured from eight individuals.

Table **2-4.** Ctenophore morphometric and kinematic parameters.

Variable	**Description**
$\boldsymbol{L_B}$	Body length
$\boldsymbol{d_B}$	Body diameter (measured in tentacular plane)
$\boldsymbol{l}$	Ctene length
$\boldsymbol{\delta}$	Average distance between ctenes
$\boldsymbol{n_S}$	Number of ctenes on each sagittal row
$\boldsymbol{n_T}$	Number of ctenes on each tentacular row
$\boldsymbol{\varepsilon_S}$	Sagittal ctene row position angles (measured from tentacular plane)
$\boldsymbol{\varepsilon_T}$	Tentacular ctene row position angles (measured from tentacular plane)
$\boldsymbol{\kappa}$	Position angle of the first ctene on the row (measured from centroid)

$\boldsymbol{f}$	Beat frequency
$\boldsymbol{\Phi}$	Stroke amplitude
$\boldsymbol{P_L}$	Phase lag between adjacent ctenes, expressed as a percentage of the cycle period
$\boldsymbol{Ta = \frac{t_r - t_p}{t_r + t_p}}$	Temporal asymmetry, quantifying the time difference between the power (t_p) and recovery strokes (t_r); also known as the "kinematic parameter" (Gauger et al., 2009)
$\boldsymbol{Sa = \frac{A_e}{A_o}}$	Spatial asymmetry, quantifying the degree of difference in flow-normal area between the power and recovery stroke by comparing the area enclosed by the ctene tip trajectory A_e to its practical maximum A_o (Herrera-Amaya et al., 2021)

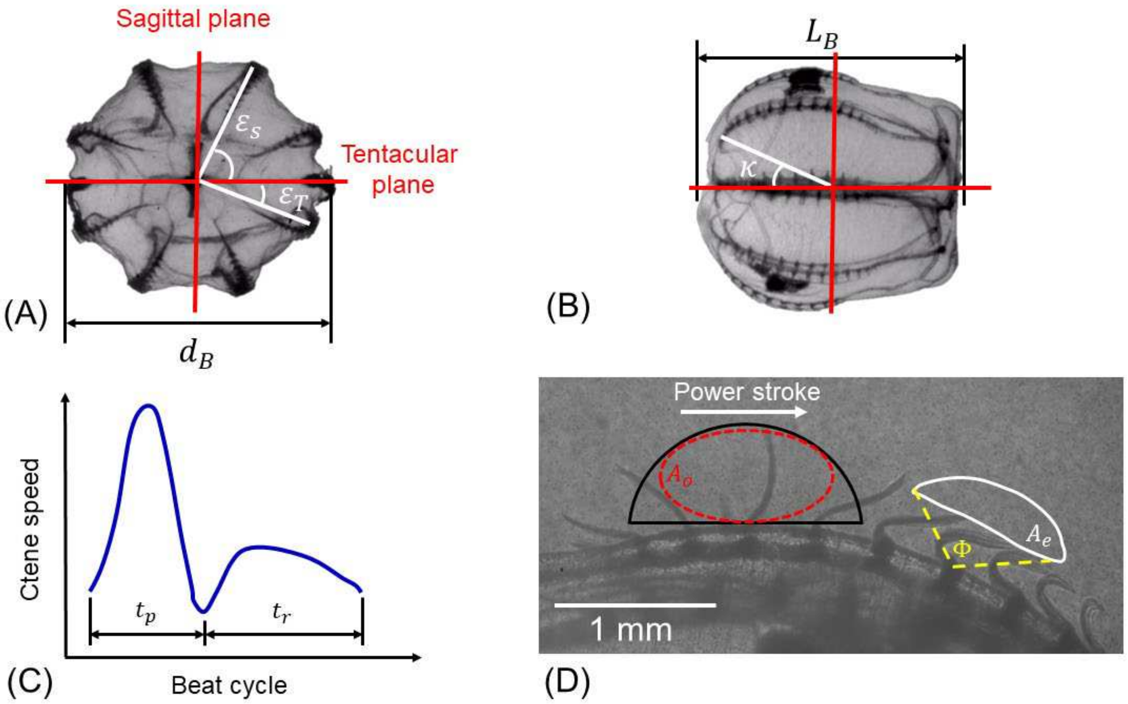

Figure **2-7.** Morphology and ctene row kinematics of a typical *Bolinopsis vitrea*. (A) Top view showing the eight ctene rows, the ctene row position angle ε, and the sagittal and tentacular planes ($d_B = 7.6mm$). (B) Side view showing the ctene rows along the body ($L_B = 7.4mm$) and κ, the angle for the most aboral ctene. (C) Stylized example time-series of ctene tip speed for one ctene over one beat cycle, where t_p is the power stroke duration and t_r the recovery stroke duration. (D) Ctene row close side view, showing a tracked ctene tip trajectory (A_e, solid white line), and the estimated ctene reachable space (A_o, red dashed ellipsoid inscribed in a black half circle of radius

l; shown elsewhere on the ctene row for clarity). Stroke amplitude (Φ) and the direction of the power stroke are also marked.

Table **2-5.** Morphometric measurements of included *B. vitrea* (mean ± one standard deviation)

$\boldsymbol{L_B(mm)}$	$\boldsymbol{d_B(mm)}$	$\boldsymbol{l(mm)}$	$\boldsymbol{s}$	$\boldsymbol{n_S}$	$\boldsymbol{n_T}$	$\boldsymbol{\varepsilon_S(^\circ)}$	$\boldsymbol{\varepsilon_T(^\circ)}$	$\boldsymbol{\kappa(^\circ)}$
7.8 ± 1.6	6.1 ± 1.7	0.5 ± 0.06	0.8 ± 0.2	10 ± 1.7	7.1 ± 1.2	63.9 ± 2.1	23 ± 2.4	27 ± 5.1

2.2.3 Results

From 27 recorded sequences of eight individuals, we observed four different appendage control strategies. These strategies differ categorically in the total number and the geometrical arrangement of the rows actively beating. The first three strategies are used to turn, with rows on the outside of the turn beating at a higher frequency than the rows on the inside of the turn $(f_{out} > f_{in})$. In the first strategy (mode 1), two adjacent rows beat at some frequency f_{out} and the two opposite rows beat at a lower frequency f_{in} while the remaining four rows are inactive. In the second strategy (mode 2), the four outer rows beat at approximately the same frequency, which exceeds the frequency used by the four rows on the opposite side. For the third strategy (mode 3), six rows beat at a constant frequency f_{out} while only two rows beat at a lower frequency f_{in}. Lastly, in mode 4, all rows are beating at approximately the same frequency; thus, the animal swims roughly in a straight line. The observed control strategies agree with morphological studies of lobate ctenophores (Tamm, 2014): the apical organ has four compound balancer cilia, and each balancer controls the activation of one sagittal and one tentacular row. In other words, *B. vitrea* can independently control the ctenes in each body quadrant formed by the sagittal and tentacular planes (see Figure 2-7A). Both rows in each quadrant beat at approximately the same frequency. Table 2-6 summarizes the control strategies and the number of times each was observed. The recorded beat frequencies range from 0 to $34.5\ Hz$.

Table **2-6.** Appendage control strategies observed in freely swimming *B. vitrea*

Control strategy	**No. of rows beating at f_{out}**	**No. of rows beating at f_{in}**	**No. of observations (out of 27)**
Mode 1	2	2	2
Mode 2	4	4	8
Mode 3	6	2	9
Mode 4	8	0	8

Two important variables explore and quantify turning performance: maneuverability and agility. Maneuverability refers to the ability to turn sharply within a short distance. It is typically quantified by the swimming trajectory's radius of curvature (usually normalized by body length) (Norberg & Rayner, 1987). Agility, however, is not clearly or consistently defined in the animal locomotion literature. A widely used definition is the ability to rapidly reorient the body (Webb, 1994), quantified by the maximum observed angular velocity. However, the angular velocity on its own does not speak to whether the animal needs to stop or slow to perform a turn, which is another colloquial definition of agility. An animal's translational speed while performing a turn can give insight into its agility (Fish & Nicastro, 2003; Walker, 2000; Webb & Fairchild, 2001). Here, we will use the average speed during the turn $(\bar{V})$ as a measure of agility, and the average normalized radius of curvature $(\overline{R/L}$, where R is the radius of curvature and L is the body length) during the turn as a measure of maneuverability. We can examine a large number of discrete turns to build a Maneuverability-Agility Plot (MAP), plotting $\overline{R/L}$ *vs.* $\bar{V}$ for a given organism.

We used the observed 3D swimming trajectories of *B. vitrea* to build a MAP. In Figure 2-8, the x-axis shows the average animal speed during the recorded sequence $(\bar{V})$, measured in body lengths per second, which we treat as a measure of agility. The y-axis shows the average normalized radius of curvature $\left(\overline{R/L}\right)$, which we treat as a measure of maneuverability. Movements that are both highly maneuverable and highly agile are found in the lower-right corner of the MAP, while highly maneuverable but less agile (slow) movements are found in the lower-left corner. From the experimental observations, we observe an increase in $\overline{R/L}$ as $\bar{V}$ increases, an expected tradeoff between maneuverability and agility (Fish & Nicastro, 2003). The most maneuverable observed turn has $\overline{R/L} = 0.08$ at a speed of $\bar{V} = 0.22\ BL/s$ (lower-left corner). In the lower-right corner, we have a turn with a measured speed of $\bar{V} = 1.89\ BL/s$ for $\overline{R/L} = 1.3$—still a comparatively sharp turn, carried out at 71% of the maximum recorded straight-line swimming speed of $\bar{V} = 2.65\ BL/s$ (rightmost point, Figure 2-8). Simply put, ctenophores are capable of sharp turning while maintaining considerable speeds—that is, they have both high maneuverability and high agility.

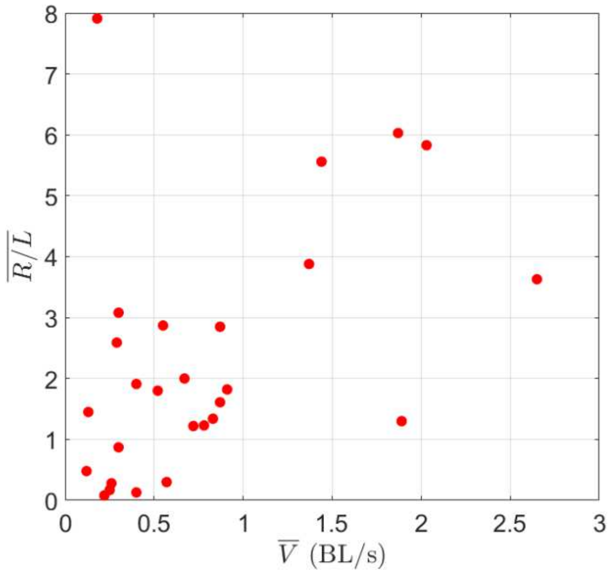

Figure **2-8**. Maneuverability-Agility Plot (MAP). Experimental measurements of freely swimming *B. vitrea*. Lower values of $\overline{R/L}$ indicate sharp turns (more maneuverable); higher values of $\bar{V}$ indicate faster swimming (more agile). Values in the upper left (low $\bar{V}$, high $\overline{R/L}$) are straightforwardly achievable with straight swimming (mode 4).

Due to their high number of appendages, the distribution of appendages along the body, and the independent frequency control between paired rows, ctenophores are capable of achieving the performance displayed in Figure 2-8 over numerous planes of motion. Using the observed 3D swimming trajectories, we estimate *B. vitrea*'s motor volume (MV) (Snyder et al., 2007), which illustrates the maneuvering capabilities of the ctenophore locomotor system (Figure 2-9). Conceptually, the MV represents the reachable space of a swimming ctenophore over a given time horizon. To build the MV, we translated and rotated the observed swimming trajectories so that at the start of the trajectory, the tentacular plane is on the x-y plane, with the midpoint between the tentacular bulbs on the origin, the aboral-oral axis of symmetry is aligned with the x-axis, and the tentacular bulbs facing the positive x-direction. From this starting position, the positive x-direction is forward swimming (lobes in front) and the negative x-direction is backward swimming (apical organ in front). Figure 2-9 shows the rearranged swimming trajectories (black lines) and the volume swept by the animals' bodies (gray cloud). Each animal body was estimated as a prolate spheroid based on its unique body length and diameter (L_B, d_B). In our observations, animals swam freely (without external stimuli), and the trajectories were recorded through the time period that the animal was in the field of view. Each observation has a different initial speed and total swimming time (see Table 2-7); thus, this MV does not directly compare different appendage control strategies, since observed maneuvers have different initial speeds and durations. We also note that because we only observed animals who freely swam through the field of view, the experimental dataset is biased towards animals who had a nontrivial initial swimming speed, leading to a stretching of the MV along the x-axis. Nonetheless, the observed MV shown in Figure 2-9 provides some visualization of the 3D maneuvering capabilities of *B. vitrea*'s locomotor system. In section 3.2.3, we use reduced-order analytical modeling to further explore the potential motor volume across a wider range of behaviors than those observed in these experiments.

Table **2-7.** Experimental recordings (mean ± one standard deviation)

Swimming direction	**No. Recordings**	**Initial speed (BL/s)**	**Recording duration (s)**
Forward (+x)	19	0.61 ± 0.75	2.25 ± 1.34
Backward (-x)	8	0.85 ± 0.55	1.82 ± 1.11

Figure 2-9 shows the potential of the ctenophore locomotor system for omnidirectional swimming, which we define as the ability to move in any direction from a given initial position within a relatively small space and a short time. Figure 2-9A shows nearly equal capacity between backward and forward swimming—an ability few swimmers share, and which typically requires major adjustments to control strategy (Sutherland et al., 2019). Ctenophores, by contrast, achieve agile backward swimming simply by reversing the direction of the ctene power stroke. The trajectories in Figure 2-9 are achieved via the activation of different ctene rows, which (when coupled with the ability to swim both forward and backward) allow ctenophores to quickly access many different swimming directions from the same initial position.

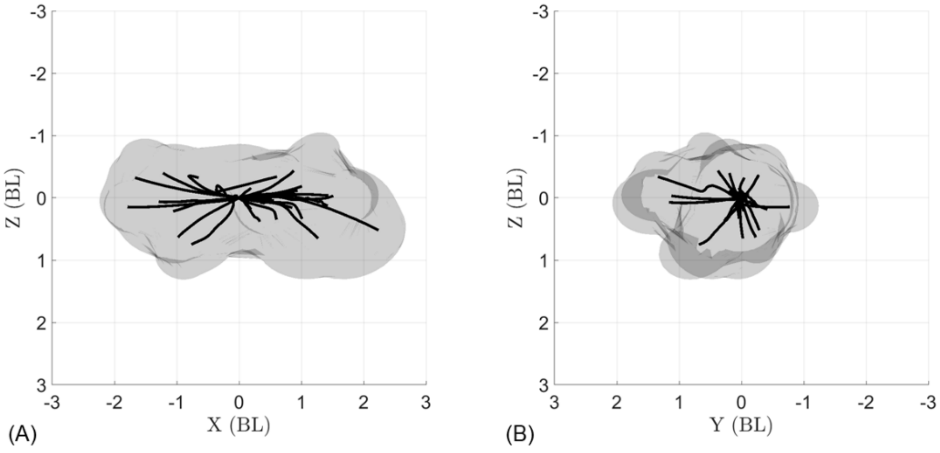

Figure **2-9**. Motor volume (MV) constructed from the 27 tracked swimming trajectories of *B. vitrea*. Black lines show swimming trajectories (midpoint between tentacular bulbs) and volume swept by animals' bodies (gray cloud) during each maneuver. Based on morphological measurements, animal volume is estimated as a prolate spheroid (Table 2-5). (A) Side view and (B) front view of the tracked swimming trajectories and motor volume show that *B. vitrea* can turn over a large range of angles.

2.2.4 Summary

Ctenophores' higher number of propulsive rows differentiates them from other metachronal swimmers, which typically have only one or two rows of propulsors (Garayev & Murphy, 2021; J. L. Lim & DeMont, 2009; Murphy et al., 2013; Ruszczyk et al., 2022; Sutherland et al., 2019). Flexibility in controlling a higher number of appendages, combined with the ability to swim backward and forward, allows for nearly omnidirectional swimming. Our results illustrate that the ctenophore body plan is highly agile and maneuverable. Ctenophores can turn sharply without slowing down, reverse directions easily, and turn about many planes, enabling them to access a nearly-unconstrained region of space from a given initial position over relatively short time horizons. To explore both the turning performance and the omnidirectional capabilities of *B. vitrea* more systematically, we will employ the reduced-order model of section 3.2. Using this mathematical model, we can investigate ctenophore turning across a range of beat frequencies and appendage control strategies, revealing the potential of the ctenophore body plan for bio-inspired design.

Chapter 3

Reduced-order analytical modeling

A limitation of behavioral experiments with living animals is that parameters cannot be varied independently; without a prohibitively large dataset, it is difficult to explore the parameter space and identify key functional dependencies fully. Numerical methods (e.g., computational fluid dynamics) are more controllable (Granzier-Nakajima et al., 2020; Y. Liu et al., 2021; Semati et al., 2020a), but computationally costs can be prohibitive for a parameter sweep of a highly multivariate problem. In addition, to fully simulate ctenophore swimming would require a large domain to capture an entire maneuver (on the scale of centimeters) while resolving flow around the ctene rows (sub-millimeter scale). The ctenes are at least twenty times smaller than the body, so computational resources needed for a fully-coupled model of even a few ctenes in a row are already a limiting factor (Dauptain et al., 2008; D. Lim et al., 2019a; Semati et al., 2020a). However, a simplified modeling approach is still attractive due to the large and multivariate parameter space we seek to explore.

Section 3.1 has been published in (Herrera-Amaya et al., 2021), and section 3.2 is under review at the time of dissertation submission.

3.1 Rowing spatiotemporal asymmetry: One-dimensional swimming equation

Here we develop a reduced-order analytical model based on known empirical expressions for fluid drag— an approach previously used to study metachronal rowing in 1D for low to intermediate Reynolds numbers (Alben et al., 2010; Du Clos et al., 2022; Takagi, 2015). This class of analytical model is limited because it does not consider hydrodynamic interactions between the propulsors. Therefore, it cannot fully reproduce key features (such as enhanced swimming efficiency) of metachronal swimming. However, it can still reasonably predict swimming kinematics, and (most importantly) it provides a useful tool for comparing the relative effects of the many morphometric and kinematic parameters involved in metachronal swimming without prohibitive computational costs.

Our model has three notable features, which distinguish it from previous (analytical or robotic) modeling attempts: (i) we directly prescribe the level of spatiotemporal asymmetry (Sa and Ta); (ii) we model the phase lag between appendages as a continuous (rather than discrete) variable, in contrast to (Alben et al., 2010), and (iii) we explicitly include both viscous and inertial effects by using an intermediate-Re drag coefficient formulation (Shih & Buchanan, 1971).

Each ctene is treated as an oscillating flat rigid plate, whose distal end traces an ellipse (Figure 3-1). The ellipse's major axis is set by the prescribed stroke amplitude (Φ), and its minor axis is set by the prescribed spatial asymmetry Sa (see Appendix A1). The plate reciprocates horizontally over a total cycle period T equal to the inverse of the prescribed frequency f. Time spent in the power ($0 \leq \theta \leq \pi$, where θ is the angle swept out by the tip as it moves around the ellipse) and recovery ($\pi < \theta < 2\pi$) strokes is set by the prescribed temporal asymmetry Ta. This yields the parametric tip position ($x_A(t), y_A(t)$) as a function of the prescribed variables (for further details of the modeled kinematics, see Appendix A1).

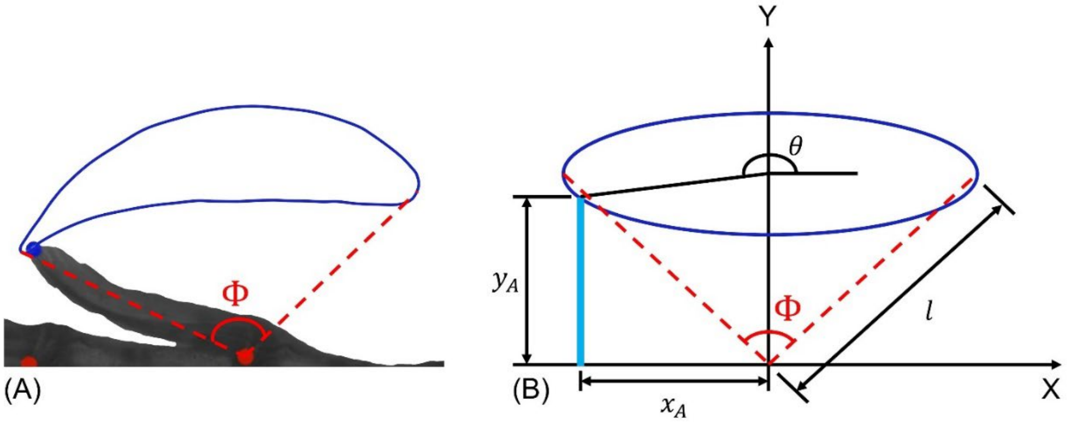

Figure **3-1.** (A) Sample trajectory of a real ctene and (B) simplified elliptical trajectory for the analytical model. Thin solid lines (dark blue) depict tip trajectories; the thick solid line (light blue) represents an oscillating plate whose tip position (x_A, y_A) is a function of θ and ellipse geometry. Dotted lines denote the stroke amplitude Φ. The spatiotemporal asymmetry parameters, Sa and Ta, are prescribed for each model run; these determine the time-varying tip position (x_A, y_A), which subsequently determines the oscillating plate's speed and flow-normal area on the power and recovery strokes. Reprinted with permission from (Herrera-Amaya et al., 2021).

The propulsive force generated by a single plate as a function of time is given by:

$$F_p = -\frac{1}{2}\rho C_A(\dot{x}_A + \dot{x}_B, f) w y_A [(\dot{x}_A + \dot{x}_B)|\dot{x}_A + \dot{x}_B|] \quad (3)$$

where ρ is the fluid density, w is the width of the appendage, $\dot{x}_B$ is the body's swimming speed, and C_A is the plate drag coefficient. C_A is a function of both the plate's absolute speed $\dot{x}_A + \dot{x}_B$ and its oscillation frequency f, following (Shih & Buchanan, 1971). Further details are given in Appendix A.3.2.

To consider multiple appendages operating at a phase lag, we sum equation (3) over n plates:

$$F_{net} = -\frac{1}{2}\sum_{k=1}^{n} \rho C_A(\dot{x}_A + \dot{x}_B, f) w y_A(t + (k-1)\tau)[(\dot{x}_A(t + (k-1)\tau) + \dot{x}_B)|\dot{x}_A(t + (k-1)\tau) + \dot{x}_B|] \qquad (4)$$

By dephasing the position variables x_A and y_A by an amount $(k-1)\tau$, we introduce metachronal coordination (where $\tau = P_L \cdot T$). The model does not consider inter-appendage interactions, so it is not affected by the spacing between appendages (unlike a real ctenophore).

3.1.1 Spatiotemporal asymmetry in a single appendage

We compute the total propulsive force (averaged over one cycle) for a single ctene on a fixed substrate ($\dot{x}_B = 0$), modeled by equation (3). Because of its dependence on x_A and y_A (which are prescribed—see Appendix A1), F_p is implicitly a function of Sa, Ta, Φ, and f. Increasing Φ increases the magnitude of F_p but does not change Re_ω, which is based only on oscillation frequency and ctene length; we therefore set Φ to a fixed value ($\Phi = 100°$). We compute F_P for a ctene with $l = 1$ mm, with w assumed to be $l/2$ (Afzelius, 1961), and beating at frequencies corresponding to Re_ω between 5 and 200 (Afzelius, 1961; Matsumoto, 1991). For each frequency, we continuously vary spatial and temporal asymmetry ($0.1 < Sa < 0.6$ and $0.1 < Ta < 0.6$).

To examine the effect of varying spatiotemporal asymmetry throughout the parameter space, we calculate the gradient of F_p with respect to Sa and with respect to Ta throughout the tested $Sa - Ta$ space. That is, we calculate two partial derivatives: $\partial F_p/\partial Sa$, the rate of change of F_p with respect to Sa, and $\partial F_p/\partial Ta$, the rate of change of F_p with respect to Ta. We compare the value of these two quantities over the full range of asymmetry observed in the behavioral experiments. These derivatives measure how strongly F_P depends on either Sa or Ta; for example, if $\partial F_p/\partial Sa$ is small but $\partial F_p/\partial Ta$ is large, this means that force production is more sensitive to changes in temporal asymmetry than changes in spatial asymmetry (as we have defined them).

We find that $\partial F_p/\partial Sa > 0$ and $\partial F_p/\partial Ta > 0$ always, indicating that an increase in either Sa or Ta increases propulsive force. However, F_p is influenced differently by changes in Ta or Sa in different regions of the parameter space, depending on Re_ω. To measure their relative influence, we define the operator $G(\cdot) \equiv \frac{\partial(\cdot)}{\partial Ta}/\frac{\partial(\cdot)}{\partial Sa}$, so that $G(F_p) = \frac{\partial F_p}{\partial Ta}/\frac{\partial F_p}{\partial Sa}$. A high value of $G(F_p)$ indicates that propulsive force is more sensitive to changes in Ta; a low value of $G(F_p)$ indicates that propulsive force is more sensitive to changes in Sa. $G(F_p)$ is, therefore, a summary variable that quantifies the behavior of F_p with respect to Sa and Ta.

Figure 3-2A shows $G(F_p)$ averaged over $Sa - Ta$ space as a function of Re_ω. At lower Re_ω, the influence of Sa is higher than that of Ta, as expected from stronger viscous effects. However, as we increase Re_ω, $G(F_p)$ increases as well, making Ta the most influential asymmetry as inertia starts to dominate. Recall from Figure 2-5 that in our experimental observations, Sa decreases and Ta increases as Re_ω increases. This trend is corroborated by the value of $G(F_p)$ shown in Figure 3-2A. An increasing value of $G(F_p)$ corresponds to a higher sensitivity of F_p to changes in Ta; in other words, it is easier to boost force production by increasing Ta than by increasing Sa as Re_ω increases.

Figure 3-2B-E shows the value of F_P for several discrete values of Re_ω, over the full range of Sa and Ta considered. The role of Sa vs. Ta can be inferred from the slope of the contours: a very shallow slope indicates that F_P is very sensitive to Sa, and a very steep slope indicates that F_P is more sensitive to Ta. At low Re_ω, spatial asymmetry is at its highest level of influence; the slope of the contours is fairly uniform across $Sa - Ta$ space, indicating that F_P changes slightly favor Sa over Ta in the same manner for all points in this space. As Re_ω increases, the contours steepen: a change in Ta produces a higher F_P than a similar change in Sa. As is expected, the influence of Ta is weaker at lower Re_ω, where the flow approaches time-reversible conditions (however, the drag coefficient in our model is not appropriate for these conditions, so we do not attempt to extend the model to $Re_\omega < 1$ where the flow would be fully time-reversible). In general, the contours are shallowest (indicating maximal sensitivity to Sa) for low Ta; the contours are steepest (indicating maximal sensitivity to Ta) at high Ta.

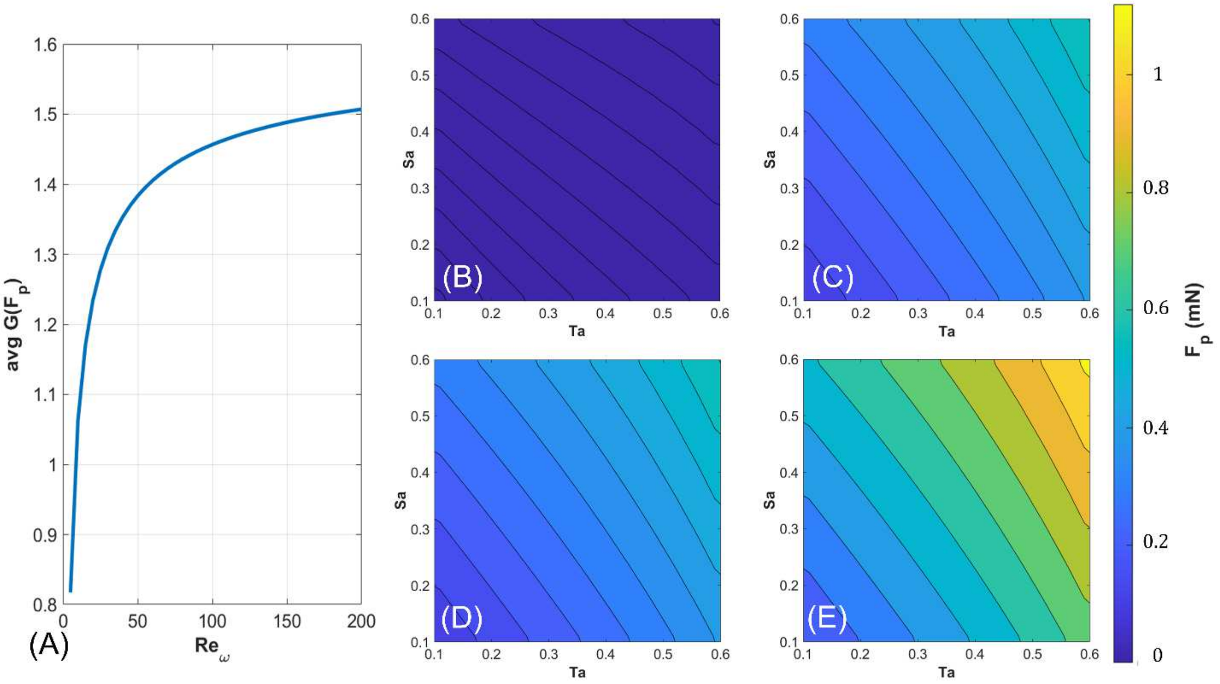

Figure **3-2.** (A) The ratio $G(F_p)$ of the gradients of F_p in $Sa - Ta$ space as a function of Re_ω, averaged over the tested parameter space. On the right, contour plots show the behavior of F_p for several values of Re_ω: (B) $Re_\omega = 5$, (C) $Re_\omega = 60$, (D) $Re_\omega = 145$, and (E) $Re_\omega = 200$. High Re_ω leads to Ta being more influential in force production than Sa, an effect that increases as Re_ω increases; for lower Re_ω, Sa more strongly influences force production. Reprinted with permission from (Herrera-Amaya et al., 2021).

3.1.2 Spatiotemporal asymmetry in metachronal rowing

To explore how spatiotemporal asymmetry can affect swimming efficiency, and to investigate the role of metachronal coordination, we consider several rows of oscillating plates as described by equation (4), unidirectionally propelling a spheroidal body. Drag on the spheroid is modeled as

$$F_D = -\frac{1}{2}\rho C_B(\dot{x}_B)\pi r^2 \dot{x}_B|\dot{x}_B| \qquad (5)$$

where C_B is the intermediate-Re drag coefficient for a prolate spheroid aligned with the flow, and is a function of its speed and geometry ((Loth, 2008); see Appendix A3.2); r is the average radius of the body's flow-normal area; and $\dot{x}_B$ is the overall swimming speed. Summing forces (propulsion, body drag, and acceleration reaction force) in the x-direction yields:

$$\ddot{x}_B + \frac{\rho\pi r^2}{2(m+\alpha\rho V)} C_B(\dot{x}_B)\dot{x}_B|\dot{x}_B| + \frac{N}{(m+\alpha\rho V)} F_{net}(Sa, Ta, \Phi, \mathrm{f}, P_L, \dot{x}_B) = 0 \qquad (6)$$

where N is the number of appendage rows (in ctenophores, $N = 8$), m is the body mass, α is the added mass coefficient (Daniel, 1983), and V is the spheroid volume. The "added mass" term ($\alpha\rho V$) accounts for displaced water that must be accelerated along with the body (Vogel, 1994). This approach allows us to compute the swimming efficiency η, which we calculate as the ratio of the output power (P_o) to the input power (P_i) ($\eta \equiv P_o/P_i$, see Appendix A2. To verify that our analytical model predicts forces comparable to those generated by the real animal it is meant to represent, we compare the model to actual measurements of freely swimming ctenophores from section 2.2.

Our model considers a ctenophore swimming in a straight line, with a constant beat frequency, whose body orientation is aligned with the swimming trajectory (heading angle of zero degrees). We consider two unidirectional swimming trajectories that resemble the modeled situation—one steady swimming animal, and one animal which accelerates from near rest. The beat frequency and phase lag were measured manually, counting the beat period of two neighboring ctenes from each visible ctene row on the three videos. Relevant morphometric and kinematic parameters can be found in Table 3-1.

Table **3-1.** Morphometric and kinematic measurements of observed animals (mean ± one standard deviation)

Body length (mm)	**Body width (mm)**	**No. Ctenes**	**Ctene length (mm)**	**Phase Lag (%)**	**Beat frequency (Hz)**
6.24	5.36	9	0.38	13.5±4.82	28.97±1.74
8.18	6.25	9	0.41	17.1±3.52	27.89±0.98

Based on these experimental observations, we run the swimming model (equation 6) with the values listed in Table 3-1, using the mean value for P_L and f. We also need to set values for Φ, Sa, and Ta; however, these are impossible to measure in our recordings due to a lack of spatial resolution. To measure Φ and Sa together with whole-body trajectories, we need a perfectly aligned view and an extremely high-resolution sensor given the range of sizes that must be resolved. For Ta, our 600 fps recordings are resolved enough in time to calculate the overall beat frequency of a ctene row, but not to finely measure power *vs.* recovery stroke duration (necessary to calculate Ta). We therefore use representative values of Φ, Sa, and Ta from our experimental observations (see Figure 2-5 and Table 2-3). The stroke amplitude shows almost no variation across our dataset; thus, we set it to the mean observed value of $112°$. Shaded areas in Figure 3-3 represent solutions for the entire Sa-Ta space considered in this section ($0.1 < Sa < 0.6$ and $0.1 < Ta < 0.6$). Blue lines in Figure 3-3 are the combinations of Sa and Ta that best predict the observed animal speed (red line), yielding $Sa = 0.55$ and $Ta = 0.35$ for the unsteady (accelerating) case and $Sa = 0.3$ and $Ta = 0.2$ for the steady swimming case. These values of Sa and Ta are within the experimental range observed in Figure 2-5. The agreement between observed and predicted swimming speeds shown in Figure 3-3 verifies that the model can produce similar propulsive forces as those generated by the animals.

For this parametric study, we consider a modeled ctenophore whose morphometric parameters are based on the experimental measurements of the second animal in Table 3-1. The geometry for the model is $L_b = 8.18$ mm, $l = 0.41$ mm, $n = 9$, and $d = 6.25$ mm. We solve equation (6) for a total of 40,000 combinations of Sa, Ta, Re_ω, and P_L (see Table 3-2), separating each solution into two sequential events: unsteady swimming (acceleration from rest) and steady swimming. Once the model reaches a steady speed, we continue to run the calculations until the model "swims" for three times its body length (Figure 3-4A). We note that oscillations in $\dot{x}_b$ are still present in the steady swimming portion for some values of P_L due to the time dependence of the metachronal motion.

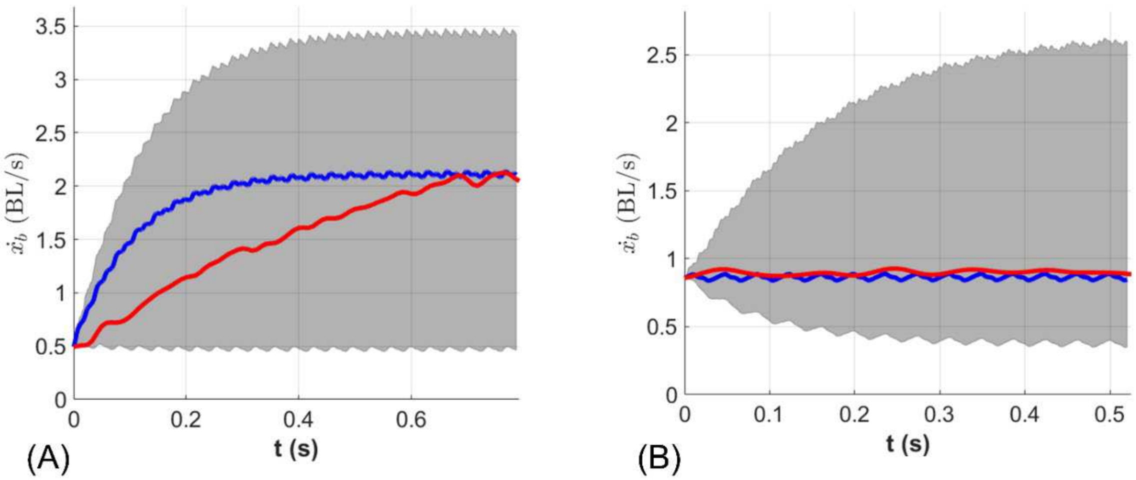

Figure 3-3. Comparison between experimental (red line) and modeled (blue line) swimming speed. The shaded area represents all Sa-Ta combinations considered in Figure 3-2. (A) shows an animal accelerating from near rest. The modeled speed (blue line) has $Sa = 0.55$ and $Ta = 0.35$. (B) shows an animal swimming at a steady speed. The modeled speed (blue line) has $Sa = 0.3$ and $Ta = 0.2$. Reprinted with permission from (Herrera-Amaya et al., 2021).

We find that swimming efficiency η depends only weakly on Re_ω during both unsteady and steady swimming throughout the tested parameter space; η varies less than 1% for each $Sa - Ta$ combination across the tested range of Re_ω. However, efficiency does depend on the other parametrically swept variables (P_L, Sa, and Ta). Figure 3-4B shows a representative example of $\eta\ (P_L)$ (for $Sa = 0.4$ and $Ta = 0.3$), where η is calculated over the full duration of steady or unsteady swimming.

For unsteady swimming, there is a clear maximum efficiency at a slight phase lag; this peak appears for every $Sa - Ta$ combination at a phase lag of approximately $7.04 \pm 1.12\%$ (mean $\pm$ standard deviation). For steady swimming, the efficiency is largely independent of P_L (Figure 3-4B). We attribute this difference to the stronger influence of the added mass term (see equation (6)) during the acceleration, since this term is proportional to $\ddot{x}_b$. Any energetic advantage of metachronal coordination during steady swimming is likely to be due to hydrodynamic interactions between ctenes (de Brouwer et al., 2013; Ford et al., 2019; Ford & Santhanakrishnan, 2020), which are not captured here. While our model does not consider these interactions, we can consider how phase lag P_L affects oscillations in body speed $\dot{x}_b'$. Figure 3-4C shows that zero phase lag produces strong oscillations in body speed; however, $\dot{x}_b'$ is minimized for $P_L = 19.59\%$ (for the specific combination of $Sa = 0.4$ and $Ta = 0.3$). Averaged across the tested $Sa - Ta$ space, this minimum appears at $P_L = 20.11 \pm 0.46\%$ (mean $\pm$ standard deviation). This phase lag is close to what we observe experimentally (see Table 2-3) and also within the optimal P_L range reported for a krill-inspired robot ($16.7\% < P_L < 25\%$) (Ford et al., 2019) and by a krill-inspired numerical rowing model ($20\% < P_L < 25\%$) (Granzier-Nakajima et al., 2020). In our model, this corresponds to the range that produces the smallest values of $\dot{x}_b'$ (*i.e.*, the smoothest and least "jerky" swimming), though these are not necessarily the values that maximize swimming efficiency (η has no clear maximum for the steady-swimming portion of the modeled trajectory). These two cases (unsteady swimming at maximum η and steady swimming with a minimum $\dot{x}_b'$) represent cases of particular interest, which we will further explore in the next section.

This analysis highlights the importance of considering the added mass force as a significant component of propulsion at intermediate Re, especially during bouts of whole-body acceleration; it also highlights a correlation between the range of optimal phase lags found in other studies and the range of phase lags which here produced the smoothest modeled swimming speeds.

Table **3-2.** Range and resolution of the parameter sweep study.

	$\boldsymbol{Sa}$	$\boldsymbol{Ta}$	$\boldsymbol{f}$**(Hz)**	$\boldsymbol{Re_\omega}$	$\boldsymbol{PL}$ (%)
Range	0.2-0.6	0-0.6	10-30	10-30.1	0-30
Resolution	0.1	0.0316	1.0526	1.0526	1.5789

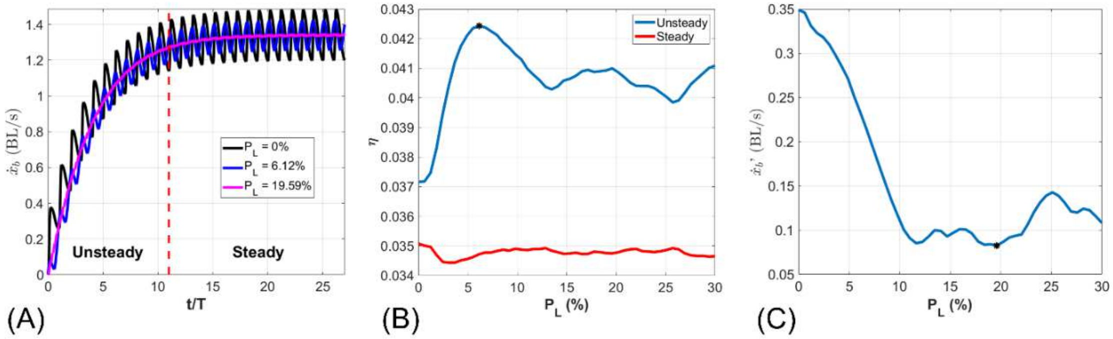

Figure 3-4. (A) Modeled swimming speed of a mid-size ctenophore ($L_b = 8.18$ mm, $l = 0.41$ mm, $n = 9$, and $d = 6.25$ mm) accelerating from rest at a beat frequency of $f = 20$ Hz (Re_ω =20.1) with $Sa = 0.4$ and $Ta = 0.5$. The black line shows the highest oscillations in speed ($P_L = 0\%$), the blue line shows the phase lag that gives optimal efficiency for unsteady swimming ($P_L = 6.12\%$ for this specific case), and the magenta line shows the phase lag that reduces body speed oscillations to a minimum ($P_L = 19.59\%$ for this specific case). (B) Swimming efficiency $\eta \equiv \frac{P_o}{P_i}$ (ratio of power output to power input) as a function of phase lag for both the unsteady and

steady swimming period, as demarcated in panel (A). Efficiency is calculated over the entire unsteady/steady periods to obtain the results shown. Maximum efficiency (black dot) occurs at a phase lag of 6.12% during the unsteady period for this case; there is no clear maximum efficiency for the steady period. (C) Magnitude of swimming speed oscillations $\dot{x}_b{}'$ as a function of phase lag. Oscillations in $\dot{x}_b$ are minimized for this case at a phase lag of 19.59% (black dot). Reprinted with permission from (Herrera-Amaya et al., 2021).

3.1.3 Variation of swimming efficiency over *Sa-Ta* space

Previously, we used a gradient-based analysis to examine the sensitivity of propulsive force F_P to both Sa and Ta throughout $Sa - Ta$ space. However, this analysis considered a ctene on a fixed substrate, and thus could not include swimming efficiency. We extend this gradient-based analysis here to consider how Sa and Ta affect swimming efficiency η. The quantity $\mathrm{G}(\eta) = \frac{\partial \eta}{\partial Ta} / \frac{\partial \eta}{\partial Sa}$, defined for all points in $Sa - Ta$ space, represents the relative sensitivity of η to Ta *vs.* Sa. Recall that η is weakly dependent on beat frequency f; for unsteady swimming, η is maximized at a moderate phase lag P_L, and for steady swimming η depends only weakly on phase lag P_L. We consider a map of η over $Sa - Ta$ space for two cases of interest: A) unsteady swimming at $f = 20Hz$ and $P_L = 6.12\%$, which maximizes η, and B) steady swimming at $f = 20Hz$ and $P_L = 19.59\%$, which minimizes $\dot{x}_b{}'$ (Figure 3-4).

In general, efficiency η increases if either Sa or Ta increase, with a maximum at the edge of the considered parameter space where $Sa = 0.6$ and $Ta = 0.6$ (Figure 3-5A-B). However, efficiency is not dependent on Sa and Ta in the same way. This is apparent from the slope of the contours in Figure 3-5, and how they vary over $Sa - Ta$ space: very steep contours indicate higher sensitivity to Ta, and very shallow contours indicate higher sensitivity to Sa.

We find that η is more responsive to Ta than it is to Sa throughout $Sa - Ta$ space. The gradient ratio $G(\eta)$ is greater than one over nearly the entire parameter space considered, indicating that η is always more sensitive to changes in Ta versus changes in Sa. Interestingly, η is most sensitive to Sa at very high values of Sa for both unsteady and steady swimming. This means that when the stroke is very spatially asymmetric, further increases in Sa can still produce nontrivial increases in η; there is no saturation point. We note that the analysis in Figure 3-5 is representative of all tested frequencies ($10Hz < f < 30Hz$ and $10 < Re_{\omega} < 30$), and that $G(\eta)$ can be inferred from the shape of the contours of η.

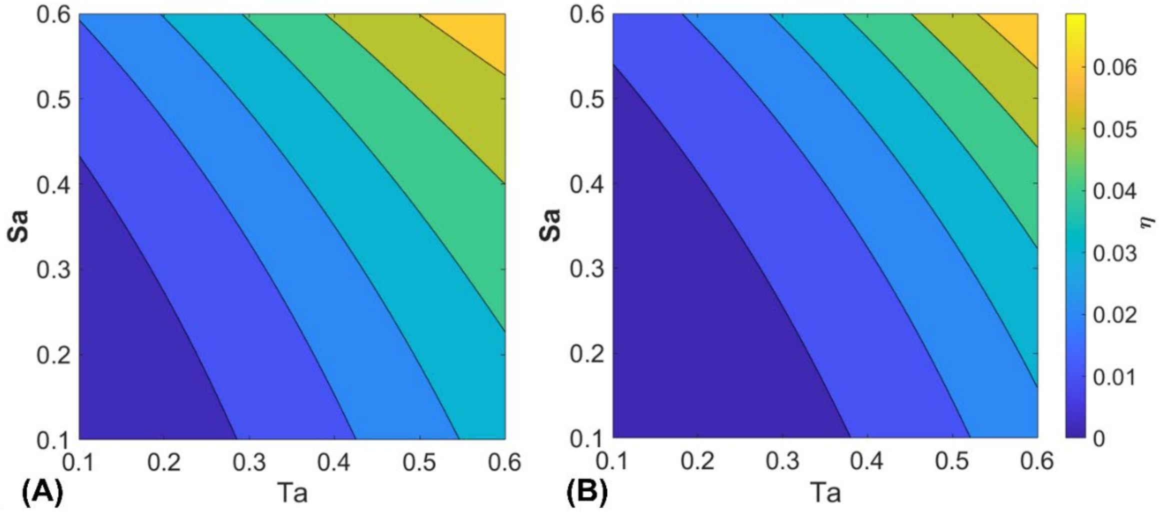

Figure **3-5.** Contours of swimming efficiency at $f = 20Hz$ ($Re_{\omega} = 20.1$) for (A) unsteady swimming, at $P_L = 6.12\%$ (which maximizes efficiency η) and (B) steady swimming, at $P_L = 19.59\%$ (which minimizes body speed oscillations $\dot{x}_b'$), throughout $Sa - Ta$ space. Reprinted with permission from (Herrera-Amaya et al., 2021).

3.1.4 Summary

Results from the single appendage model show that force production is more sensitive to temporal asymmetry (*vs*. spatial asymmetry) at higher Reynolds numbers. In general, the model results showed that the relative sensitivity to spatial vs. temporal asymmetry is a function of both Reynolds number and the position in $Sa - Ta$ space. This simple analysis would also dictate that increasing the spatiotemporal asymmetry always increases propulsive force generation. Since the experimental data do not suggest that animals always maximize both Ta and Sa (see section 2.1.4), we expanded the mathematical model to consider multiple rows of appendages propelling a freely-swimming model ctenophore to consider the energetic costs. Results showed that swimming efficiency η increases with both Sa and Ta, but that η is always more sensitive to changes in Ta than changes in Sa (and that η is most sensitive to Sa when Sa is already high). It is likely that Sa is somewhat passive – that is, some ctene deformation results from the fluid-structure interaction between the beating ctene, its material properties, and the surrounding flow (Colin et al., 2020). Ctenes become longer and thicker as an animal grows (Afzelius, 1961; Hernandez-Nicaise, 1991; Tamm, 2014), so the material properties of larger ctenes (which tend to beat at higher Re_ω) are different from those of smaller ctenes. It is, therefore, likely that some changes in Sa passively arise from variations in size and beat frequency. In other words, increasing beat frequency is correlated with increasing size, so a larger and faster animal may have lower Sa simply because ctenes have a higher bending modulus; Sa may remain low simply because it is not mechanically possible to increase it, even if doing so would increase force generation and/or efficiency. For these larger animals, which are observed to beat with lower Sa, increasing Ta represents a pathway to compensate for efficiency and speed losses (this is what we observe in the experimental data). The model shows that force production is generally more sensitive to Ta at higher Re_ω, making it easier to compensate for Sa losses as Re_{ω} increases. This is highly relevant for swimming animals, since it is likely that Ta is more actively controlled than Sa.

Further study is necessary to understand if and how ctenophores may actively control both the spatial and temporal asymmetry of the ctene beat cycle, as well as how the material properties of ctenes might dictate how Sa change passively with Re_{ω}. Because our model does not consider hydrodynamic interactions between ctenes, it only partially captures the effects of phase lag. Nonetheless, it predicts enhanced efficiency while the animal is accelerating with a slight phase lag, which we attribute to the role of the added mass force. For steady swimming, the model results show that phase lag affects neither the overall magnitude of the propulsive force nor the swimming efficiency. We know that this is not true, and that hydrodynamic interactions lead to increased efficiency for metachronal coordination relative to synchronous stroking (Granzier-Nakajima et al., 2020). However, even this simple model shows that there is an optimal phase lag to minimize unsteadiness in the swimming trajectory. This "smoothest trajectory" optimal phase lag was found to be similar to those which maximize efficiency in swimming animals and robots (Colin et al., 2020; Ford et al., 2019; Granzier-Nakajima et al., 2020; Murphy et al., 2011). Further exploration of the role of spatiotemporal asymmetry in rowing would greatly benefit from using flexible robotic models for which frequency and ctene structural properties can be varied. Section 4.1 describes a ctene-inspired robotic model and the roles of spatiotemporal asymmetry on propulsion efficiency in this context.

3.2 Ctenophore turning mechanics: 3D swimming equation

In this section, we expand the 1D swimming equation (6) to three dimensions and use it to complement our experimental observations of ctenophore maneuverability. The 3D reduced-order analytical model allows us to explore the kinematics resulting from the range of physically possible beat frequencies for each ctenophore turning mode (section 2.2). Unlike similar models, here we fully incorporate the combination of viscous and inertial effects, which arises at intermediate Reynolds numbers, by ensuring that relevant drag and torque coefficients are a function of the instantaneous speed and geometry of both the body and the ctenes. Based on the average body and appendage length (Table 2-5), the maximum recorded swimming speed $(2.7\ BL/s)$ and maximum beat frequency $(34\ Hz)$, we calculate body and appendage-based Reynolds numbers of 157 and 57 $(Re_b = UL/\nu$ and $Re_\omega = 2\pi f l^2/\nu)$, respectively.

We model the ctenophore as a self-propelled spheroidal body suspended in a quasi-static flow (Figure 3-6), whose motion is governed by the balance between the propulsive and opposing forces and torques. Table 3-3 lists all the model parameters. To describe the motion of the spheroidal body, we require two coordinate systems: a global (fixed) coordinate system, in which a vector is expressed as $\vec{x} = x_1\hat{e}_1 + x_2\hat{e}_2 + x_3\hat{e}_3$, and a body-based coordinate system in which $\vec{x}' = x_1'\hat{e}_1' + x_2'\hat{e}_2' + x_3'\hat{e}_3'$.

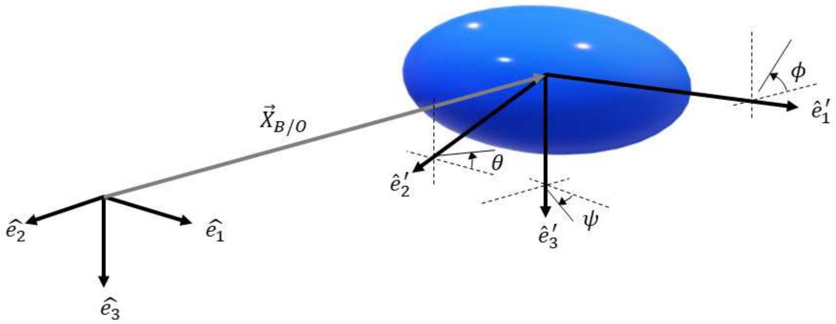

Figure **3-6.** Schematic of a ctenophore's simplified geometry moving in 3D space. The unit vectors $\hat{e}_1$, $\hat{e}_2$, and $\hat{e}_3$ define the global (fixed) coordinate system while $\hat{e}_1'$, $\hat{e}_2'$, and $\hat{e}_3'$ correspond to the moving coordinate system attached to the spheroidal body.

As is typical in vehicle dynamics (Schaub & Junkins, 2018), we relate the orientation between both coordinate systems by successive rotations: yaw (ψ, rotation about $\hat{e}_3'$), pitch, (θ, rotation about $\hat{e}_2'$) and roll (ϕ, rotation about $\hat{e}_1'$). The transformation between the global and body frames is given by $\vec{x}' = \boldsymbol{R}\vec{x}$, where the transformation (rotation) matrix is given by

$$\boldsymbol{R} = \begin{bmatrix} \mathrm{c}(\theta)\,\mathrm{c}(\psi) & \mathrm{c}(\theta)\,\mathrm{s}(\psi) & -\mathrm{s}(\theta) \\ \mathrm{s}(\phi)\,\mathrm{s}(\theta)\,\mathrm{c}(\psi) - \mathrm{c}(\phi)\,\mathrm{s}(\psi) & \mathrm{s}(\phi)\,\mathrm{s}(\theta)\,\mathrm{s}(\psi) + \mathrm{c}(\phi)\,\mathrm{c}(\psi) & \mathrm{s}(\phi)\,\mathrm{c}(\theta) \\ \mathrm{c}(\phi)\,\mathrm{s}(\theta)\,\mathrm{c}(\psi) + \mathrm{s}(\phi)\,\mathrm{s}(\psi) & \mathrm{c}(\phi)\,\mathrm{s}(\theta)\,\mathrm{s}(\psi) - \mathrm{s}(\phi)\,\mathrm{c}(\psi) & \mathrm{c}(\phi)\,\mathrm{c}(\theta) \end{bmatrix} \tag{7}$$

where (ψ, θ, ϕ) are the Euler angles, and $\mathrm{c}(\cdot)$ and $\mathrm{s}(\cdot)$ denote cosine and sine, respectively.

Table **3-3.** Reduced-order swimming model parameters. Vector quantities are expressed in the global frame unless marked with a prime (as in $\vec{\omega}'$).

Variable	**Description**
ψ, θ, ϕ	Euler angles (yaw, pitch, and roll)
$\vec{F}_{net}$	Net propulsive force
$\vec{F}_D$	Body drag
$\vec{F}_{AR}$	Acceleration reaction force
$\vec{X}_{B/O}$	Body position vector
m	Body mass
$\vec{T}'_{net}$	Net propulsion torque
$\vec{T}'_{op}$	Opposing torque
$\vec{\omega}'$	Angular velocity vector
$\boldsymbol{I}$	Moment of inertia matrix
$\boldsymbol{R}$	Rotation matrix
w	Plate width
y_A	Instantaneous plate length
x_A	Instantaneous plate oscillatory position
C_A	Plate drag coefficient
$\vec{u}$	Plate instantaneous velocity vector
C_B	Body drag coefficient
a	Body semi-minor axis
b	Body semi-major axis
$\vec{r}'$	Ctene position vector
τ	Phase lag time
C_m	Added mass coefficient
C_R	Torque coefficient

The differential equations describing the propulsion-opposing force balance are based on Euler's first and second laws (Equations (8) and (9)). Equation (8) balances the propulsive force $\left(\vec{F}_{net}\right)$, the drag force $\left(\vec{F}_D\right)$, the acceleration reaction force $\left(\vec{F}_{AR}\right)$, the body mass (m), and the body acceleration with respect to the origin $\left(\ddot{\vec{X}}_{B/O}\right)$. Equation (9) balances the propulsive torque $\left(\vec{T}'_{net}\right)$ and the opposing torque $\left(\vec{T}'_{op}\right)$ with the moment of inertia matrix $[I]$ and the body's angular velocity $(\vec{\omega}')$ and acceleration $\left(\dot{\vec{\omega}}'\right)$. We will define each one of these terms in the following subsections. However, we direct the reader to the supplementary material for details of the solution procedure, the numerical implementation, the formulations for various coefficients, and the validation of the model against experimental data.

$$\vec{F}_{net} + \vec{F}_D + \vec{F}_{AR} = m\ddot{\vec{X}}_{B/O} \qquad (8)$$

$$\vec{T}'_{net} + \vec{T}'_{op} = [I]\dot{\vec{\omega}}' + \vec{\omega}' \times ([I]\vec{\omega}') \qquad (9)$$

For the 3D model, we consider each ctene as an oscillating flat plate with a time-varying length, just as in the 1D model (Figure 3-1). However, in this case, the flat plate proximal end oscillates along a plane tangent to the body surface (Figure 3-7D). We “place” a modeled ctene in each of the ctene positions (determined by ε, δ, and κ, coupled with the body geometry (Table 2-5 and Figure 2-7)) around the spheroidal body (Figures 3-7A and C). Each ctene oscillates around its initial position (Figure 3-7D), creating a force tangential to the body surface. The total propulsive force of the i^{th} ctene row is modeled as the negative of the drag force summed over each of n oscillating plates:

$${}_{i}\vec{F} = -\frac{\rho w}{2} \sum_{k=1}^{n} {}_{ik}y_A \;\; {}_{ik}C_A \;\; \left[\left| \dot{\vec{X}}_{B/O} + {}_{ik}\vec{u} \right|^2 \frac{{}_{ik}\vec{u}}{\left| {}_{ik}\vec{u} \right|} \right] \qquad (10)$$

where ρ is the fluid density, and n is the number of ctenes in a given row (k is the index of the ctene). The flow-normal area is given by the plate width w (assumed to be $0.5 \cdot l$) times the instantaneous plate length ${}_{ik}y_A$ $(t + (k-1)\tau)$. The drag coefficient ${}_{ik}C_A$ is that of an oscillating flat plate at an intermediate Reynolds number and is a function of the instantaneous plate speed $\dot{x}_A$ (Shih & Buchanan, 1971). The force is proportional to the square of the magnitude of the global ctene velocity vector $\dot{\vec{X}}_{B/O} + {}_{ik}\vec{u}$, where $\dot{\vec{X}}_{B/O}$ is the body velocity with respect to the origin and ${}_{ik}\vec{u}$ is the velocity of the k^{th} plate in the i^{th} row in the global frame, which is itself a function of the instantaneous plate oscillatory speed ${}_{ik}\dot{x}_A\ (t + (k-1)\tau)$:

$$ {}_{ik}\vec{u} = \boldsymbol{R}^T\ {}_{ik}\dot{x}_A\ \left[c(\ {}_k\lambda)\hat{e}_1' + s(\ {}_k\lambda)c(\ {}_i\varepsilon)\hat{e}_2' + s(\ {}_k\lambda)s(\ {}_i\varepsilon)\hat{e}_2'\right] \qquad (11) $$

where ${}_k\lambda$ is the angle defining the tangent to the body surface at the k^{th} plate (see Figure 3-7D). Metachronal coordination is incorporated by dephasing the plate kinematic variables ${}_{ik}\dot{x}_A$ and ${}_{ik}y_A$ by an amount $(k-1)\tau$, where $\tau = P_L \cdot T$. Considering all N ctene rows, the net propulsive force is

$$ \vec{F}_{net} = \sum_{i=1}^{N} {}_i\vec{F} \qquad (12) $$

Propulsive torque is calculated as the cross product of the ctene's position relative to the centroid of the body and the force generated by the ctene:

$$ \vec{T}_{net}' = \sum_{i=1}^{N}\sum_{k=1}^{n} {}_{ik}\vec{r}' \times -\frac{\rho w}{2}\mathbf{R}\left[{}_{ik}y_A\ {}_{ik}C_A\ \left(\left|\dot{\vec{X}}_{B/O} + {}_{ik}\vec{u}\right|^2 \frac{{}_{ik}\vec{u}}{\left|{}_{ik}\vec{u}\right|}\right)\right] \qquad (13) $$

where ${}_{ik}\vec{r}'$ is the position vector of the k^{th} ctene in the i^{th} row (relative to the body centroid), and the bracketed term is the ctene propulsion force in the global frame of reference. To calculate the propulsive torque, the propulsive force must be expressed in the body frame of reference; hence, we multiply it by the transformation matrix $\boldsymbol{R}$.

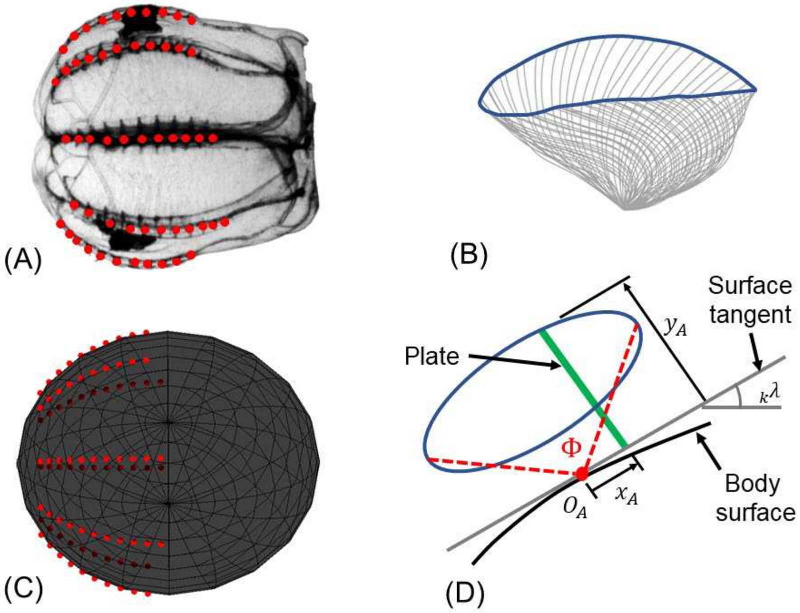

Figure **3-7**. Ctenophore reduced-order modeling. (A) Lateral view of a ctenophore; red dots mark the position of the ctenes that circumscribe its body in eight rows. (B) Real ctene tip trajectory from a tracked time series of ctene kinematics (gray lines, spaced equally in time). (C) Ctenophore modeled as a spheroidal body; red dots indicate the application point for each modeled (time-varying) ctene propulsion force. (D) Simplified elliptical trajectory for a modeled ctene, which is a flat plate with time-varying length. The plate oscillates parallel to a plane tangent to the curved surface of the modeled body (${}_k\lambda$, tangential angle to the body surface). The time-varying tip position (x_A, y_A) is prescribed as a function of the five ctene beating control parameters: f, Φ, l, Sa, and Ta.

The drag force on the 3D spheroidal body is:

$$\vec{F}_D = -\mathbf{R}^{\mathbf{T}}\frac{\rho}{2}\begin{bmatrix}(\pi a^2)C_B^{\parallel}\left(\left(\mathbf{R}\dot{\vec{X}}_{B/O}\left|\dot{\vec{X}}_{B/O}\right|\right)\cdot\hat{e}_1'\right)\\(\pi ab)C_B^{\perp}\left(\left(\mathbf{R}\dot{\vec{X}}_{B/O}\left|\dot{\vec{X}}_{B/O}\right|\right)\cdot\hat{e}_2'\right)\\(\pi ab)C_B^{\perp}\left(\left(\mathbf{R}\dot{\vec{X}}_{B/O}\left|\dot{\vec{X}}_{B/O}\right|\right)\cdot\hat{e}_3'\right)\end{bmatrix} \qquad (14)$$

Because the body is spheroidal, we must consider two drag coefficients: $C_B^{\parallel}$ is the drag coefficient for the longitudinal movements (roll axis, $\hat{e}_1'$), and $C_B^{\perp}$ is the drag coefficient for the lateral movements (pitch and yaw axes, $\hat{e}_2'$ & $\hat{e}_3'$). Because we are in the viscous-inertial (intermediate Reynolds number) regime, $C_B^{\parallel}$ and $C_B^{\perp}$ are each a function of both speed and geometry (Loth, 2008). These coefficients are multiplied by the respective velocity squared components (transformed to the body frame of reference by the transformation matrix $\boldsymbol{R}$), the corresponding flow normal area (πa^2, for $C_B^{||}$, and πab, for $C_B^{\perp}$), the fluid density, and a factor of 1/2. Finally, to transform the components of the drag force back to the global frame of reference, we multiply by the transpose of the transformation matrix $\mathbf{R^T}$. The drag force on the ctenes has already been incorporated as part of ${}_i\vec{F}$, which opposes the direction of motion during the ctene's recovery stroke.

The acceleration reaction (added mass) force is calculated as $C_m \rho V$, where ρ is the fluid density, V is the body volume, and C_m is the added mass coefficient, which depends on the body shape and the direction of motion (Brennen, 1982). We need two added mass coefficients for our spheroidal body: $C_m^{\parallel}$, for motion along the roll axis, and $C_m^{\perp}$, for motion along the pitch/yaw axes (Horace, 1993). Similar to the derivation of the drag force (Equation (14)), we have:

$$\vec{F}_{AR} = -\boldsymbol{R}^{\mathbf{T}} \rho V \begin{bmatrix} C_m^{\parallel}\left(\mathbf{R}\ddot{\vec{X}}_{B/O} \cdot \hat{e}_1'\right) \\ C_m^{\perp}\left(\mathbf{R}\ddot{\vec{X}}_{B/O} \cdot \hat{e}_2'\right) \\ C_m^{\perp}\left(\mathbf{R}\ddot{\vec{X}}_{B/O} \cdot \hat{e}_3'\right) \end{bmatrix} \qquad (15)$$

Finally, we model the overall resistance to body rotation, notated as the opposing torque $\left(\vec{T}'_{op}\right)$. The opposing torque comes from both viscous drag and acceleration reaction forces; however, an analytical formulation of this torque is outside the scope of this model. Here we use an expression based on torque coefficients for rotating prolate spheroids at intermediate Reynolds numbers, which are taken from numerical simulations (Zastawny et al., 2012):

$$\vec{T}'_{op} = -\frac{\rho}{2}\left(\frac{d_e}{2}\right)^5 \begin{bmatrix} sgn(\omega'_x)C_R^{\parallel}\omega_{x'}^2 \\ sgn(\omega'_y)C_R^{\perp}\omega_{y'}^2 \\ sgn(\omega'_z)C_R^{\perp}\omega_{z'}^2 \end{bmatrix} \qquad (16)$$

where d_e is the equivalent sphere diameter (i.e., the diameter of a sphere with the same volume as the spheroid), $C_R^{\parallel}$ is the torque coefficient for rolling, and $C_R^{\perp}$ for pitch and yaw. Both coefficients are a function of angular speed and geometry (see Appendix A4. The sign function is introduced so the resistive torque always opposes the body motion.

3.2.1 Swimming model verification

To confirm that our reduced-order model can estimate the forces and torques present in ctenophore swimming, we will compare the model predictions to freely swimming ctenophores. We considered two experimentally observed turning sequences: 1) mode 1, with only two active ctene rows, and 2) mode 3, with six rows beating at a higher frequency. Figure 3-8 shows the observed beat frequencies for the two active ctene rows for Sequence 1, measured by counting the beat period of ctenes on the three camera views. This sequence had $\overline{R/L} = 0.13$ and $\bar{V} = 0.4\ BL/s$. We run our reduced-order swimming model based on these observations and the morphometrics reported in Table 3-4. Figure 3-9A compares the experimental (red line) and predicted (blue line) swimming trajectory. As explained before, available camera resolution precludes simultaneous measurement of the ctene-level spatiotemporal asymmetries together with trajectory tracking; thus, the shaded areas in Figure 3-9A show the entire solution space ($0.1 < Sa < 0.6$ and $0.1 < Ta < 0.6$), and the blue solid line is the best prediction for this case (taking $Sa = 0.2$ and $Ta = 0.6$, both reasonable values). Figure 3-9B shows the experimental tracked triangle (red, formed by the tentacular bulbs and the apical organ; see Figure 2-6) *vs.* and the predicted triangle (blue) for different time points ($t = 0, 1.5, and\ 2.5\ s$). The agreement between the experimental and predicted triangles shows the model's capacity to predict the animal's orientation.

Table **3-4.** Morphometric measurements of observed animals

Maneuver	$L_B(mm)$	$d_B(mm)$	$l(mm)$	s	n_S	n_T
Mode 1	7.42	7.68	0.43	0.6	10	9
Mode 2	8	5.07	0.47	1.2	9	7

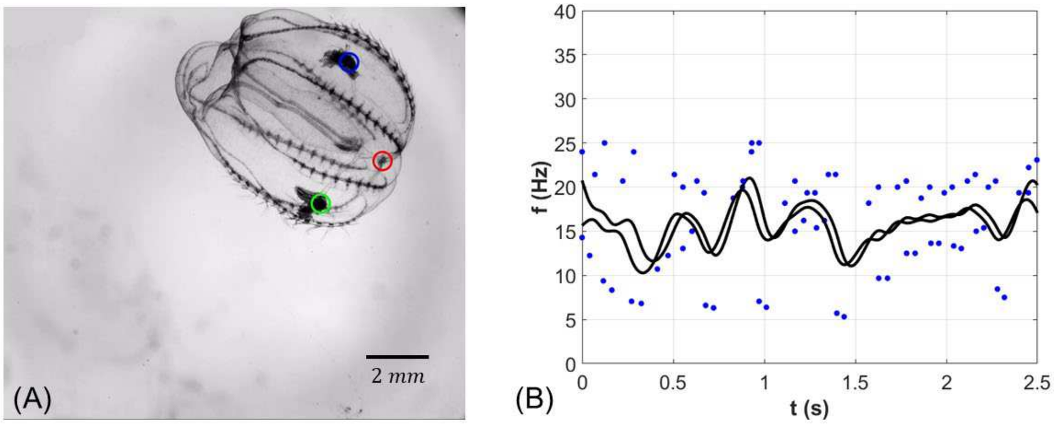

Figure **3-8.** Beat frequency measurements for the mode 1 turning trajectory**.** (A) Snapshot of freely swimming ctenophore and the tracked points: apical organ (red) and tentacular bulbs (blue and green). (B) shows the direct frequency measurements for ctene rows 4 and 5 (bottom ctene rows). Dots represent measurements, and the fitted black line is used as an input to calculate the kinematics of the oscillating plates in the mathematical model.

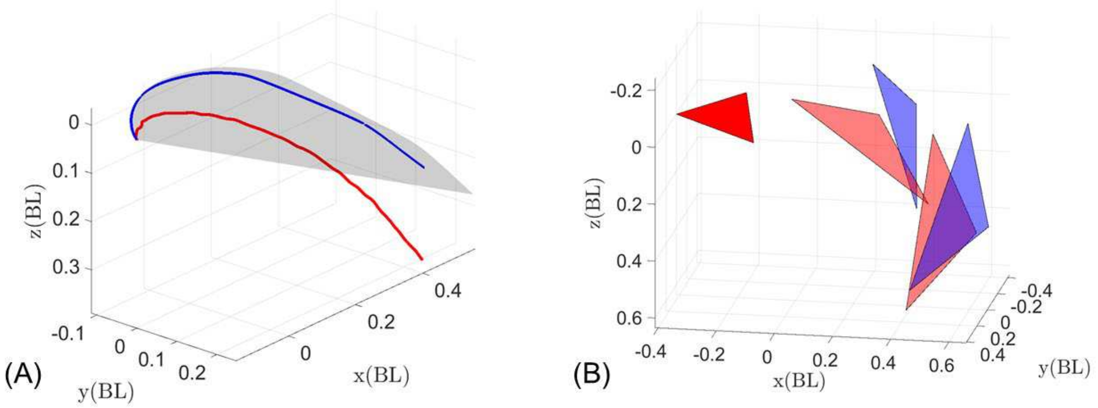

Figure **3-9**. Comparison between experimental measurements (red) and mathematical predictions (blue) for the mode 1 turning trajectory**.** (A) shows experimental vs predicted swimming trajectories. The shaded area shows the entire spatiotemporal solution space ($Sa - Ta$), while the blue line is the best model prediction ($Sa = 0.2$ and $Ta = 0.6$). (B) shows experimental vs predicted swimming orientation. The red triangles show the experimental positions for the tentacular bulbs and the apical organ for different time points t = 0, 1.5, and 2.5s. The blue triangles are the best fit ($Sa = 0.2$ and $Ta = 0.6$) predicted positions for the same time instants.

For the second case (mode 3), Figure 3-10 shows the beat frequencies for each of the eight ctene rows. Here turning is powered mainly by ctene rows 7 and 8 (Figures 3-10H and I), which beat with a lower frequency for the first second. This results in $\overline{R/L} = 0.08$ and $\bar{V} = 0.24\ BL/s$. Figure 3-11A compares the experimental (red line) and predicted (blue line) swimming trajectory, and the shaded areas in Figure 3-11A show the entire solution space ($0.1 < Sa < 0.6$ and $0.1 < Ta < 0.6$). For this case, the best prediction (blue line) has asymmetry values of $Sa = 0.18$ and $Ta = 0.18$. Figure 3-11B shows the experimental tracked triangle (red), and the predicted triangle (blue) for different time points ($t = 0, 1.5, and\ 3\ s$).

Both comparisons show that our highly simplified mathematical model can predict propulsion and opposing forces/torques similar to those experienced by a swimming ctenophore.

Therefore, we are justified in using this model for our parametric exploration of the maneuverability and agility of the ctenophore body plan and locomotion strategy.

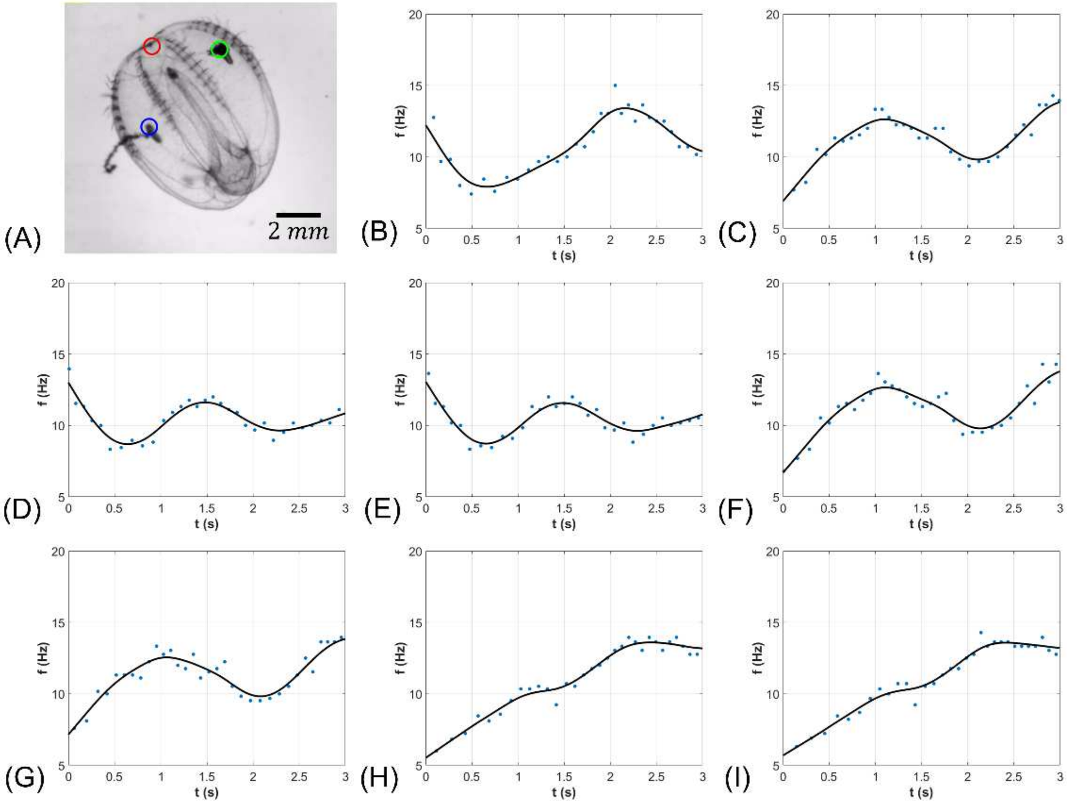

Figure **3-10.** Beat frequency measurements for the mode 3 turning trajectory. (A) Snapshot of freely swimming ctenophore and tracked points: apical organ (red) and tentacular bulbs (blue and green). (B) to (I) show the direct frequency measurements for ctene rows 1 to 8. Dots represent measurements, and the fitted black line is used as an input to calculate the kinematics of the oscillating plates in the mathematical model.

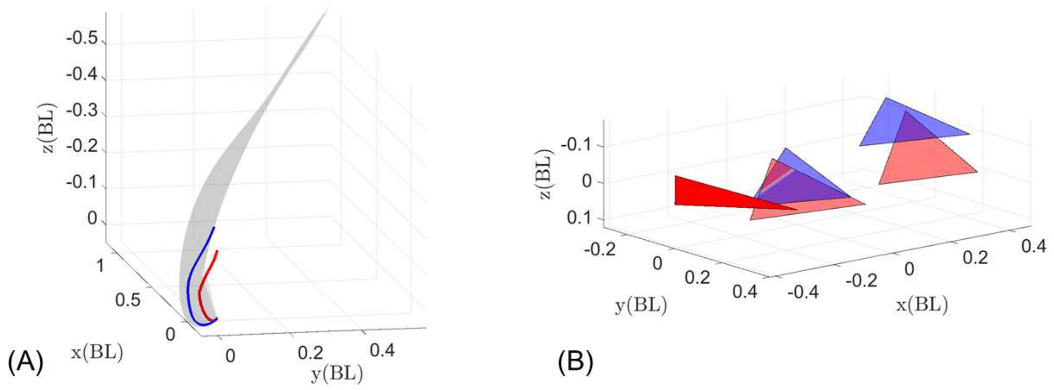

Figure **3-11.** Comparison between experimental measurements (red) and mathematical predictions (blue) for the mode 3 turning trajectory. (A) shows experimental vs predicted swimming trajectories. The shaded area shows the entire spatiotemporal solution space $(Sa - Ta)$, while the blue line is the best model prediction ($Sa = 0.18$ and $Ta = 0.18$). (B) shows experimental vs predicted swimming orientation. The red triangles show the experimental positions for the tentacular bulbs and the apical organ for different time points = 0, 1.5, and 3s. The blue triangles are the best fit ($Sa = 0.18$ and $Ta = 0.18$) predicted positions for the same time instants.

3.2.2 Turning performance

We use the mathematical model to expand our analysis of *B. vitrea*'s turning performance by simulating all possible configurations of modes 1, 2, and 3 (as defined in section 2.2, Table 2-6). We ran a total of 612 simulations covering the range and resolution of the beat frequencies reported in Table 3-5. Each simulation continued until the average of the normalized radius of curvature $\left(\overline{R/L}\right)$ over two seconds (simulation time) reached steady-state, or if $\overline{R/L}$ exceeded 10, which we considered straight swimming. Figure 3-12 shows the simulated range (blue dots) with the experimental results (red dots, Figure 2-8). Our model predicts that *B. vitrea*'s locomotor system can reach $\overline{R/L} = 0.08$ at a speed of $\bar{V} = 0.58\ BL/s$ (lower-left corner of the MAP, maximizing maneuverability). However, the system is also capable of significant maneuverability at high speeds: in the lower-right corner of the MAP (highly maneuverable and agile), the system can reach a speed of $\overline{V} = 2.33\ BL/s$ for $\overline{R/L} = 0.98$. These two data points range from 24% to 93% of the simulated top speed ($V_{max} = 2.49\ BL/s$, with eight rows beating at $34\ Hz$), while maintaining a turning radius of less than one body length. The model results confirm that ctenophores' metachronal rowing platform is highly maneuverable and agile, with performance limits that may extend beyond our experimental observations.

Table **3-5.** Range and resolution of the frequencies used in the analytical simulations.

	$\boldsymbol{f_{out}\ (Hz)}$	$\boldsymbol{f_{in}(Hz)}$
Range	$2 - 34$	$0 - (f_{out} - 2\ Hz)$
Resolution	2	2

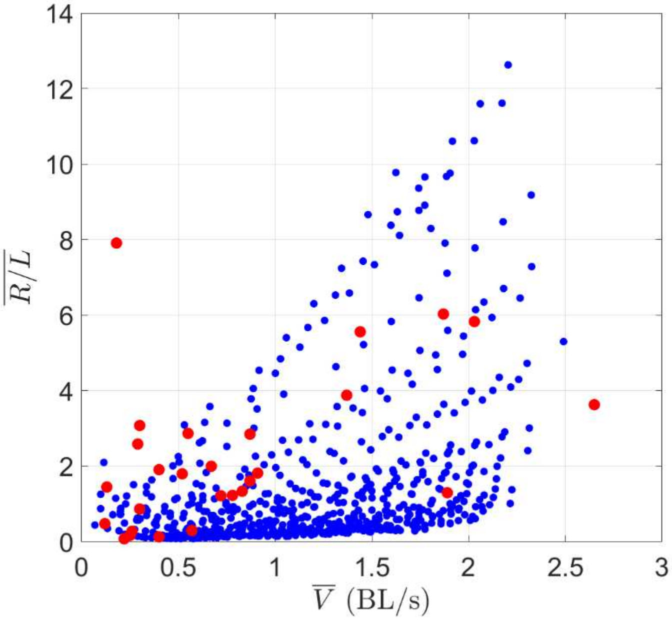

Figure **3-12**. Maneuverability-Agility Plot (MAP). Experimental measurements of freely swimming *B. vitrea* (red dots) and for all simulated cases of modes 1, 2, and 3 (blue dots). Lower values of $\overline{R/L}$ indicate sharp turns (more maneuverable); higher values of $\overline{V}$ indicate faster swimming (more agile). Values in the upper left (low $\bar{V}$, high $\overline{R/L}$) are straightforwardly achievable with straight swimming (mode 4) or with $\Delta f < 2Hz$; these points were not simulated. Simulating mode 4 mathematically would result in $\overline{R/L} \sim\infty$, since the eight rows beat at the same frequency. However, mode 3 will approach the behavior of mode 4 as $\Delta f = f_{out} - f_{in}$ approaches zero. Here, the minimum value is $\Delta f = 2Hz$, so the upper-left corner of the MAP is not occupied. Simulations were halted after the timestep in which $\overline{R/L}$ exceeded 10, resulting in some trials with $\overline{R/L}$ slightly greater than 10.

3.2.3 Omnidirectionality

To explore the omnidirectional capabilities of *B. vitrea* in a more systematic fashion, we use the mathematical model to explore all possible permutations of modes 1, 2, and 3. For simplicity and clarity, Figure 3-13 displays only trajectories produced by active rows beating at a frequency of $f_{out} = 30\ Hz$ and a $\Delta f = 30\ Hz$ (so that all other rows are not active), for a simulation time of one second. As expected by the number of active rows, mode 1 is the most maneuverable of the three (shortest trajectories, Figure 3-13A). In contrast, mode 2 and mode 3 reach higher speeds while turning (longer trajectories, Figure 3-13A). This suggests that activating only two ctene rows (mode 1) could be best suited for fine orientation control (for example, when maintaining a vertical orientation when resting/feeding)(Tamm, 2014). The higher number of active appendages used in modes 2 or 3 could be used for escaping, where both high speed and rapid reorientation are needed (Kreps et al., 1997). A front view of all modes (the y-z plane) displays the range of swimming directions accessible from a given initial position (Figure 3-13B). This MV—which captures only a fraction of the full capability of the swimming platform—shows the omnidirectionality of the ctenophore metachronal locomotor system, achieved only by constant pitching and yawing. In an actual swimming trajectory, a ctenophore can change the active rows, the frequency, or the turning mode over time, resulting in much more complex maneuvers (as in Figure 2-6).

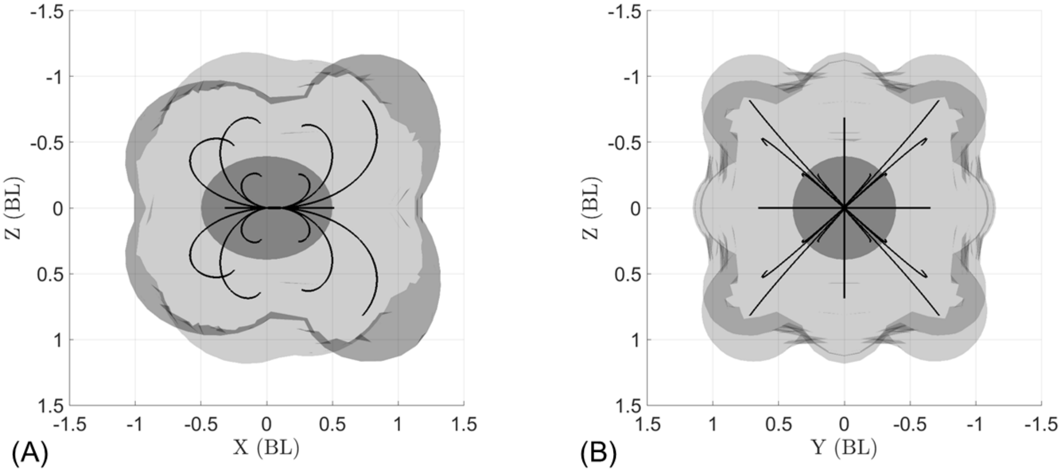

Figure **3-13.** Computationally simulated MV for the 3 ctenophore row control strategies, with a variable number of rows beating at 30 Hz, swimming either forward or backward, for a simulated time of one second. The darker gray ellipsoid placed on the origin illustrates the animal's initial position. (A) Side view displaying the backward (-x) and forward (+x) swimming trajectories. Asymmetry arises from the distribution of ctenes along the body. (B) Front view of the swimming trajectories, showing the wide range of turning directions.

To fully explore the maneuvering capabilities of the ctenophore body plan, we will explore the hypothetical case in which each ctene row has independent control. Figure 3-14 shows the MV for all 255 non-repeatable permutations of activating n_{cr} ctene rows at a time ($n_{cr} = 1,2,\ldots,8$) at 30 Hz for a simulation time of one second. This MV shows that nearly any swimming direction can be accessed from the same initial position.

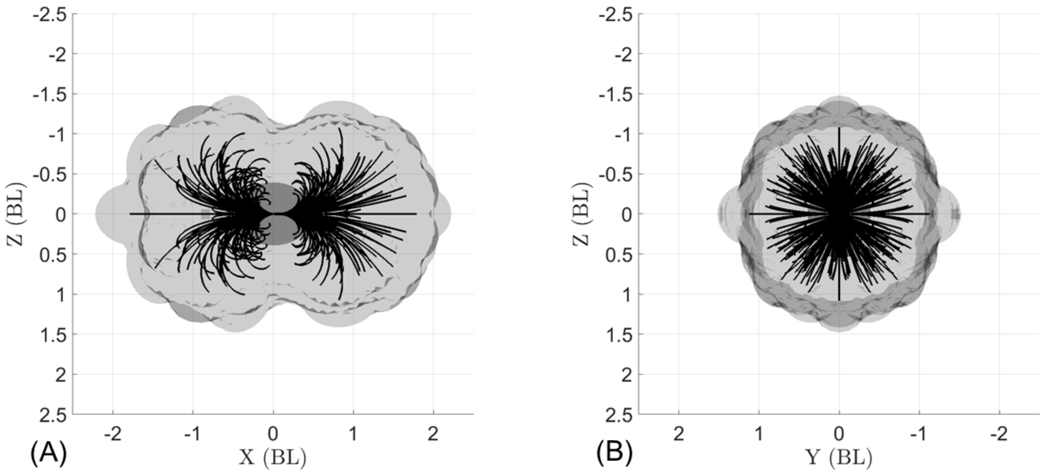

Figure **3-14.** Computationally simulated MV for 255 ctene row control strategies, with $1 \leq n_{cr} \leq 8$ rows beating at 30 Hz, swimming either forward or backward for a simulated time of one second. (A) Side view displaying the backward (-x) and forward (+x) swimming trajectories. (B) Front view of the swimming trajectories, showing the wide range of turning directions.

3.2.4 Summary

Results from the 3D swimming model show that metachronal swimming, particularly as used in the ctenophore body plan, allows for highly maneuverable/agile and nearly omnidirectional swimming. For the body plan studied here, which is typical of lobate ctenophores, we found that the asymmetric placement of ctenes within each row (i.e., ctenes distributed closer to the aboral than the oral end) enabled sharper turns during backward swimming when compared to forward swimming (Figure 3-13A). Ctene row asymmetries between the sagittal and tentacular rows of *B. vitrea* are due to the presence of the lobes (see Figure 1-4), which are used to create highly efficient feeding currents (Colin et al., 2010). However, cydippid ctenophores such as *Pleurobrachia* sp. feed by capturing prey with their tentacles, then bringing the prey to their mouth by rotating their bodies(Tamm, 2014). In *Pleurobrachia* and other cydippids*,* ctenes are approximately symmetrically arranged from the oral to aboral end, which may eliminate the trajectory asymmetries observed in lobate ctenophores. Cydippid ctenophore swimming may likely be even more omnidirectional. To accomplish their stereotypical rotating behavior, cydippid ctenophores also reverse the direction of the power stroke on the inner ctene rows, potentially leading to even tighter turns that are not captured in our model. Another lobate ctenophore genus, *Ocyropsis*, contracts its lobes (like the bell of a jellyfish medusa) to increase its escape velocity, while still using ctene rows for orientation (Gemmell et al., 2019); this indicates that ctene rows can be coupled with other propulsive strategies to achieve goals beyond that of maximizing maneuverability (*e.g.,* to increase overall swimming speed). Extinct ctenophores had as many as 80 ctene rows, increasing the number of reachable turning planes. Some even had ctene rows placed diagonally on the body, potentially allowing them to roll (Morris, 1996). Real ctenophores also use sporadic, irregular beating for fine-scale positional control, which is not captured in our model; this likely increases maneuverability beyond what we have predicted.

Chapter 4

Physical modeling and method development

This dissertation aims to explore the scaling of metachronal rowing from low to intermediate Reynolds numbers. This requires studying appendage kinematics and the resulting flows as the effects of inertia become more important—that is, as we move away from time-reversible flows ($Re \ll 1$). Our experimental observations of ctenophores (Chapter 2) show a general decrease in spatial asymmetry and increased temporal asymmetry with increasing Re (Figure 2-6). Because obtaining important functional relationships between parameters from behavioral experiments is difficult without large datasets, we turned to reduced-order models to study the impact of appendage kinematics on ctenophore swimming (Chapter 3). While this approach enables a more systematic exploration of the kinematic parameter space, it does not allow us to explore the details of flows produced by the appendages. To address this missing link, we developed a physical (robotic) model inspired by ctene kinematics. In Section 4.1, we describe this model and the produced flows across a range of Re and kinematic parameters, as well as a new metric to study rowing performance. Using the concept of Froude efficiency, we analyze how spatiotemporal asymmetry of beating affects thrust and lift production.

Section 4.2 outlines a key methodological innovation used here and in Chapter 2: a tracer detection/enhancement algorithm for Particle Shadow Velocimetry (PSV). PSV was initially developed as a micro-scale technique which uses optical elements to isolate the measurement plane (rather than a focused light sheet, as in the more commonly used Particle Image Velocimetry, PIV). Like PIV, PSV uses cross-correlation of image subwindows to infer the average displacement (and therefore velocity) of tracers over a Cartesian grid. In PSV, Depth of Correlation (DoC) refers to the thickness of the planar volume within which the imaged tracer shadows contribute to the measured subwindow cross-correlations, even if the tracers themselves are out of focus. Having a shallow DoC is crucial for obtaining accurate measurements of particle displacement. We chose to use PSV for all the velocimetry experiments in this dissertation because it is animal friendly (lacking laser light sources, which may cause damage or alter natural behavior), and because of its ability to resolve flow close to solid surfaces (no laser reflections). Additionally, PSV provides optical access not available with PIV, since the camera and light source lie along one single optical axis (rather than the orthogonal axes required by PIV, which often create shadowed regions where flow cannot be measured). However, our magnification requirements lead to nontrivial signal-to-noise ratios (large DoC), necessitating significant image preprocessing to improve data quality. Section 4.2 describes the image processing algorithm we developed to remove out-of-focus particles digitally, effectively providing an *a posteriori* reduction of DoC.

4.1 Ctene flexible robotic model

Animal experiments (Chapter 2) show that ctene rows can produce different flows in different contexts—that is, different individuals, different beating frequencies (and correspondingly different Re_ω), or other shifts in kinematics can produce categorically dissimilar velocity fields (section 2.1). Figure 2-4 shows the flows generated by two different animals; one produces a strongly tangential flow, while the other shows an increased presence of radial flow. Both cases have a similar Reynolds number ($Re_\omega = 23$ and $Re_\omega = 68$) and the same phase-lag (13%), but strongly differ in their spatiotemporal asymmetry ($Sa = 0.53$ *vs.* 0.29, with $Ta = 0.04$ *vs.* 0.15). Since the directionality of the flow affects the production of both thrust and lift, this also impacts the swimming dynamics of the animal. However, the effect of the paddle shape and motion asymmetries on rowing force production is not well understood. For a swimming body, thrust and lift are defined as the force parallel (thrust) and perpendicular (lift) to the swimming direction. In this chapter we focus on the local forces produced by a single appendage; thus, we will be referring to thrust as the horizontal force and lift as the vertical force. These are also the global thrust and lift directions if we assume the appendage is placed on a flat horizontal surface or body (Figure 4-1).

Here we perform experiments on three robotic paddles with different material flexibilities and geometries, allowing us to parametrically explore the effect of motion asymmetry on force production. To analyze our results, we developed a new efficiency expression with the potential to be implemented broadly in both animal experiments and numerical simulations. The new efficiency formulation is motivated by the fact that existing widely used measures of swimming efficiency—such as displacement efficiency (Ellington, 1984; Murphy et al., 2011), Froude efficiency (Gough et al., 2021; Jimenez et al., 2023; Lighthill, 1960; Mchenry et al., 1995), and cost of transport (Gemmell et al., 2013; Jahn & Seebacher, 2019; Tack & Gemmell, 2022)—all require the measurement of overall swimming speed, which is not applicable to directly evaluate the efficiency of a rowing appendage or set of appendages on their own. Analysis of a (globally) fixed set of rowing appendages is valuable in its own right, as this configuration occurs in many systems (Lim et al., 2019a; Milana et al., 2023; Park et al., 2016; Semati et al., 2020; Sensenig et al., 2009; Sensenig et al., 2010). This analysis is also a crucial step toward understanding a free-swimming system's propulsion dynamics. For example, in behavioral experiments it is often methodologically simpler to study tethered animals (Alben et al., 2010; Barlow & Sleigh, 1993; Colin et al., 2020; Herrera-Amaya et al., 2021). Numerical simulations often focus on fixed appendages due to their lower computational costs, since allowing the model to swim freely would require significant two-way coupling and large highly resolved meshes (Dauptain et al., 2008; Granzier-Nakajima et al., 2020; D. Lim et al., 2019a; R. Zhang et al., 2021). Lastly, initial robotic prototypes typically begin with a non-moving device to enable more thorough analysis of potential propulsive strategies (Ford et al., 2019; Gu et al., 2020; Kim & Gharib, 2011; Milana et al., 2020; Ren et al., 2022; Rockenbach et al., 2015; Saffaraval & Goudarzi, 2021; Santos et al., 2022).

Existing efforts to evaluate the performance of globally fixed rowing paddles typically calculate fluid dynamic parameters such as thrust/lift coefficients, impulse, and momentum fluxes (Ford et al., 2019; Kim & Gharib, 2011), or use dimensionless ratios such as flowrate-to-power (Dauptain et al., 2008; Granzier-Nakajima et al., 2020). Alternatively, the paddle is placed in an enclosed channel to evaluate the pumping performance by measuring the generated volumetric flow (Saffaraval & Goudarzi, 2021). In our work, we approach the problem by modifying the formulation of the Froude efficiency to consider the forces and velocities along the rowing paddle. With this new formulation, we can calculate thrust and lift efficiencies and visualize the paddle force distributions, thus helping us understand the role of the motion asymmetries on the overall propulsion dynamics.

4.1.1 Experimental facilities

The experimental setup consisted of a 3D printed paddle fixed to a steel shaft and mounted to a servomotor (300 Alacritous servo, Reefs RC, Corona, CA, USA), which rotated the shaft according to a prescribed time-varying angular displacement (Figure 4-1B). The paddle, shaft, and motor were submerged within an acrylic tank filled with a glycerol-water mixture; we adjusted the mixture proportions to achieve varying Reynolds numbers. Inside the tank, the servomotor was fixed to an acrylic plate and connected to the rowing paddle models via a timing belt (Figure 4-1B). Three different paddles were used in this experiment: one paddle was flat and rigid (made of PLA and printed using a MK3S+, Prusa Research, Prague, Czech Republic) and two paddles were flexible, with one initially flat geometry and one initially curved geometry (made of proprietary Elastic 50A resin, printed on a Form 2, Formlabs, Somerville, MA, USA). All paddles have dimensions of 1x30x120 mm (thickness, height, and width); the aspect ratio (width-to-height) is purposefully large so that the produced flow is approximately 2D. Figures 4-1C-E show camera recordings of the three different paddles. We will refer to the paddles as FR (flat and rigid), FF (flat and flexible), and CF (curved and flexible). The prescribed shaft rotation produced a power stroke and a recovery stroke whose durations could be adjusted, thereby varying temporal asymmetry Ta.

We used PSV to measure both flow velocities and paddle kinematics. The setup was similar to the one used in section 2.1, but used a macro lens instead of a long-working-distance microscope objective. Figure 4-1A shows the inline configuration of components; from left to right, we have a 4MP high-speed camera (Phantom VEO E-340L, Vision Research Inc., Wayne, NJ, USA), 105 mm F1.4 SIGMA lens (Ronkonkoma, NY, USA), the experimental tank with dimensions 560x150x250 mm (length, width, and height), a 6.7x6.7" Fresnel lens with a focal length of 6" (Edmund optics, Barrington, NJ, USA), and a white 10,000 lux LED panel (Charmax, China) as our light source. In this configuration, the LED panel produces diffuse light which is collimated as it passes through the Fresnel lens, producing sharply-defined shadows of tracer particles.

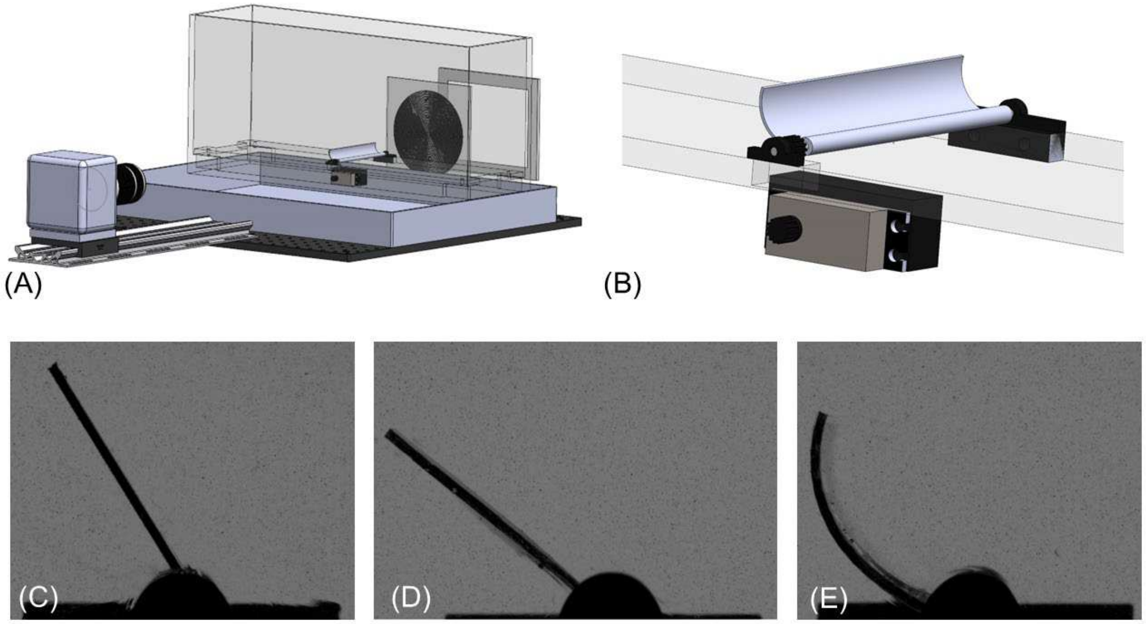

Figure **4-1.** (A) Schematic of experimental PSV setup showing the inline configuration of the camera, macro lens, water-glycerol tank with paddle, Fresnel lens, and light source. (B) Close-up of the paddle actuation system. (C) Flat and rigid paddle (FR) as seen by the camera. (D) Flat and flexible paddle (FF). (D) Initially curved and flexible paddle (CF).

4.1.2 Velocimetry and kinematics analysis

We recorded a side view of the paddle, as seen in Figure 4-1C-E, with the focal plane at the paddle's width midpoint to ensure observation of 2D flow. Images were collected at 300 frames per second with an exposure time of 900 μs. The Depth of Correlation (DoC), or thickness of the useful measurement volume, is estimated at 1.69 mm (equation 17, section 4.2), using 100 μm hollow glass silver-coated tracer particles (Conduct-o-fil, Potters Industries, Carlstadt, NJ, USA). To mitigate the noise created by out-of-focus particles, we used the pre-processing algorithm described in section 4.2. Processed images have an average seeding density of 2.08×10^{-3}

particles per pixel. We performed a vector computation (three-pass iteration with subwindows of 256x256, 128x128, and 64x64 px, with 50% overlap) using the MATLAB-based tool PIVLab (Thielicke & Stamhuis, 2014). All image pre-processing and vector field postprocessing was conducted with MATLAB (Mathworks Inc., Natick, MA, USA).

For each experiment, the paddle shaft's angular velocity was controlled via an Arduino Uno microcontroller board which oscillated the shaft in a temporally asymmetric beat cycle, with a net frequency of $1.07 \pm 0.2\ Hz$ and a stroke amplitude of $101.97 \pm 6.38°$ over ten cycles. To avoid start-up transients, only the last three cycles were recorded for analysis. This process was repeated for all three paddle types (FR, FF, and CF) using five levels of temporal asymmetry ($Ta = 0, 0.1, 0.2, 0.3, 0.4$) and four different Reynolds numbers ($Re_\omega = 7.43 \pm 0.24$, 14.87 ± 0.3, 27.40 ± 0.53, and 62.93 ± 1.11, where $Re_\omega \equiv 2\pi f l^2/\nu$), for a total of sixty experiments. To achieve this range of Re_ω, we varied the kinematic viscosity (ν) using water-glycerol mixtures. Specific viscosities were targeted using the work of (Brindise et al., 2018), and we directly measured viscosity using a Brookfield DV-E viscometer (Amtek, Inc., Berwyn, PA, USA). Fluid properties are shown in Table 4-1. We tracked the propulsor kinematics by automatically extracting the centerline of the paddle *via* image processing and interpolating 100 equally spaced points along the centerline. Figure 4-2A shows the centerline points (white dots; subsampled for visual clarity) used to calculate the speed along the paddle, as well as the tip trajectory for a single cycle (blue line). Figure 4-2B shows (for the CF paddle) the average tip velocities for the five levels of temporal asymmetry, consistent with our approach from Chapters 2 and 3.

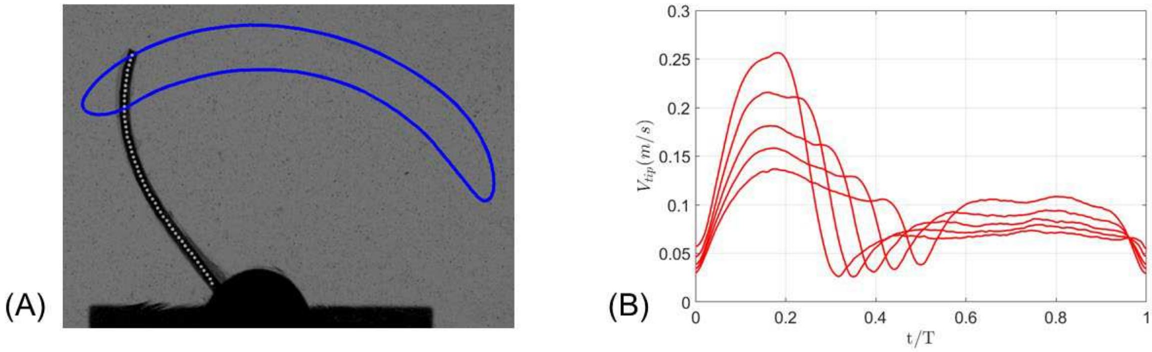

Figure **4-2.** (A) Example of a still frame from a collected video showing the tip trajectory (blue line) of the CF paddle and several tracked centerline points (white dots). (B) CF paddle tip velocity for $Ta = 0, 0.1, 0.2, 0.3, 0.4$. Red lines are the 3-cycle average velocity.

Table **4-1.** Fluid properties for the water-glycerol mixtures and the resulting oscillating Reynolds numbers (Re_ω).

$\boldsymbol{Re_\omega}$	**Density** $\boldsymbol{(kg/m^3)}$	**Kinematic viscosity** $\boldsymbol{(mm^2/s)}$
7.43 ± 0.24	1273.8	810.17
14.87 ± 0.3	1248.6	407.89
27.40 ± 0.53	1239.4	221.29
62.93 ± 1.11	1220.1	96.17

As previously mentioned, we are using three different paddles to explore the effects of propulsor shape and spatiotemporal asymmetry. Figure 4-3 shows the time series of the kinematics of these different paddles for the case of $Ta = 0.4$, displaying the power stroke tip trajectory in red and the recovery stroke tip trajectory in blue. Figure 4-3A shows the FR paddle, which has completely symmetric power and recovery strokes ($Sa = 0$). Figure 4-3B displays the kinematics of the FF paddle. In this case, the paddle bends more during the power stroke (left to right, red line) than during the recovery stroke (right to left, blue line), as the difference in speed passively deforms the paddle. This is the opposite of the appendages of actual ctenophores (Figure 2-2, section 2.1), in which the projected area in the plane normal to the body surface (transversal area) is increased during the power stroke and reduced during recovery (maximizing the ctene's local thrust production). To account for this possibility, in this chapter we use a more specific definition of spatiotemporal asymmetry (previously defined as $Sa = A_e/A_o$, equation 2, where A_e is the tip trajectory enclosed area and A_o is the ellipse inscribed in the ctene's reachable half-circle). We instead calculate A_e as the area under the power stroke trajectory (red line) minus the area under the recovery stroke trajectory (blue line), which does not alter the values of Sa reported in previous chapters but appropriately results in a negative spatial asymmetry for the flat/flexible paddle studied here. This negative value results from the paddle's passive bending due to the higher speed during the power stroke when $Ta \neq 0$. The third paddle (CF) is designed to mimic the spatial asymmetry of a real ctene ($Sa > 0$). In this case, the curved profile unrolls during the power stroke (increasing the transversal area), and returns to its original curvature during the recovery stroke, resulting in a positive spatial asymmetry.

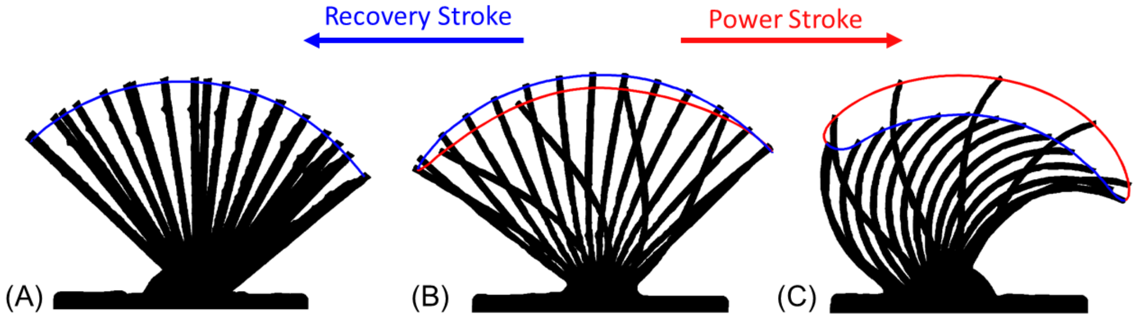

Figure **4-3**. Timeseries of the three different paddle kinematics, with paddle side profiles plotted at equal time intervals. Red lines are power stroke tip trajectories, and blue lines are recovery stroke tip trajectories. (A) shows the FR paddle; only the recovery stroke tip trajectory is visible due to complete spatial symmetry ($Sa = 0$). (B) shows the FF paddle; here, the paddle bends more during the power stroke than on the recovery stroke, resulting in a negative spatial asymmetry. (C) shows the CF paddle, which mimics the positive spatial asymmetry of a real ctene.

Due to its rigidity, the spatial asymmetry of the FR paddle is zero for all values of Ta and Re_ω. However, this is not the case for flexible paddles. For both FF and CF the spatial asymmetry is a passive response to the fluid forces acting on the paddles. Therefore, the value of Sa depends on Ta and Re_ω. Figure 4-4 shows the spatial asymmetry values for the FF (blue) and CF (magenta) as a function of temporal asymmetry and Reynolds number. The four Reynolds numbers $(Re_\omega = 7.43 \pm 0.24, 14.87 \pm 0.3\ , 27.40 \pm 0.53, \text{and } 62.93 \pm 1.11)$, are displayed by the color transparency level of the lines, with the most transparent being $Re_\omega = 7.43 \pm 0.24$ and the solid line $Re_\omega = 62.93 \pm 1.11$. The deformation of both paddles increases at higher values of Ta due to the higher speed during the power stroke (Figure 4-2B). The force is directly proportional to the square of the velocity $0.5\ \rho v^2 C_D A$. For the CF paddle, a higher force helps unroll the paddle and thus produce a higher Sa by extending the paddle during the power stroke. For the FF paddle, more force during the power stroke results on higher bending and therefore produces an increasingly negative value of Sa by collapsing the paddle during the power stroke. This same principle is invoked to show that the opposite trends hold when considering how Sa depends on Re_ω. From Table 4-1, we can observe that the fluid density decreases (ρ) as kinematic viscosity (ν) decreases, thereby increasing Re_ω (lowering the absolute force, $0.5\ \rho v^2 C_D A$, and resulting on less paddle deformation). This yields lower values of Sa as Re_ω increases for CF, and higher Sa as Re_ω increases for FF.

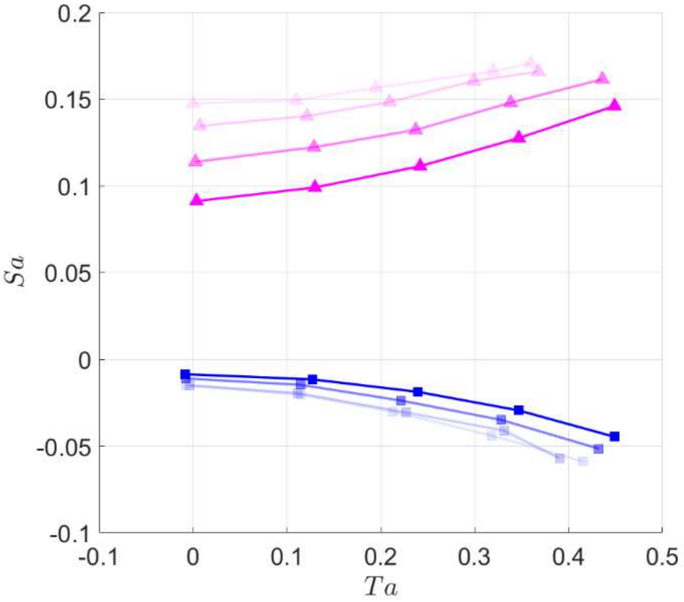

Figure **4-4**. Spatial asymmetry passively responds to fluid forces. The FF paddle is shown in blue, and the CF paddle in magenta. Experiments at different Reynolds numbers ($Re_{\omega} \equiv 2\pi f l^2/\nu$) are indicated by the line transparency. From the most transparent line to the solid line, Reynolds numbers vary across $7.43 \pm 0.24, 14.87 \pm 0.3$, $27.40 \pm 0.53,$ and 62.93 ± 1.11.

4.1.3 Rowing paddle dynamics

To evaluate rowing performance, we first calculate the force distribution over the paddle height. Using the measured velocity fields around the propulsor (Figure 4-5A), we solve the Navier-Stokes equation and compute the pressure field with the tool QUEEN 2.0 (Dabiri et al., 2014), which has previously been used to calculate pressure fields of ctene-generated flows (Colin et al., 2020). Figure 4-5B shows a sample pressure field for the FR paddle; here, the white-masked area denotes the solid region (paddle). On top of the computed pressure field, we plot the centerline of the paddle (blue line); we sample the pressure on both sides of the paddle over two transects parallel to and equidistant from the centerline (green dots). The time-varying force imparted by the paddle to the fluid can be calculated as follows:

$$\vec{F}(t) = \int \hat{n}\, P\, dA - \int \boldsymbol{\tau} \cdot \hat{n}\ dA \qquad (17)$$

where $\hat{n}$ is the normal unit vector directed outward from the centerline, P is the fluid pressure, $\boldsymbol{\tau}$ is the viscous stress tensor, and $\vec{F}$ is the force applied to the fluid by the paddle. Here we assume that the shear term is small relative to the pressure term, thus neglecting the last term of equation 17 (Lucas et al., 2017). Figure 4-5C shows a schematic of the centerline and the pressure sampling points. For each centerline point we use the unit normal to define two corresponding pressure sampling points to evaluate equation 17, such that there are two normal force vectors per centerline point. The net force for each centerline point is the vector sum of the two forces. The resulting force distribution is shown in Figure 4-5D, where the orange arrows correspond to the computed forces per unit length (2D flow), and the cyan arrows are the velocities for each point along the paddle. We note that force vectors for the rigid paddle are not strictly parallel due to a small errors produced by the automatic centerline identification; however, we do not consider this to be a significant source of error relative to existing noise in the velocity and pressure fields. We note that our analysis does not consider the hydrostatic pressure gradient; however, since each pair of sampled points is at approximately the same z-location, the pressure difference ΔP (and therefore net force) at each centerline point is independent of hydrostatic variation.

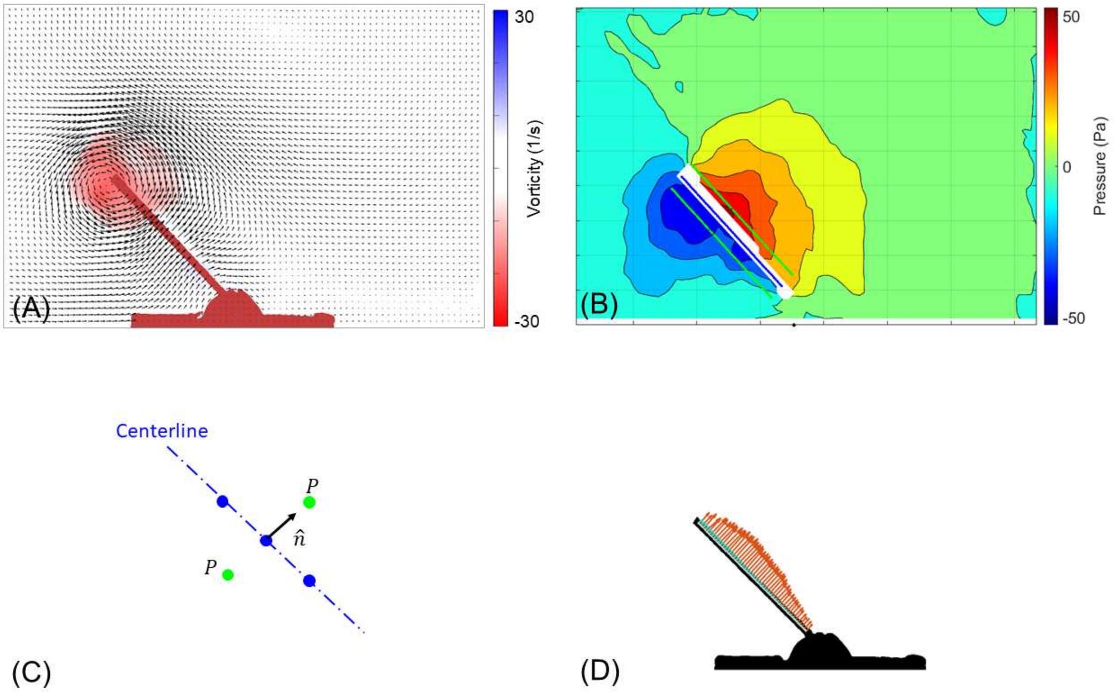

Figure **4-5**. Analysis procedure to calculate the force distribution along the paddle. (A) Velocity field from PSV experiments; colormap shows vorticity. (B) Pressure fields are computed by solving the Navier-Stokes equations using the measured velocity field as input and assuming out-of-plane velocities and velocity gradients are zero. (C) Schematic of the centerline and offset points used to evaluate equation 17; each point is a at an offset distance $d_o = 3.5\, mm$ from the centerline. (D) Force vectors (blue) and velocity vectors (red) along the paddle.

The analysis procedure assumes that we are sampling the pressure exactly at the solid-fluid interface; however, in practice we choose the minimum possible distance between the centerline and the sampling points so that we measure fluid pressure outside the masked region (white area, Figure 4-5B) during the complete cycle. The mask resolution is constrained by the PSV velocity vectors' cartesian grid positions, such that the masked region is slightly larger than the true paddle dimensions. Appendix B shows a sensitivity analysis of the sampling offset distance, similar to the one in (Lucas et al., 2017), and shows that similar values for net force are obtained at distances up to five times the paddle thickness (5 mm). This sensitivity analysis also justifies the neglect of the shear term in equation 17.

As a general example, we discuss the analysis for the case of $Re_{\omega} = 14.87 \pm 0.3$ and $Ta = 0.21 \pm 0.003$ to describe the role of spatiotemporal asymmetry on the thrust and lift production. Figures 4-6A and B show the thrust and lift forces produced during one beat cycle (FR in red, FF in blue, and CF in magenta). From these two plots we observe that for the FR case (rigid propulsor), the force peaks at the beginning and end of the power stroke; however, these peaks are mitigated by flexibility in the FF and CF cases. In living animals, the presence of flexibility helps enhance swimming stability and reduces the risk of appendage fracture and fatigue (Kim & Gharib, 2011). We further note that for the CF case, thrust is generally higher during the power stroke (relative to FR and FF) and less negative during the recovery stroke, due to the higher spatial asymmetry present in the CF paddle. We discuss this in detail below.

The force distributions in Figures 4-6C- E (FR, FF, and CF) are also useful to interpret thrust and lift production of each paddle. Each diagram shows three different time instants, representing the beginning of the power stroke, during the power stroke, and shortly after the completion of the power stroke (from left to right: t/T of 0.05, 0.3, and 0.42). We have placed a green arrow normal to the paddle and close to the peak force, to help visualize how the deformed shape of the paddle affects the distribution of the produced force between thrust (parallel to the substrate) and lift (normal to the substrate). At the beginning of the power stroke ($t/T = 0.05$), the backward bending of the FF paddle (Figure 4-6D) increases the vertical component of the force vectors relative to the FR case (higher lift). On the other hand, the initial curvature of the CF paddle increases the horizontal vector components (higher thrust). As the power stroke continues ($t/T = 0.3$), the FF paddle’s deformed shape maintains higher vertical components relative to the FR case, while the force vectors of the CF paddle have negative vertical components at this point. Thus, the

CF paddle produces the highest thrust force during the power stroke (Figure 4-6A), while the FF paddle has the highest lift force (Figure 4-6B). During the recovery stroke ($t/T = 0.42$), due to the slower speeds, the shape of the FR and FF paddles are similar, and therefore have similar force production (Figure 4-6A and B). However, the curved shape of the CF paddle strongly reduces the horizontal force components during the recovery stroke ($t/T = 0.42$); considerably reducing the negative thrust force (that is, drag) (Figure 4-6A).

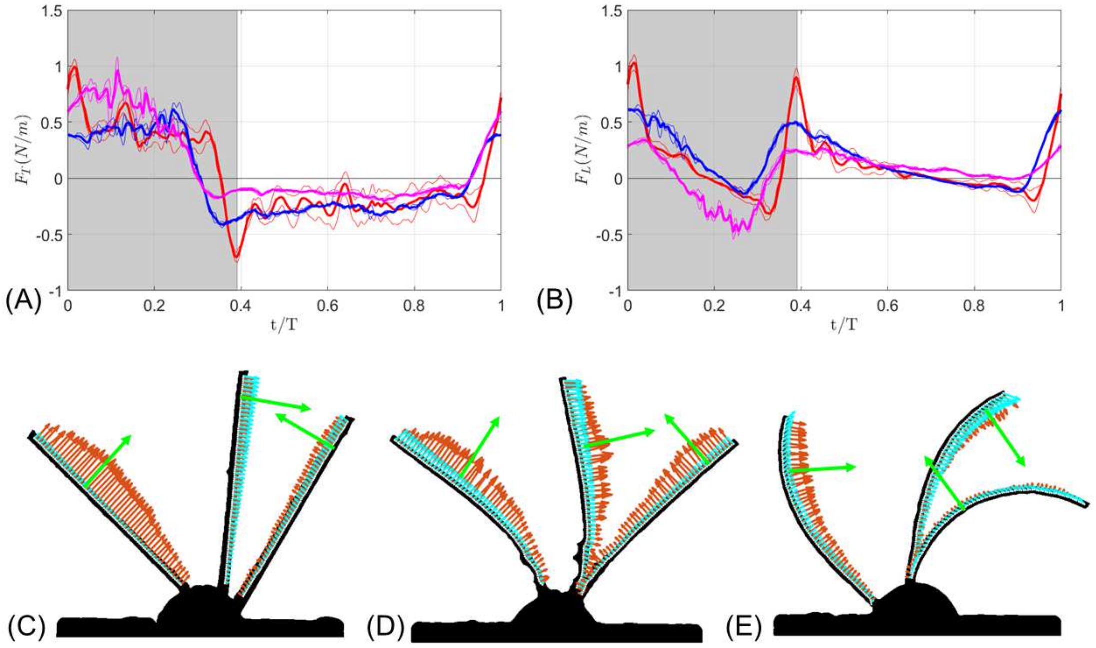

Figure **4-6**. Analysis of propulsor force production at $Re_\omega = 14.87 \pm 0.3$ and $Ta = 0.21 \pm 0.003$. (A) Thrust force production for the FR (red), FF (blue), and CF paddles (magenta). (B) Lift force production for the FR (red), FF (blue), and CF paddles (magenta). Thick lines are the 3-cycle-averaged time series, and thinner lines show the standard deviation of the measurements. The shaded area illustrates the time interval of the power stroke, and the white region is the recovery stroke. (C, D, and E) Force (orange) and velocity (cyan) distributions for three time instants at the beginning of the power stroke ($t/T = 0.05$), during the power stroke slightly after peak tip speed ($t/T = 0.3$), and the beginning of the recovery stroke ($t/T = 0.42$).

To compare thrust and lift force production for the three paddles at different Reynolds numbers, we compute the non-dimensional thrust and lift coefficients: $C_T = F_T/0.5\rho U_{tip}^2 l$ and $C_L = F_L/0.5\rho U_{tip}^2 l$. Here, since we are collecting 2D data, both F_T and F_L have dimensions of N/m (Figure 4-6A and B); we therefore we use the paddle height (l) to normalize the coefficient instead of the paddle area. We choose U_{tip} to be the tip speed of the rigid paddle at $Ta = 0$ (such that $U_{tip} = 2l\Phi f$).

Figure 4-7 shows the cycle-averaged thrust and lift coefficients for the FR (red), FF (blue), and CF (magenta) paddles as a function of Ta and Re_ω. In general, thrust increases as Ta increases; however, lift is generally constant across all observed Ta. For all studied cases, we observe that the CF paddle produces the highest thrust (Figure 4-7A) at the expense of the lift production (Figure 4-7B). The FF paddle produces the least thrust, but produces significant lift. The FR paddle is an intermediate case, producing both thrust and lift. These results are intuitive and agree with the previous discussion on the role of the paddle shape on force orientation (Figure 4-6). Figure 4-7 also shows how the force production is dependent on Reynolds number: in general, force coefficients decrease as the Reynolds number increases. This can be attributed both to our experimental strategy of increasing Re_ω by decreasing kinematic viscosity (and therefore lowering the density of the working fluid, see Table 4-1) and also to the passive response of the paddles to the hydrodynamic forces (Figure 4-4). Because the hydrodynamic forces and the paddle geometry/flexibility are coupled, performance cannot be evaluated solely from these cycle-averaged force coefficients. In the next section, we address this problem by introducing a new approach to calculate the efficiency of force generation (both thrust and lift).

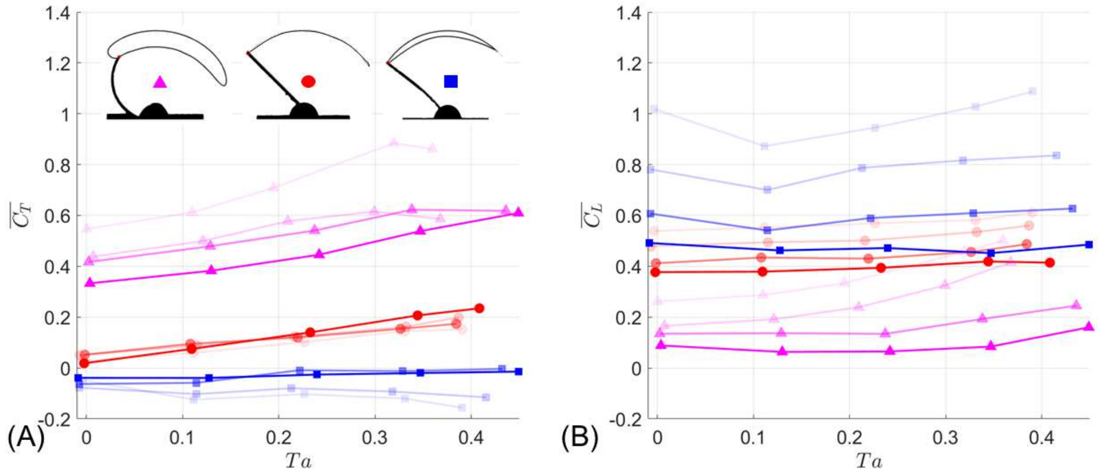

Figure **4-7.** Cycle-averaged force coefficients of the three rowing paddles at intermediate Reynolds numbers, where (A) shows thrust coefficient $\overline{C_T}$ and (B) shows lift coefficient $\overline{C_L}$. The FR paddle is shown in red, the FF paddle in blue, and the CF paddle in magenta. Experiments at different Reynolds numbers ($Re_\omega \equiv 2\pi f l^2/\nu$) are shown by the color transparency; from the most transparent line to the solid line, Re_ω increases as $7.43 \pm 0.24, 14.87 \pm 0.3$, 27.40 ± 0.53, and 62.93 ± 1.11.

4.1.4 Rowing paddle efficiency

The previous section discusses how motion asymmetry affects force production in rowing propulsors. Our goal in this next section is to develop a useful and mathematically appropriate expression for efficiency as a tool to quantify the performance of a rowing paddle (that is, dimensionless and scaling from 0 to 1). As mentioned previously, current metrics of propulsive efficiency commonly used for swimming organisms are based on the free motion of a body, requiring an overall swimming velocity (Gemmell et al., 2013; Lighthill, 1960; Murphy et al., 2011). This is a problem for evaluating the performance of a single rowing paddle, since the speed and force vary along the propulsor. For the case of (globally) fixed rowing appendages, it may be tempting to use the average or maximum far field velocity in place of the free-swimming velocity. However, the far field may not be a coherent velocity stream, nor is "far field" a well-defined distance. Additionally, this approach would not necessarily result in an efficiency expression that scales from 0 to 1, as desired. To calculate output power from a generated velocity field, we must make assumptions about the flow. For example, (Barlow & Sleigh, 1993) assumed that the flow above a ctene row behaves as a jet. The peak output power of a jet can be calculated as $0.5\rho u^3 A$, where A is the cross-sectional area of the jet. For this work, the (1D) area may be estimated as the distance from the top of the ctene to the point at which the flow velocity reaches only ~20% of the peak velocity. However, this approach is somewhat arbitrary, is not guaranteed to correctly measure the power output, and is not universally applicable to any type of oscillating appendage. We thus seek a new metric for propulsive efficiency, suitable for all globally-fixed rowing appendages (and extensible to appendages on a swimming body).

The definition of Froude efficiency (or propulsive efficiency) is the ratio between the power used to overcome drag to the power expended to produce the motion (Lighthill, 1960). When applied to a moving object it can be calculated as $\eta = F_T U/P$, where F_T is the thrust force, U is the swimming speed and P is the power input to the fluid. Here we will rely on this concept to develop an expression which accounts for the variable force and velocity distribution along the paddle, such that integrated thrust efficiency η_T is defined as

$$\eta_T = \frac{\sum_0^T \sum_1^n F_x V_x sgn(F_x)}{\sum_0^T \left| \left(\sum_1^n \vec{F} \times \vec{r} \right) \cdot \vec{\omega} \right|} \qquad (18)$$

where F_x and V_x are the horizontal components of force and velocity for each point on the paddle center line (summed over n spatial points, see Figure 4-5D, and T timepoints). The numerator of this expression therefore is the net power (force x speed) required to move each tracked point along the paddle through the fluid over the entire operation time (T). The sign function indicates that the power stroke produces thrust (positive), and the recovery stroke produces drag (negative) and therefore decreases the net integrated efficiency η_T. The denominator is the input power, which is calculated as the absolute value of the inner product of torque and shaft angular speed. The (time varying) net torque is calculated as the net force on each centerline point $(\vec{F})$ crossed with its position vector $(\vec{r})$ with respect to the shaft position. We calculate the (time varying) shaft angular speed using the first tracked point on the paddle and the shaft position. To define the lift efficiency (η_L), we consider the vertical components of force and velocity in the numerator.

Figures 4-8A and B show the integrated thrust and lift efficiencies for the FR (red), FF (blue), and CF (magenta) paddles as a function of Ta and Re_ω. As previously discussed, spatial asymmetry Sa is not prescribed, and is a function of Ta and Re_ω (Figure 4-4). We note that the CF paddle has the highest spatial asymmetry, and that Sa increases as Ta increases (with a mean of $Sa = 0.144 \pm 0.01$ across all tested conditions). The FR paddle is symmetric, with $Sa = 0$ across all Ta and Re_ω; the FF paddle has negative spatial asymmetry ($Sa = -0.03 \pm 0.01$ across all tested conditions).

For thrust production, we observe that the efficiency of all paddles rises as spatiotemporal asymmetry increases (at a given Re_ω). FF is the least efficient, slightly underperforming compared to the FR paddle. The decrease in performance can be attributed to the negative Sa values of the FF paddle. The CF paddle is the most efficient thrust producer: in fact, it is the only paddle which produces net positive thrust for temporally symmetric cycles ($Ta = 0$). The thrust efficiency of this paddle reaches a maximum value of $\eta_T \sim 0.6$, at the highest explored values of Ta. In Figure 4-4, we see that for fixed Ta, lower Re_ω always corresponds to higher Sa for the CF paddle. However, at high Ta, lower Re_ω counterintuitively produces lower η_T (upper right, Figure 4-8A). At lower values of Ta for the CF paddle, lower Re_ω are more efficient (middle left, Figure 4-8A). This may indicate that while higher Sa generally produces more net thrust, the cost of producing that thrust is a strong function of the viscous-inertial balance. In other words, producing thrust is easier at higher Re_{ω}, and when both Sa and Ta are high.

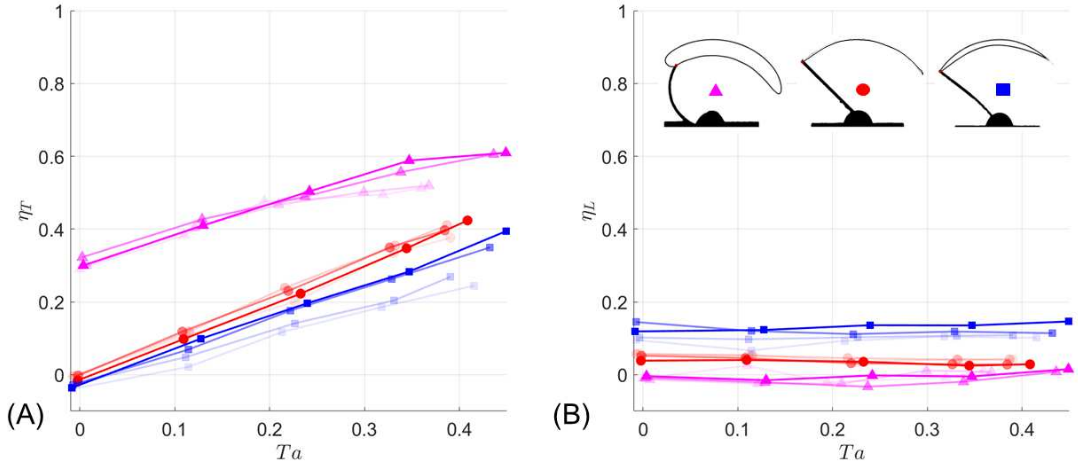

Figure **4-8**. Performance of three rowing paddles at intermediate Reynolds numbers. (A) Thrust production efficiency. (B) Lift production efficiency (equation 18). The FR paddle is shown in red, the FF paddle in blue, and the CF paddle in magenta. Experiments at different Reynolds numbers ($Re_{\omega} \equiv 2\pi f l^2/\nu$) are indicated by the line transparency; from the most transparent line to the solid line, Re_{ω} increases as $7.43 \pm 0.24, 14.87 \pm 0.3\,, 27.40 \pm 0.53,$ and $62.93 \pm 1.11.$

For the lift production efficiency η_L, we observe the opposite behavior with respect to spatial asymmetry (Figure 4-8B). The FF paddle, with negative spatial asymmetry, is the best at producing lift. The curved flexible paddle (CF), which carries the highest spatial asymmetry, is the worst. This is partially due to the propulsors' shape during the stroke cycle (Figure 4-6). As explained previously, the backward bending seen in the FF paddle (Figure 4-6D) increases the vertical force components during the power stroke. Conversely, the CF paddle's bending tilts the force vectors toward the horizontal, and actually produces negative values of lift force during the power stroke (Figure 4-6B). The FF paddle is the most efficient lift producer; this makes sense, since its bending kinematics (Figure 4-6D) are similar to the tail kinematics of a fish or other lift-based swimming strategy (Dewey et al., 2013). A fish's tail must maximize spanwise force production (corresponding to lift in these experiments). This strategy is typically used at much higher Reynolds numbers (Kurt et al., 2021). Fish swimming experiments have also shown that a flexible tail enhances swimming efficiency (Han et al., 2022), likely by smoothing force peaks and increasing the spanwise force components as described in section 4.1.2.

4.1.5 Discussion

We evaluated the propulsive performance of three paddles with different flexibilities and initial geometries in order to explore the role of spatiotemporal asymmetry for intermediate Re rowing. The comparison between the flat/rigid (FR), flat/flexible (FF), and curved/flexible (CF) paddles shows how flexibility smooths the aggressive force peaks observed on the rigid structure, as well as the role that the deformed paddle shape plays in directing the overall orientation of the hydrodynamic force. We showed how the CF paddle's passive deformation during the beat cycle resembles the spatially asymmetric motion of a ctene ($Sa > 0$). The geometry and flexibility of this paddle encodes the Sa into the structure, thus simplifying the required controls and hardware of a robotic rowing appendage (Ford & Santhanakrishnan, 2020; Santos et al., 2022). However, the passive response of the paddle makes its time-varying geometry a function of both Ta and Re_ω, thus complicating attempts to directly investigate the role of spatiotemporal asymmetries *vs.* Reynolds number.

We developed a new definition of propulsive efficiency that can be used to directly evaluate a rowing appendage's performance independently from the full-body swimming dynamics. Instead of swimming speed, the integrated efficiency considers the force and velocity distributions measured around the appendage. It also considers the directionality of appendage movement, so that only net thrust is considered (subtracting the power produced by drag from the motions that produce useful thrust power). The integrated efficiency may be calculated for robotic devices, numerical simulations, and animal experiments as long as the system's input power can be measured or estimated. Calculating the input power is typically feasible for robotic devices or numerical simulations, but estimating the power consumption of a live animal is not trivial (Svendsen et al., 2013). As it is defined here, the integrated efficiency (equation 18) is developed for 2D flows; however, it is easily extensible to 3D motion if the force and velocity distributions over the appendage surface are known. The expression is also extensible to non-globally fixed appendages, such as those moving with a body, as the appendage(s) may simply be considered in the reference frame of the body.

We showed that increasing both temporal and spatial asymmetries improve thrust efficiency, but that this relationship is coupled to Reynolds number. Spatial asymmetry (Sa) plays a significant role in thrust generation, and can substantially increase η_T. Even for a stroke cycle with $Ta = 0$, the CF paddle (which always has $Sa > 0$) has an efficiency of ~0.3 (Figure 4-8A). Spatially symmetric motions (FR) can only achieve this level of efficiency at very high values of temporal asymmetry ($Ta > 0.3$). To evaluate lift production, we found that the time-varying deformation of the paddle—not just net asymmetry—during the beat cycle plays an important role. The force distribution diagrams (Figures 4-6C-E) show how the bending kinematics of the FF paddle maximize lift force production, similar to the mechanism used by *e.g.* the tails of fish. In contrast, the CF paddle maximizes thrust, making the CF paddle the best of the three tested options for thrust production (Figure 4-8). However, none of the three tested paddles strictly reproduces the motion of the actual ctene. Real ctene bending kinematics (Figure 2-2) could be described as the power stroke of the FF paddle combined with the recovery stroke of the CF paddle, suggesting that ctene motion is a compromise between maximizing thrust while still generating some lift.

Although thrust production for forward swimming is a primary goal of rowing, producing a certain amount of lift in some cases is important. For ctenophores with spheroidal shapes (such as the small to medium lobates examined in Chapter 2 or cydippid ctenophores such as *Pleurobrachia* sp.), their ctenes protrude from strongly curved body surfaces. Depending on the co-located substrate curvature, the local ctene lift production can contribute to full-body forward motion (Lionetti et al., n.d.). For other metachronal rowers like krill or shrimp, which operate at higher *Re*, lift production is essential since they are negatively buoyant (Murphy et al., 2013). Future work may focus on creating propulsors whose shape and stiffness can be tuned to reproduce these kinematics, which balance lift and thrust for swimming organisms.

4.2 Particle Shadow Velocimetry: image pre-processing algorithm

Particle shadow velocimetry (PSV) is a flow measurement technique that differs in several key ways from the more commonly used Particle Image Velocimetry (PIV) (see Table 4-2). It uses back-lit (sometimes collimated) illumination to produce sharply defined shadows of tracer particles rather than the light-scattering approach produced by a laser sheet, as in PIV. Given that its illumination source is not usually laser-based, PSV is generally cheaper and safer to operate than PIV (Estevadeordal & Goss, 2005). It is also useful for systems in which optical access points are not ideal for PIV, or where backlighting can avoid undesirable shadows (e.g., in wake regions) (L. P. Goss et al., 2007). Typical 2C2D (*i.e.*, measuring two velocity components within a two-dimensional plane) PIV and PSV experimental setups are shown in Figure 4-9. One notable contrast is that in PIV, only the particles inside the laser sheet are imaged, even though other particles are in focus (but not illuminated); PSV instead relies on the optical depth of correlation (DoC) to isolate tracer motion to a plane. The DoC is the thickness of the imaged “plane” and is a property of the system optics as well as the tracer size (Figure 4-9); it is defined as the thickness over which imaged objects (e.g. tracers) can contribute to image cross-correlations. In general, it is desirable to reduce DoC as much as possible to confine velocity measurements to a single plane. Here is where one of the significant restrictions of PSV lies: DoC scales with field of view (FoV). Larger FoVs necessitate a larger imaged volume overall (and therefore a larger DoC), thus producing unacceptable noise levels from the out-of-focus tracers. Laser-based PIV does not have this problem because the imaged volume is defined by the thickness of the laser sheet, not the optics of the system.

Table **4-2.** Planar velocimetry using laser-based PIV vs PSV (2D2C).

Technique	**PIV**	**PSV**
Illumination	Laser light sheet	Backlighting from collimated LED (or similar)
Effect of out-of-focus tracers	Focal depth typically larger than light sheet; significantly out-of-focus tracers are not illuminated	Out-of-focus particles still visible, and can decrease to the signal-to-noise ratio
Field of view	Determined by optics, but not linked to the measurement thickness	Field of view varies with DoC, so large fields of view require mitigating noise from out-of-focus tracers

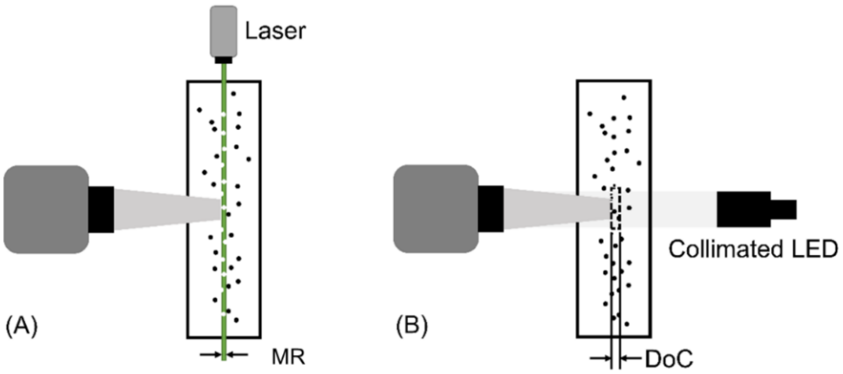

Figure **4-9.** (A) Schematic for a laser-based PIV system, where the thickness of the laser sheet defines the thickness of the measurement region (MR) and (B) a PSV system where the thickness of measurement region (dotted box) is defined by the optics of the system (DoC).

The DoC can be calculated for micro and macro-PSV (Olsen & Adrian, 2000; Truong et al., 2018) systems as

$$DoC = 2\sqrt{\frac{1-\sqrt{\varepsilon}}{\sqrt{\varepsilon}}\left[\left(\frac{\eta}{2NA}\right)^2 d_p^2 + 5.95\frac{(M+1)^2\lambda^2\left(\frac{\eta}{2NA}\right)^4}{M^2}\right]} \quad (17)$$

where ε is a threshold parameter (Olsen & Adrian, 2000), η is the refractive index of the material between the lens and the specimen, NA is the lens numerical aperture, d_p is the tracer diameter, M is the lens magnification, and λ is the wavelength of the illumination. The threshold ε is typically taken to be 0.01, which fits experimental data on the extinction of out-of-focus tracers (Santiago et al., 1998). The size of the FoV is inversely proportional to the magnification M. Following equation (17), a higher magnification produces a smaller DoC, which is desirable but not always attainable. If the DoC is on the order of the tracer diameter, the images can be inverted and processed as in traditional 2D2C PIV. However, as magnification decreases, DoC increases, and simple image inversion produces unacceptable noise levels from the out-of-focus tracers (Figure 4-10).

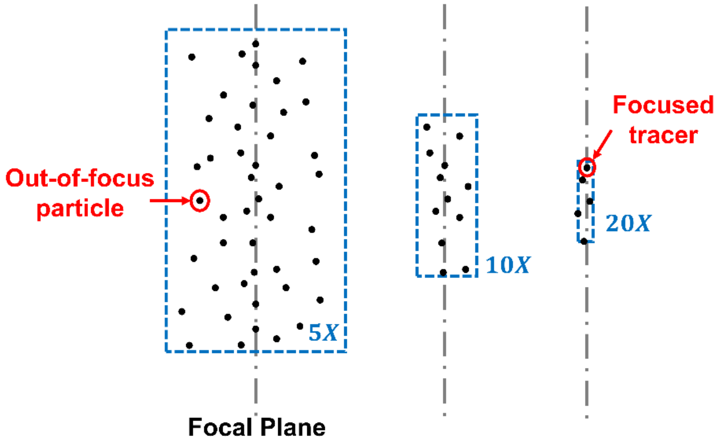

Figure **4-10.** To-scale schematic of the DoC (rectangle width) and FoV (rectangle height) for 3 µm particles at three different magnifications: 5X (NA=1.4), 10X (NA=0.21), and 20X (NA=0.5), as illuminated by a collimated white LED with $\lambda = 0.55\mu m$ and a refractive index of $\eta = 1$ (air).

Figure 4-11A show how a tracer looks in the camera when it is in front of, within, or behind the focal plane. When the tracer is aligned with the focal plane ($z \sim 0\ \mu m$) region where the "deep shadow region" dominates (Figure 4-11B), it is clearly delineable. When the tracer is behind the focal plane (on the shadowed side, $z > 0$) or in front of the focal plane (on the lit side, $z < 0$), it is haloed. Figure 4-11A effectively represents how 2.6 μm diameter out-of-focus tracers, captured at a magnification of 3.5, look across an imaged thickness of 400 μm (L. Goss & Estevadeordal, 2006). Although these are not the experimental conditions of our experiments, Figure 4-11A is representative of the in and out-of-focus particles behavior in all PSV configurations. If the flow of interest is three-dimensional enough that there is significant variability between the target plane *vs.* planes where we can still image these out-of-focus tracers, the signal-to-noise ratio becomes a problem. The haloing effect can extend for many particle diameters (Ovryn & Izen, 2000); it is therefore important to avoid imaging this region by keeping the DoC as small as possible.

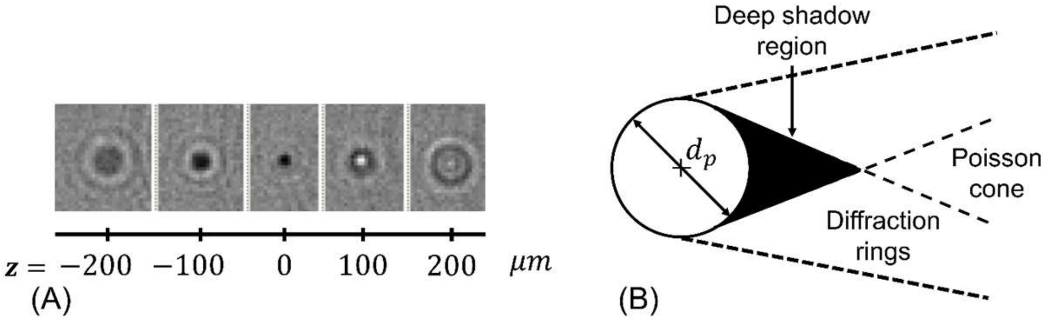

Figure **4-11.** Particles imaged by PSV. (A) Particles imaged at different distances from the focal plane for $d_p = 2.6\ \mu m$, and a DoC of $200\ \mu m$, reproduced from (L. Goss & Estevadeordal, 2006). (B) Schematic of the regions created by the backlighting of a hard sphere. The sphere is being illuminated from left to right. Adapted from (van de Hulst, 1957).

PSV is a logical choice for our experiments (outlined in Chapters 2 and 4) for two main reasons: first, given the geometry of the ctene row (Figure 2-1) and the robotic paddles (Figure 4-1C-E), side illumination is not an option as ctenes would cast shadows in the targeted imaging regions. Second, zooplankton are generally photosensitive; thus, high-energy lasers are not desirable. PSV has been used successfully for studying flows around plankton, but has generally been applied to small creatures (<1mm) (Gemmell et al., 2014) or restricted to highly zoomed-in regions (Colin et al., 2020). The ratio DoC/d_p for these experiments is less than 10 (*i.e.*, the DoC is less than ten tracer diameters thick). In our animal experiments, we are interested in simultaneously capturing several ctenes in one row, increasing the size requirements of the FoV and stretching to $DoC/d_p \sim 43$. This results in a strong signature of out-of-focus particles within the images. This problem is also common when using PSV to investigate bubble dynamics (Bröder & Sommerfeld, 2007; Hessenkemper & Ziegenhein, 2018). However, there is currently no detailed study on best practices for digitally removing the out-of-focus particles that decrease the quality of the vector fields.

4.2.1 Image pre-processing for focused tracer detection (FTD)

Here we outline our image pre-processing method that extends the PSV technique for scenarios with nontrivial DoC. Figure 4-12 shows the pre-processing method applied to a 200x200 pixel subwindow of a PSV image obtained from the experiments of section 2.1.1. When processing an entire image, intensity variation is significant between different regions of the image. To avoid thresholding problems, we apply the method by subwindows with an overlap. This way, all the operations are based on local rather than global parameters. The overlap also ensures that we will not lose tracers at the intersections between subwindows.

Each image describes one step in the detection algorithm, corresponding to a panel in Figure 4-12:

(0) The first image is the original (raw) image from the PSV setup. The in-focus and out-of-focus particles are distinguishable; there is one alien particle at the top left corner (too big to be a tracer; in this experiment, it is likely to be a piece of algae or mucus).

(1) We first invert the image.

(2) We then enhance the contrast using an exponential intensity transformation. In other words, we rescale the intensity distribution so it will follow an exponential distribution. This allows us to more easily separate the brighter regions (focused tracers) from the other areas of the image (out-of-focus tracers, background, and miscellaneous noise).

(3) Next, we apply a weak spatial Gaussian filter, which further reduces noise without eliminating the sharp edges of in-focus tracers.

(4) We isolate discrete regions using an edge detection operation. Given the nature of the image, a non-directionally based edge detection is needed; in this case, we use a Canny edge detection algorithm (Gonzalez et al., 2004) and fill closed contours with white to make the shapes uniform in intensity.

(5) We use two geometric threshold criteria to distinguish between artifacts, alien particles, and tracers: circularity ($C = 4A\pi/P^2$, where A is the area and P the perimeter) and the diameter d_p. If $C < 1$ or if d_p is outside the anticipated range (based on the known tracer dimensions), the spot is eliminated. **The remaining spots represent in-focus particles**. Finally, a Gaussian smoothing operation helps to avoid potential peak-locking effects (so that tracers themselves may still be centered at fractional pixel locations).

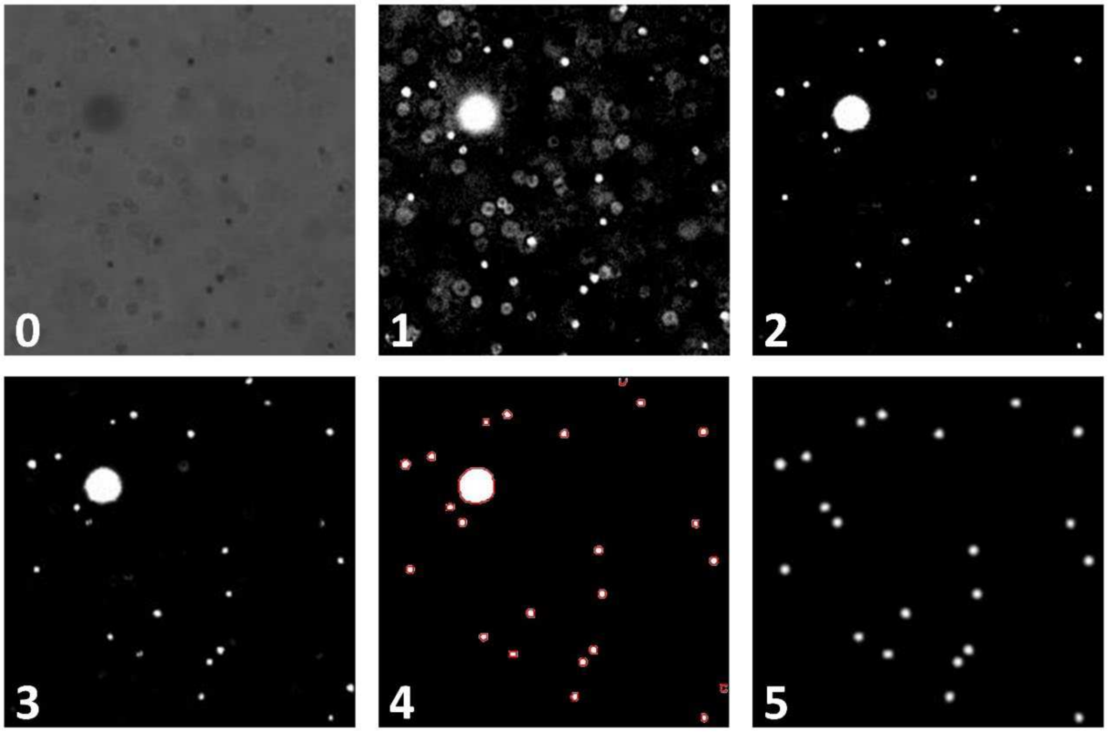

Figure **4-12.** Focused tracer detection algorithm for particle shadow velocimetry, from (0) the original image to (5) final processed image ready to be used in a PIV cross-correlation algorithm. Haloing effects like those shown in Figure 4-11 are clearly visible in the original image (0)

4.2.2 Results

Because ctenes have finite dimensions (*i.e.*, a rectangular plate with defined width, height, and thickness), they produce 3D flow structures. However, in our context of planar flow visualization, the finite width imposes two restrictions on what constitutes a useful 2D2C ctene velocimetry analysis: 1) the focal plane must be normal to the ctenes, and 2) it should bisect the ctene row as closely as possible. These two restrictions ensure that the flow within the measured plane is as 2D as possible, improving data quality and enabling analyses that would not otherwise be possible. The difficulty of achieving these conditions with live animals—combined with the large depth of correlation ($DoC/d_p = 43$) necessitated by the relatively large FoV required to image multiple ctenes simultaneously—yielded many out-of-focus particles, as shown in Figure 4-12 (0). Typical PIV image pre-processing techniques such as adaptive histogram equalization, highpass intensity filtering, and intensity capping (Thielicke & Stamhuis, 2014) were not helpful when dealing with noise levels produced by simply inverting the raw images, such as that seen in Figure 4-12 (1). When using these typical PIV preprocessing techniques, we obtained velocity fields similar to the one in Figure 4-13A. Here we observe numerous artefacts, such as false deceleration zones (circled), resulting from the influence of the out-of-focus tracers. These out-of-focus tracers, positioned on either side of the focal plane, are likely to be moving at low velocity or with a velocity primarily directed normal to the plane of focus; their contribution to the image correlation artificially decreases the calculated in-plane velocities. In contrast, Figure 4-13B, generated from the same raw images but using the prefiltering described in the previous section, shows more reasonable velocity measurements and demonstrates the algorithm's capacity to eradicate out-of-focus noise.

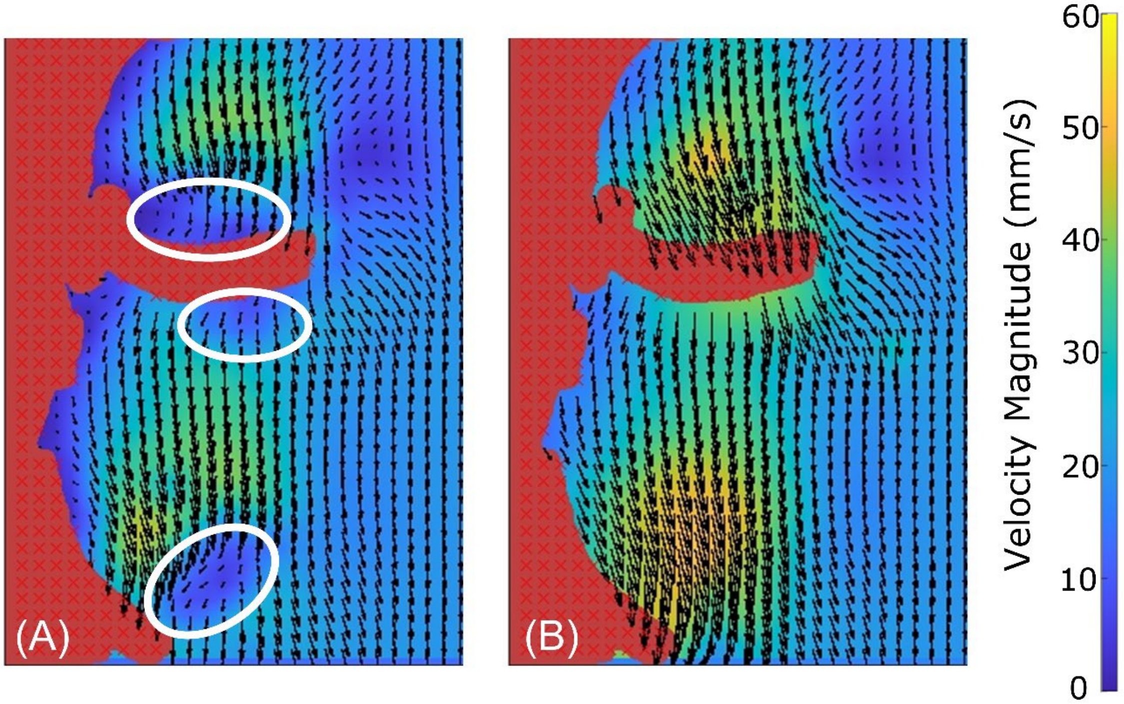

Figure **4-13.** Velocity field of the metachronal rowing of an adult ctenophore, calculated using (A) PIV common pre-processing techniques, and (B) our focused tracer detection algorithm. False deceleration zones are circled in white.

4.2.3 Summary and planned future work

We have developed a focused tracer detection algorithm for PSV systems with nontrivial DoC, which is qualitatively shown to increase the signal-to-noise ratio (Figure 4-13). This pre-processing algorithm is used for the velocimetry described in Sections 2.1 and 4.1. Given the lack of information available on reducing the effective DoC via image prefiltering in PSV systems, we suggest a comprehensive study to systematically characterize the performance of our algorithm. By comparing the velocity vectors obtained under different DoC/d_p ratios when imaging a canonical, well-described flow (*e.g.*, Poiseuille flow or a laminar jet), we can quantitatively calculate how much our prefiltering algorithm improves the probability of detecting valid velocity vectors (Shavit et al., 2006).

Chapter 5

Conclusions

The study of locomotion at intermediate Reynolds on the order of 1-1000 has tremendous potential for bioinspired design, particularly for scalability across the viscous-inertial flow regime. Animals living in this flow regime deal nontrivially with viscous and inertial effects. Therefore, their locomotive strategies must be adaptable for success in either viscous-dominated ($Re < 1$) or inertia-dominated environments ($Re > 1$). The vast number of animals at the millimeter to centimeter scale represent a potential source of inspiration for engineers to develop both micro- and macro-robotic platforms. However, understanding the operational limits—and therefore the contextual applicability—of different propulsors is crucial. We stress that strict biomimicry should not be the goal in designing vehicles and devices based on animal models: for all animals, their morphology is a compromise that allows them to perform all vital functions, not just locomotion (and some aspects of morphology may be vestigial and irrelevant to performance in any sense).

In the preceding chapters, we have studied the swimming dynamics of ctenophores *via* behavioral observation, mathematical modeling, and physical (robotic) modeling. Ctenophores base their locomotion on the metachronal (sequential) actuation of multiple appendages; this rowing technique exists across a wide range of sizes, from unicellular organisms (micrometers, $Re \ll 1$) to marine crustaceans (tens of centimeters, $Re > 1000$). Ctenophores with appendage-based Reynolds numbers on the order of 10-100 are a bridge to understanding how this technique scales from low to intermediate Reynolds numbers. Using several methods, we showed the importance of appendage motion asymmetries (spatial and temporal) on force production. At intermediate Reynolds numbers, both spatial and temporal asymmetries increase the performance of the propulsors. However, spatial asymmetries are dominant—that is, they are observed to be stronger in behaving animals, and calculated to be more effective in models—in more viscous environments ($Re \sim 1$). Temporal asymmetry gains importance as the inertial effects grow; we observe increasing temporal asymmetry with Reynolds numbers in behaving animals, and our modeling shows that increasing temporal asymmetry is more effective at higher Reynolds numbers.

Through our robotic appendage experiments, we developed a new expression for rowing efficiency which is tailored for oscillating appendages (flexible or rigid). The integrated efficiency allows more accurate performance analysis of robotic devices and can be used to improve our understanding of animal motion. By analyzing the ctene-inspired robotic appendage, we showed how the rowing propulsor's shape throughout the beat cycle could reorient the direction of the produced force—an important factor to consider in designing a bio-inspired Unmanned Underwater Vehicle (UUV). Finally, with a combination of animal observations and mathematical modeling, we studied how the spheroidal body shape of ctenophores—combined with the large number of appendages circumscribing their body and the independent frequency control between paired appendages—enables near-omnidirectional swimming.

Our results show how geometric and kinematic parameters, together with flexibility, affect ctenophores' swimming dynamics. As a representative intermediate Reynolds number metachronal rower, our findings can be extrapolated to a large number of organisms in a wide variety of ecological niches. Additionally, our new understanding the role of these parameters will help us tailor the design of bio-inspired devices depending on their specific task and context. Metachronal coordination is well known for being an efficient locomotor strategy (Guo & Kanso, 2016); therefore, the development of an intermediate to high Reynolds number metachronal-swimming UUV may meet the needs of certain ocean exploration tasks (Xu & Dabiri, 2022). At the other end of the size spectrum, the near-omnidirectional swimming of ctenophores is a highly desirable skill for low-Reynolds number robots needed for therapeutic or diagnostic operations inside the human body (Sitti, 2018). By successfully investigating the hydrodynamic scaling of metachronal rowing and its dependence on kinematic and geometric variation of the propulsors, the research presented in this dissertation provides a firm foundation for the development of new flexible bio-inspired robotic vehicles and fluidic devices.

Appendix A

Reduced-order modeling

A.1 Ctene kinematics

We model each ctene as a flat plate which oscillates unidirectionally with a time-varying height, such that the tip of the plate traces out an elliptical trajectory (section 2.1, Figure 14). To define the beating kinematics, we first derive expressions to construct the elliptical trajectory for the plate tip—namely, finding the semimajor and semiminor axes (a and b) as function of the spatial asymmetry (Sa) and the ctene length (l). In equation (2), A_o is defined as the largest possible area of an ellipse contained within the reachable area of the ctene, which is 0.77 times the reachable area of a rigid, non-bending ctene (the half circle with area $\pi l^2/2$). Substituting into equation (2) we get $Sa = A_e/0.385\pi l^2$, where A_e is the area of the elliptical tip trajectory ($A_e = \pi ab$). From this we can calculate the semiminor axis b as

$$b = 0.385\frac{l^2}{a}Sa \qquad (A.1)$$

To calculate the semimajor axis a, we must include the stroke amplitude (Φ). Figure 6B shows that the starting and ending points of the power stroke are defined by Φ and the perimeter of the half circle with radius l. Focusing on a triangle formed by the origin, the center of the ellipse, and a major axis vertex we can calculate the semimajor axis length and the y-coordinate of the center of the ellipse as:

$$a = l\sin(\Phi/2) \qquad (A.2)$$

$$y_c = l\cos(\Phi/2) \qquad (A.3)$$

The position of the plate tip is given by the parametric equations of the ellipse: $x_A = a\cos\theta$ and $y_A = y_c + b\sin\theta$. The tip velocity is given by the corresponding derivatives $\dot{x}_A = -a\dot{\theta}\sin\theta$ and $\dot{y}_A = b\dot{\theta}\cos\theta$. To evaluate the kinematics, we must define expressions for the angular velocity ($\dot{\theta}$) and the angular position (θ) as functions of time. We will assume a constant angular velocity for the power and recovery strokes ($\dot{\theta}_p$ and $\dot{\theta}_r$):

$$\dot{\theta}_p = \frac{\pi}{t_p} \qquad (A.3a)$$

$$\dot{\theta}_r = \frac{\pi}{t_r} \qquad (A.3b)$$

The power and recovery stroke time are easily calculated from the temporal asymmetry and cycle period: $t_r = T(Ta + 1)/2$ and $t_p = T - t_r$. Lastly, $\theta(t)$ can be continuously evaluated for as many cycles as needed following this piecewise-defined function:

$$\theta(t) = \begin{cases} \dot{\theta}_p[t - (mt_r)] + m\pi & for \quad mT \le t \le mT + t_p \\ (m+1)\pi + \dot{\theta}_r[t - (m+1)t_p] & for \quad mT + t_p < t \le (m+1)T \end{cases} \qquad (A.4)$$

where m is the cycle number ($m = 0,1,2,3, \ldots$). Equations A.1 to A.4, define the kinematics of the model.

A.2 Swimming efficiency (1D model)

The swimming efficiency ($\eta = P_o/P_i$) is defined as the ratio between the output power (P_o) to the input power (P_i). These are computed as

$$P_i = \frac{N}{t}\sum_{k=1}^{n}\int_0^t F_p\,[\dot{x}_{\boldsymbol{B}} + \dot{x}_A(t + (k-1)\tau)]dt \qquad (A.5a)$$

$$P_o = \frac{1}{t}\left[\int_0^t F_d\dot{x}_B dt + \int_0^t (m + \alpha\rho V)\ddot{x}_B\dot{x}_B dt\right] \qquad (A.5b)$$

where the summation in A.5a calculates the work done by the n ctenes in a row, multiplied by the number of ctene rows ($N = 8$) and divided by the swimming time (t) to obtain power. Equation (A.5b) accounts for the work needed to overcome drag (first integral) and the work expended to overcome the acceleration reaction force and produce the body's own acceleration (second integral) (Daniel, 1983).

A.3 Three-dimensional swimming model

This supplementary material outlines the dynamics and solution procedure for the three-dimensional reduced-order ctenophore swimming model. Figure A-1 shows the coordinate systems used to model the spheroidal body motion. We need two coordinate systems, an inertial system $\vec{x} = x_1\widehat{e_1} + x_2\widehat{e_2} + x_3\widehat{e_3}$, and a body-based coordinate system $\vec{x}' = x_1'\widehat{e_1'} + x_2'\widehat{e_2'} + x_3'\widehat{e_3'}$. As is typical in vehicle dynamics (Schaub & Junkins, 2018), we use the successive rotations (Z-Y-X or 3-2-1) yaw, pitch, and roll (ψ, θ, ϕ).

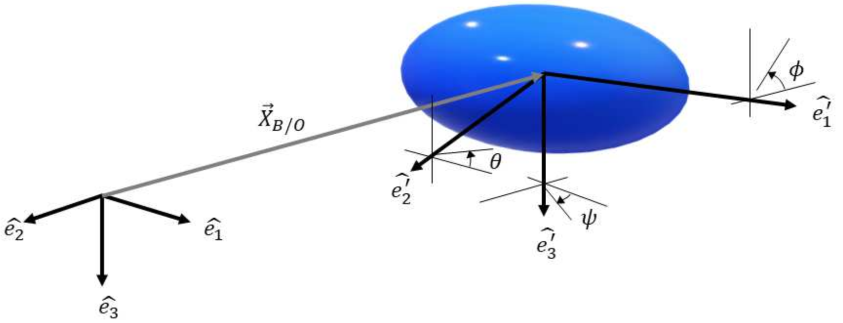

Figure **A-1.** Schematic of a ctenophore's simplified geometry moving in a 3D space**.** The unit vectors $\widehat{e_1}$, $\widehat{e_2}$, and $\widehat{e_3}$ define the global (fixed) coordinate system while $\widehat{e_1'}$, $\widehat{e_2'}$, and $\widehat{e_3'}$correspond to the moving coordinate system attached to the spheroidal body.

The transformation between the inertial and body frames is given by $\vec{x}' = [C]\vec{x}$, where the transformation matrix is given by

$$[C] = \begin{bmatrix} \cos(\theta)\cos(\psi) & \cos(\theta)\sin(\psi) & -\sin(\theta) \\ \sin(\phi)\sin(\theta)\cos(\psi) - \cos(\phi)\sin(\psi) & \sin(\phi)\sin(\theta)\sin(\psi) + \cos(\phi)\cos(\psi) & \sin(\phi)\cos(\theta) \\ \cos(\phi)\sin(\theta)\cos(\psi) + \sin(\phi)\sin(\psi) & \cos(\phi)\sin(\theta)\sin(\psi) - \sin(\phi)\cos(\psi) & \cos(\phi)\cos(\theta) \end{bmatrix} \qquad \text{(A.6)}$$

To avoid mathematical singularities when solving 3D motion using Euler angles (ψ, θ, ϕ), we performed all calculations using Euler parameters instead:

$$[C] = \begin{bmatrix} \beta_0^2 + \beta_1^2 - \beta_2^2 - \beta_3^2 & 2(\beta_1\beta_2 + \beta_0\beta_3) & 2(\beta_1\beta_3 - \beta_0\beta_2) \\ 2(\beta_1\beta_2 - \beta_0\beta_3) & \beta_0^2 - \beta_1^2 + \beta_2^2 - \beta_3^2 & 2(\beta_2\beta_3 + \beta_0\beta_1) \\ 2(\beta_1\beta_3 + \beta_0\beta_2) & 2(\beta_2\beta_3 - \beta_0\beta_1) & \beta_0^2 - \beta_1^2 - \beta_2^2 + \beta_3^2 \end{bmatrix} \qquad \text{(A.7)}$$

The most general rigid body rotation has only three degrees of freedom; thus, the Euler parameters are subject to the constraint $\beta_0^2 + \beta_1^2 + \beta_2^2 + \beta_3^2 = 1$. To calculate the Euler parameters $(\vec{\beta})$, we use the Stanley method (Schaub & Junkins, 2018). The last step for a formulation based on Euler parameters is to find the relationship between the time rates of change of $\vec{\beta}$ and the body angular velocities $(\vec{\omega}')$. This relationship is known as the Euler parameter kinematic differential equation:

$$\begin{bmatrix} \dot{\beta}_0 \\ \dot{\beta}_1 \\ \dot{\beta}_2 \\ \dot{\beta}_3 \end{bmatrix} = \begin{bmatrix} -\beta_1 & -\beta_2 & -\beta_3 \\ \beta_0 & -\beta_3 & \beta_2 \\ \beta_3 & \beta_0 & -\beta_1 \\ -\beta_2 & \beta_1 & \beta_0 \end{bmatrix} \begin{bmatrix} \omega_{x'} \\ \omega_{y'} \\ \omega_{z'} \end{bmatrix} \qquad (A.8)$$

Hence, under an Euler parameter formulation, we have three (vector) governing equations: the first and second Euler's laws (equations 8 and 9 in the manuscript) and the Euler parameter kinematic differential equation (A.8).

A.3.1 Propulsion force

As described in the main manuscript, each ctene is modeled as an oscillating flat plate, whose kinematics $(x_A(t), y_A(t))$ depend on the beating parameters and placement on the animal body (section3.2, Figure 3-8). The 3D model uses the same flat plate kinematics as the 1D version (A1), but here we will “place” them on the 3D body. To "place" each oscillating flat plate, we need three position angles: the ctene row angle $_{i}\varepsilon$, the ctene position angle on the ctene row $_{k}\zeta$, and the angle of the first ctene on the row κ (Figures A-2C and D). These angles are based on measurements from experimentally observed animals: $_{i}\varepsilon$ and κ are measured directly, while $_{k}\zeta$ is determined based on the average spacing ratio $s = l/\delta$, where δ is the arc length of the body surface between ctenes (the perimeter of the modeled body is given by $a\int_0^{\zeta}\sqrt{1-m\,sin^2(\zeta)d\zeta}$, where $m = 1-(b/a)^2$). Finally, the plates oscillate tangentially to the body surface (Fig A-2E); the tangential angle is calculated from the parametric equations of the ellipse that defines the spheroidal body as $_{k}\lambda = tan^{-1}\left[\frac{-\mathrm{a}\cos\left(_{k}\zeta\right)}{b\,\sin\left(_{k}\zeta\right)}\right]$.

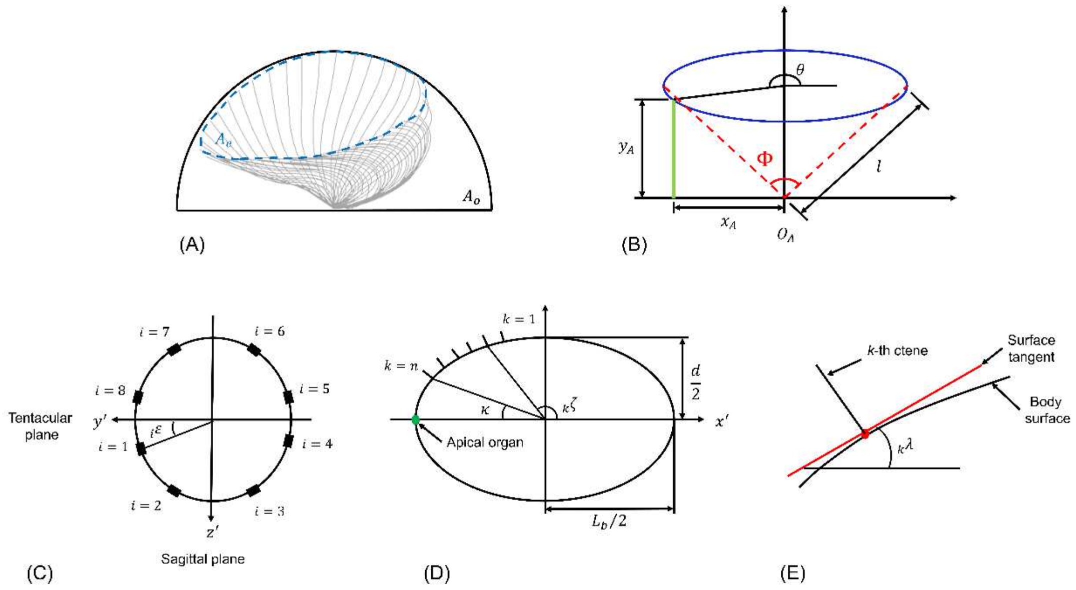

Figure **A-2.** (A) Graphical description of the spatial asymmetry overlaid on the ctene lateral profile time series. (B) Simplified elliptical trajectory (blue line, (x_A, y_A)) and the oscillating flat plate (green line). Dotted red lines denote stroke amplitude (Φ), and l is the ctene length. (C) Top view of a modeled ctenophore, showing the tentacular and sagittal planes. Black boxes indicate the i^{th}

ctene row and ${}_{i}\varepsilon$ the corresponding ctene row position angle. (D) Side view showing a plane bisecting a ctene row. Black lines protruding from the body represent the k^{th} ctene on the row. Ctene rows start at a fixed angle κ with respect to the apical organ, and ${}_{k}\zeta$ is the ctene positioning angle. (E) Close up of a ctene position (red dot), showing the tangential angle to the body surface ${}_{k}\lambda$.

A.3.2 Force and drag coefficients

To model the drag of the oscillating plate while considering the correct Reynolds number range for ctene beating $(1 < Re < 200)$, we use the empirical expression obtained by (Shih & Buchanan, 1971), appropriate for Reynolds numbers between 1 and 1057.

$$C_A = 15Pe^{-0.5}\exp\left(\frac{1.88}{Re^{0.547}}\right) \qquad (A.9)$$

where Pe is the period parameter and is defined as $Pe = \left(\left|{}^{max}_{ik}\vec{u} - \dot{\vec{X}}_{B/0}\right| T\right)/w$, and the Reynolds number is defined as $Re = \left(\left|{}^{max}_{ik}\vec{u} - \dot{\vec{X}}_{B/0}\right| w\right)/\upsilon$.

From (Loth, 2008), we obtain an expression for the drag coefficient of a prolate spheroid:

$$C_B = C_{shape}\left[\frac{24}{{Re_B}^*}\left(1 + 0.15{Re_B}^{*0.687}\right) + \frac{0.42}{1 + \dfrac{42{,}500}{{Re_B}^{*1.16}}}\right] \qquad (A.10)$$

$${Re_B}^* = \frac{C_{shape}}{f_{shape}}\left(\frac{\left|\dot{\vec{X}}_B\right| d_e}{\nu}\right)$$

$$C_{shape} = 1 + 0.7\sqrt{\left({A_{surf}}^* - 1\right)} + 2.4\left({A_{surf}}^* - 1\right)$$

$${A_{surf}}^* = \frac{1}{2{\alpha_s}^{\frac{2}{3}}}\left[1 + \frac{\alpha_s}{\sqrt{1 - {\alpha_s}^{-2}}}sin^{-1}\left(\sqrt{1 - {\alpha_s}^{-2}}\right)\right]$$

where d_e is the spherical equivalent diameter and f_{shape} depends on flow direction

$$f_{shape}^{\parallel} = \frac{(4/3)\alpha_s^{-\frac{1}{3}}(1-\alpha_s^2)}{\alpha_s - \frac{(2\alpha_s^2-1)\ln\left(\alpha_s+\sqrt{\alpha_s^2-1}\right)}{\sqrt{\alpha_s^2-1}}}$$

$$f_{shape}^{\perp} = \frac{(8/3)\alpha_s^{-\frac{1}{3}}(\alpha_s^2-1)}{\alpha_s + \frac{(2\alpha_s^2-3)\ln\left(\alpha_s+\sqrt{\alpha_s^2-1}\right)}{\sqrt{\alpha_s^2-1}}}$$

where α_s is the aspect ratio of the body, $\alpha_s \equiv L_b/d$.

From (Horace, 1993), we obtain the added mass coefficients for a spheroidal body for the axial and lateral movements (k_1, k_2):

$$k_1 = \frac{1-e^2}{e^3}\left[\ln\left(\frac{1+e}{1-e}\right) - 2e\right] \qquad (A.11a)$$

$$k_2 = \frac{1-e^2}{e^3}\left[\frac{e}{1-e^2} - \frac{1}{2}\ln\left(\frac{1+e}{1-e}\right)\right] \qquad (A.11b)$$

where e is the eccentricity $\left(e = \sqrt{b^2 - a^2/b^2}\right)$. This approach is fully valid only for linearly superposable flows (i.e. potential flow (high Re) or Stokes flow (low Re)) but is a good engineering approximation for intermediate Reynolds numbers (Brennen, 1982).

To model the opposing torques, we used the numerical expressions obtained by (Zastawny et al., 2012), which is appropriate for rotating Reynolds numbers $\left(Re_R = \frac{d_e^2|\vec{\omega}'|}{\nu}\right)$, between $10^{-1} - 10^3$.

$$C_R = r_1(Re_R)^{r_2} + \frac{r_3}{(Re_R)^{r_4}} \qquad (S.8)$$

where the coefficients r_i depend on the rotating direction (rolling or pitch/yaw axes); see Table A-1.

Table **A-1.** Values for the torque coefficient expression along the roll and pitch/yaw directions

Turning axis	r_1	r_2	r_3	r_4
roll	0.573	−0.154	116.61	1
pitch/yaw	1.244	0.239	378.12	0.789

A.3.3 Solution procedure for the 3D swimming model

We solved the reduced-order model using a fourth-order Runge-Kutta scheme for implicit equations, using the MATLAB function ode15i. The solution algorithm consists of the following steps:

1. Input the initial particle position, orientation, and speeds (translational and angular).
2. Calculate the initial transformation matrix using equation (A.6).
3. Calculate the corresponding initial values of the Euler parameters using the Stanley method and evaluate the transformation matrix in its parametrized form using equation (A.7).
4. Evaluate the propulsion and opposing forces and torques (equations 12, 13, 14, 15, and 16, section 3.2) at the current time instant for all the (predetermined) morphometric and metachronal parameters.
5. Solve the equations of motion as given by equations 8, 9, and (A.8).
6. Return to step 4 and continue until the halting condition is met. Validations and Motor Volume calculations are halted after a certain solution time; while the MAP results are halted when a steady state radius of curvature is achieved.

   The numerical integration of the equations of motion iterated until it reached tolerances of 10^{-5}.

Appendix B

Pressure-based force calculations

B.1 Force calculations at different sampling distances

One of the primary features of QUEEN 2.0 is the ability to define the presence of a solid object in a flow. Not specifying the solid region for the pressure calculation via solving the Navier-Stokes equations results in noise and affects the algorithm accuracy (Dabiri et al., 2014). For this work's velocity fields, the PSV Cartesian grid has a resolution of 64x64 px, restricted by our tracer particle density and camera resolution. Figure B-1 shows the problem of defining the solid region of our paddles by using the cartesian grid points. To define the solid region in the pressure-calculation algorithm, several points need to define the thickness of the paddle. Therefore, we must dilate the solid to a size that assures solid identification.

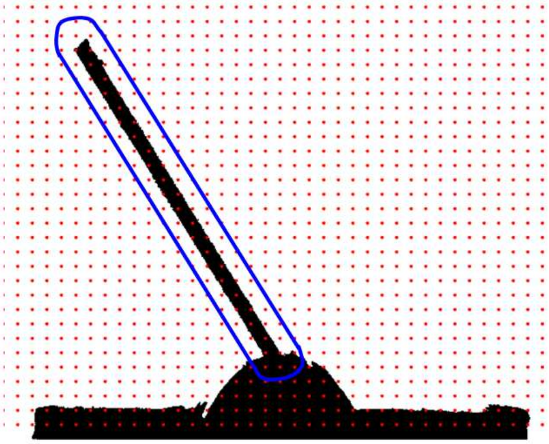

Figure **B-1.** PSV cartesian grid placed on top of the rigid paddle shape. Blue lines show how the paddle needs to be dilatated to be recognized as a solid region by the pressure-calculation algorithm of QUEEN2.

Given that pressure values are non-existing in the solid region, our sampling points (section 4.1, Figure 4-5) need to be placed where the pressure is defined—further increasing the distance from the real solid. Here we present a sensitivity analysis of the force calculation as a function of the pressure sampling distance. To do this, we calculated the thrust and lift forces for the rigid paddle without defining a solid region, sampling from a point right at the true fluid-solid interface to one five times the paddle thickness away $(d_o = 0.8, 1, 2, 3, 4, 5\ mm)$. Figure B-2A shows the pressure field calculated without a solid region with the paddle centerline (purple) and several sampling distances, and Figure 4B-2B the case considering the solid region and the distance chosen for this work $(d_o = 3.5\ mm)$.

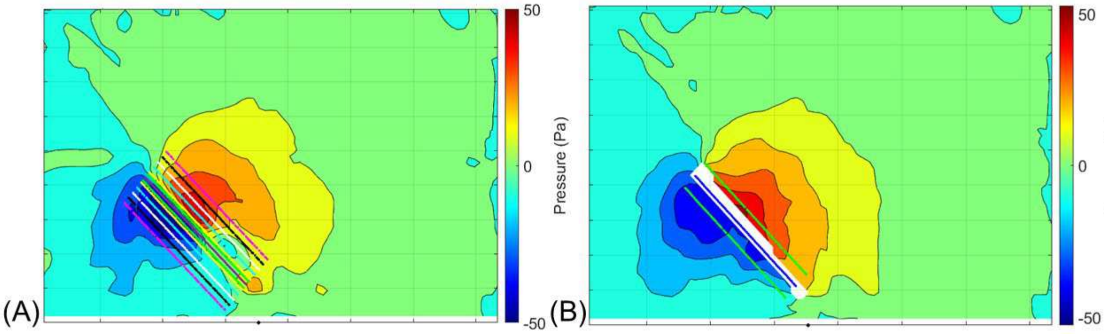

Figure **B-2**. Pressure fields computed from PSV velocity data. (A) Without considering a solid region. The centerline of the paddle is colored purple, and the rest of the lines indicate pressure sampling points with offset distances of 0.8, 1, 2, 3, 4, and 5 mm. (B) Considering a solid region. The center line of the paddle is colored blue, and the green dots show the selected offset distance of 3.5 mm.

Figures B-3A and B show that both the thrust and lift forces have limited change for all the sampling distances $(0.8 - 5\ mm)$. Therefore, we choose an offset distance of $3.5\ mm$; this clearance is enough to sample pressure values along our three different paddles. Looking at Figure B-2B, it is clear how the presence of the solid region improves the pressure estimation. The force calculation considering the presence of the solid (Figures B-3C and D), can capture the initial peak in force produced by the rigidity of the paddle. The peak force is an expected result not well captured by the calculation neglecting the solid region. The results of this sensitivity analysis agree with those conducted at higher Reynolds (Lucas et al., 2017).

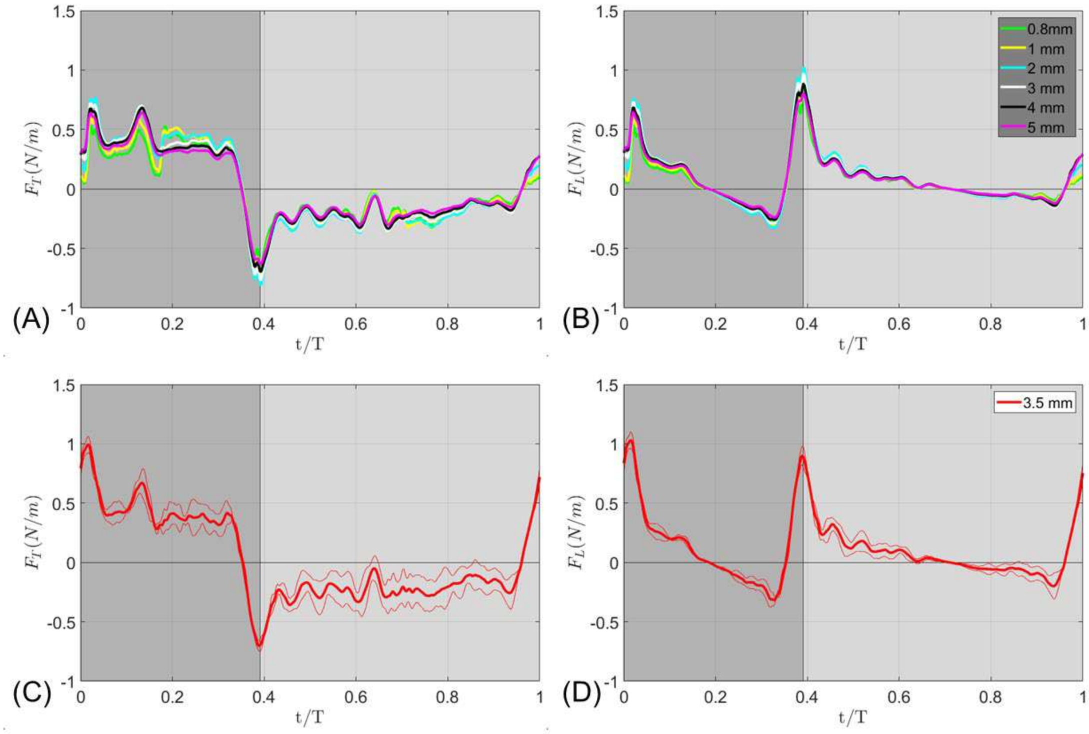

Figure **B-3.** Force sensitivity analysis for the pressure offset sampling distance (A and B). Different colors indicate different offset distances from the centerline $\left(d_{offset} = 0.8, 1, 2, 3, 4, 5\ mm\right)$. (A) Thrust force. (B) Lift force. (C and D) shows the calculated thrust and lift force for the selected offset distance 3.5 mm, considering the presence of a solid region in the pressure field. Thick lines are the 3-cycle-averaged time series, and thinner lines show the standard deviation of the measurements. The darker shaded area illustrates the time interval of the power stroke, and the lighter shaded region is the recovery stroke.

References

Afzelius, B. A. (1961). The fine structure of cilia from ctenophore swimming-plates. *The Journal of Biophysical and Biochemical Cytology*, *9*(2), 383–394. https://doi.org/10.1083/jcb.9.2.383

Alben, S., Spears, K., Garth, S., Murphy, D., & Yen, J. (2010). Coordination of multiple appendages in drag-based swimming. *Journal of The Royal Society Interface*, *7*(52), 1545–1557. https://doi.org/10.1098/rsif.2010.0171

Asadnia, M., Kottapalli, A. G. P., Karavitaki, K. D., Warkiani, M. E., Miao, J., Corey, D. P., & Triantafyllou, M. (2016). From Biological Cilia to Artificial Flow Sensors: Biomimetic Soft Polymer Nanosensors with High Sensing Performance. *Scientific Reports*, *6*(1), 1–13. https://doi.org/10.1038/srep32955

Barlow, D., & Sleigh, M. A. (1993). WATER PROPULSION SPEEDS AND POWER OUTPUT BY COMB PLATES OF THE CTENOPHORE PLEUROBRACHIA PILEUS UNDER DIFFERENT CONDITIONS. *Journal of Experimental Biology*, *183*(1).

Barlow, D., Sleigh, M. A., & White, R. J. (1993). WATER FLOWS AROUND THE COMB PLATES OF THE CTENOPHORE PLEUROBRACHIA PLOTTED BY COMPUTER: A MODEL SYSTEM FOR STUDYING PROPULSION BY ANTIPLECTIC METACHRONISM. *Journal of Experimental Biology*, *177*(1).

Blake, J. R., & Sleigh, M. A. (1974). Mechanics of ciliary locomotion. *Biological Reviews*, *49*(1), 85–125. https://doi.org/10.1111/j.1469-185X.1974.tb01299.x

Brennen, C. E. (1982). *A Review of Added Mass and Fluid Inertial Forces*. https://resolver.caltech.edu/CaltechAUTHORS:BREncel82

Brennen, C. E., & Winet, H. (1977). Fluid Mechanics of Propulsion by Cilia and Flagella. *Annual Review of Fluid Mechanics*, *9*(1), 339–398. https://doi.org/10.1146/annurev.fl.09.010177.002011

Brindise, M. C., Busse, M. M., & Vlachos, P. P. (2018). Density- and viscosity-matched Newtonian and non-Newtonian blood-analog solutions with PDMS refractive index. *Experiments in Fluids*, *59*(11), 173. https://doi.org/10.1007/s00348-018-2629-6

Bröder, D., & Sommerfeld, M. (2007). Planar shadow image velocimetry for the analysis of the hydrodynamics in bubbly flows. *Measurement Science and Technology*, *18*(8), 2513–2528. https://doi.org/10.1088/0957-0233/18/8/028

Byron, M., Santhanakrishnan, A., & Murphy, D. (2021). Metachronal Coordination of Multiple Appendages for Swimming and Pumping. *Integrative and Comparative Biology*, *61*(5), 1561–1566. https://doi.org/10.1093/ICB/ICAB181

Caldwell, R. L., Vilhena, D., & Campos, E. O. (2012). Pleopod Rowing Is Used to Achieve High Forward Swimming Speeds During the Escape Response of Odontodactylus havanensis (Stomatopoda). *Journal of Crustacean Biology*, *32*(2), 171–179. https://doi.org/10.1163/193724011X615596

Colin, S. P., Costello, J. H., Hansson, L. J., Titelman, J., & Dabiri, J. O. (2010). Stealth predation and the predatory success of the invasive ctenophore Mnemiopsis leidyi. *Proceedings of the National Academy of Sciences of the United States of America*, *107*(40), 17223–17227. https://doi.org/10.1073/pnas.1003170107

Colin, S. P., Costello, J. H., Sutherland, K. R., Gemmell, B. J., Dabiri, J. O., & Du Clos, K. T. (2020). The role of suction thrust in the metachronal paddles of swimming invertebrates. *Scientific Reports*, *10*(1), 17790. https://doi.org/10.1038/s41598-020-74745-y

Costello, J. H., Colin, S. P., Gemmell, B. J., Dabiri, J. O., & Sutherland, K. R. (2015). Multi-jet propulsion organized by clonal development in a colonial siphonophore. *Nature Communications 2015 6:1*, *6*(1), 1–6. https://doi.org/10.1038/ncomms9158

Dabiri, J. O., Bose, S., Gemmell, B. J., Colin, S. P., & Costello, J. H. (2014). An algorithm to estimate unsteady and quasi-steady pressure fields from velocity field measurements. *Journal of Experimental Biology*, *217*(3), 331–336. https://doi.org/10.1242/JEB.092767/257379/AM/AN-ALGORITHM-TO-ESTIMATE-UNSTEADY-AND-QUASI-STEADY

Dabiri, J. O., Colin, S. P., Gemmell, B. J., Lucas, K. N., Leftwich, M. C., & Costello, J. H. (2020). Jellyfish and Fish Solve the Challenges of Turning Dynamics Similarly to Achieve High Maneuverability. *Fluids 2020, Vol. 5, Page 106*, *5*(3), 106. https://doi.org/10.3390/FLUIDS5030106

Daniel, T. L. (1983). Mechanics and energetics of medusan jet propulsion. *Canadian Journal of Zoology*, *61*(6), 1406–1420. https://doi.org/10.1139/z83-190

Daniels, J., Aoki, N., Havassy, J., Katija, K., & Osborn, K. J. (2021). Metachronal Swimming with Flexible Legs: A Kinematics Analysis of the Midwater Polychaete Tomopteris. *Integrative and Comparative Biology*, *61*(5), 1658–1673. https://doi.org/10.1093/ICB/ICAB059

Dauptain, A., Favier, J., & Bottaro, A. (2008). Hydrodynamics of ciliary propulsion. *Journal of Fluids and Structures*, *24*(8), 1156–1165. https://doi.org/10.1016/j.jfluidstructs.2008.06.007

de Brouwer, A. J., de Poel, H. J., & Hofmijster, M. J. (2013). Don't Rock the Boat: How Antiphase Crew Coordination Affects Rowing. *PLoS ONE*, *8*(1), e54996. https://doi.org/10.1371/journal.pone.0054996

Dewey, P. A., Boschitsch, B. M., Moored, K. W., Stone, H. A., & Smits, A. J. (2013). Scaling laws for the thrust production of flexible pitching panels. *Journal of Fluid Mechanics*, *732*, 29–46. https://doi.org/10.1017/jfm.2013.384

Du Clos, K. T., Gemmell, B. J., Colin, S. P., Costello, J. H., Dabiri, J. O., & Sutherland, K. R. (2022). Distributed propulsion enables fast and efficient swimming modes in physonect siphonophores. *Proceedings of the National Academy of Sciences of the United States of America*, *119*(49), e2202494119. https://doi.org/10.1073/PNAS.2202494119/SUPPL_FILE/PNAS.2202494119.SAPP.PDF

Elgeti, J., & Gompper, G. (2013). Emergence of metachronal waves in cilia arrays. *Proceedings of the National Academy of Sciences of the United States of America*, *110*(12), 4470–4475. https://doi.org/10.1073/pnas.1218869110

Ellington, C. P. (1984). The aerodynamics of hovering insect flight. III. Kinematics. *Philosophical Transactions of the Royal Society of London. B, Biological Sciences*, *305*(1122), 41–78. https://doi.org/10.1098/rstb.1984.0051

Estevadeordal, J., & Goss, L. (2005, January 10). PIV with LED: Particle Shadow Velocimetry (PSV) Technique. *43rd AIAA Aerospace Sciences Meeting and Exhibit*. https://doi.org/10.2514/6.2005-37

Fish, F. E., & Nicastro, A. J. (2003). Aquatic turning performance by the whirligig beetle: constraints on maneuverability by a rigid biological system. *Journal of Experimental Biology*, *206*(10), 1649–1656. https://doi.org/10.1242/JEB.00305

Ford, M. P., Lai, H. K., Samaee, M., & Santhanakrishnan, A. (2019). Hydrodynamics of metachronal paddling: Effects of varying Reynolds number and phase lag. *Royal Society Open Science*, *6*(10). https://doi.org/10.1098/rsos.191387

Ford, M. P., & Santhanakrishnan, A. (2020). On the role of phase lag in multi-appendage metachronal swimming of euphausiids. *Bioinspiration & Biomimetics*. https://doi.org/10.1088/1748-3190/abc930

Garayev, K., & Murphy, D. W. (2021). Metachronal Swimming of Mantis Shrimp: Kinematics and Interpleopod Vortex Interactions. *Integrative and Comparative Biology*, *61*(5), 1631–1643. https://doi.org/10.1093/ICB/ICAB052

Gauger, E. M., Downton, M. T., & Stark, H. (2009). Fluid transport at low Reynolds number with magnetically actuated artificial cilia. *European Physical Journal E*, *28*(2), 231–242. https://doi.org/10.1140/epje/i2008-10388-1

Gemmell, B. J., Colin, S. P., Costello, J. H., & Sutherland, K. R. (2019). A ctenophore (comb jelly) employs vortex rebound dynamics and outperforms other gelatinous swimmers. *Royal Society Open Science*, *6*(3). https://doi.org/10.1098/rsos.181615

Gemmell, B. J., Costello, J. H., Colin, S. P., Stewart, C. J., Dabiri, J. O., Tafti, D., & Priya, S. (2013). Passive energy recapture in jellyfish contributes to propulsive advantage over other metazoans. *Proceedings of the National Academy of Sciences of the United States of America*, *110*(44), 17904–17909. https://doi.org/10.1073/PNAS.1306983110/SUPPL_FILE/SM02.AVI

Gemmell, B. J., Jiang, H., & Buskey, E. J. (2014). A new approach to micro-scale particle image velocimetry (µPIV) for quantifying flows around free-swimming zooplankton. *Journal of Plankton Research*, *36*(5), 1396–1401. https://doi.org/10.1093/plankt/fbu067

Gemmell, B. J., Troolin, D. R., Costello, J. H., Colin, S. P., & Satterlie, R. A. (2015). Control of vortex rings for manoeuvrability. *Journal of The Royal Society Interface*, *12*(108). https://doi.org/10.1098/RSIF.2015.0389

Gonzalez, R. C., Wood, R. E., & Eddins, S. L. (2004). *Digital Image Processing using MATLAB*. Pearson Prentice Hall.

Goss, L., & Estevadeordal, J. (2006). Parametric characterization for Particle-shadow Velocimetry (PSV). *Collection of Technical Papers - 25th AIAA Aerodynamic Measurement Technology and Ground Testing Conference*, *1*, 46–62. https://doi.org/10.2514/6.2006-2808

Goss, L. P., Estevadeordal, J., & Crafton, J. W. (2007). Velocity measurements near walls, cavities, and model surfaces using Particle Shadow Velocimetry (PSV). *ICIASF Record, International Congress on Instrumentation in Aerospace Simulation Facilities*. https://doi.org/10.1109/ICIASF.2007.4380874

Gough, W. T., Smith, H. J., Savoca, M. S., Czapanskiy, M. F., Fish, F. E., Potvin, J., Bierlich, K. C., Cade, D. E., Di Clemente, J., Kennedy, J., Segre, P., Stanworth, A., Weir, C., & Goldbogen, J. A. (2021). Scaling of oscillatory kinematics and Froude efficiency in baleen whales. *Journal of Experimental Biology*, *224*(13). https://doi.org/10.1242/JEB.237586/269076/AM/SCALING-OF-OSCILLATORY-KINEMATICS-AND-FROUDE

Granzier-Nakajima, S., Guy, R. D., & Zhang-Molina, C. (2020). A numerical study of metachronal propulsion at low to intermediate reynolds numbers. *Fluids*, *5*(2), 86. https://doi.org/10.3390/fluids5020086

Gu, H., Boehler, Q., Cui, H., Secchi, E., Savorana, G., De Marco, C., Gervasoni, S., Peyron, Q., Huang, T. Y., Pane, S., Hirt, A. M., Ahmed, D., & Nelson, B. J. (2020). Magnetic cilia carpets with programmable metachronal waves. *Nature Communications 2020 11:1*, *11*(1), 1–10. https://doi.org/10.1038/s41467-020-16458-4

Guo, H., & Kanso, E. (2016). Evaluating efficiency and robustness in cilia design. *Physical Review E*, *93*(3), 033119. https://doi.org/10.1103/PhysRevE.93.033119

Han, T., Mivehchi, A., Kurt, M., & Moored, K. W. (2022). Tailoring the bending pattern of non-uniformly flexible pitching hydrofoils enhances propulsive efficiency. *Bioinspiration & Biomimetics*, *17*(6), 065003. https://doi.org/10.1088/1748-3190/ac7f70

Hanasoge, S., Hesketh, P. J., & Alexeev, A. (2020). Metachronal Actuation of Microscale Magnetic Artificial Cilia. *ACS Applied Materials & Interfaces*, *12*(41), 46963–46971. https://doi.org/10.1021/acsami.0c13102

Hayashi, R., & Takagi, D. (2020). Metachronal Swimming with Rigid Arms near Boundaries. *Fluids 2020, Vol. 5, Page 24*, *5*(1), 24. https://doi.org/10.3390/FLUIDS5010024

Hedrick, T. L. (2008). Software techniques for two- and three-dimensional kinematic measurements of biological and biomimetic systems. *Bioinspiration and Biomimetics*, *3*(3), 034001. https://doi.org/10.1088/1748-3182/3/3/034001

Heimbichner Goebel, W. L., Colin, S. P., Costello, J. H., Gemmell, B. J., & Sutherland, K. R. (2020). Scaling of ctenes and consequences for swimming performance in the ctenophore *Pleurobrachia bachei*. *Invertebrate Biology*, *139*(3), e12297. https://doi.org/10.1111/ivb.12297

Hernandez-Nicaise, M.-L. (1991). Ctenophora. In *Microscopic Anatomy of Invertebrates* (pp. 359–418). Wiley-Liss, Inc.

Herrera-Amaya, A., Seber, E. K., Murphy, D. W., Patry, W. L., Knowles, T. S., Bubel, M. M., Maas, A. E., & Byron, M. L. (2021). Spatiotemporal Asymmetry in Metachronal Rowing at Intermediate Reynolds Numbers. *Integrative and Comparative Biology*, *61*(5), 1579–1593. https://doi.org/10.1093/icb/icab179

Hessenkemper, H., & Ziegenhein, T. (2018). Particle Shadow Velocimetry (PSV) in bubbly flows. *International Journal of Multiphase Flow*, *106*, 268–279. https://doi.org/10.1016/j.ijmultiphaseflow.2018.04.015

Horace, L. (1993). *Hydrodynamics* (6th ed.). Dover ublications.

Jahn, M., & Seebacher, F. (2019). Cost of transport is a repeatable trait but is not determined by mitochondrial efficiency in zebrafish (Danio rerio). *Journal of Experimental Biology*, *222*(9). https://doi.org/10.1242/JEB.201400/258945/AM/COST-OF-TRANSPORT-IS-A-REPEATABLE-TRAIT-BUT-IS-NOT

Jastrebsky, R. A., Bartol, I. K., & Krueger, P. S. (2016). Turning performance in squid and cuttlefish: Unique dual-mode, muscular hydrostatic systems. *Journal of Experimental Biology*, *219*(9), 1317–1326. https://doi.org/10.1242/jeb.126839

Jimenez, Y. E., Lucas, K. N., Long, J. H., & Tytell, E. D. (2023). Flexibility is a hidden axis of biomechanical diversity in fishes. *The Journal of Experimental Biology*, *226*(1). https://doi.org/10.1242/JEB.245308/307125

Karakas, F., D'Oliveira, D., Maas, A. E., & Murphy, D. W. (2018). Using a shell as a wing: Pairing of dissimilar appendages in atlantiid heteropod swimming. *Journal of Experimental Biology*, *221*(23). https://doi.org/10.1242/jeb.192062

Karakas, F., Maas, A. E., & Murphy, D. W. (2020). A novel cylindrical overlap-and-fling mechanism used by sea butterflies. *The Journal of Experimental Biology*, *223*(15). https://doi.org/10.1242/jeb.221499

Khodaparast, S., Borhani, N., Tagliabue, G., & Thome, J. R. (2013). A micro particle shadow velocimetry (μPSV) technique to measure flows in microchannels. In *Experiments in Fluids* (Vol. 54, Issue 2, pp. 1–13). Springer. https://doi.org/10.1007/s00348-013-1474-x

Kideys, A. E. (2002). Fall and Rise of the Black Sea Ecosystem. *Science*, *297*(5586), 1482–1484. https://science.sciencemag.org/content/297/5586/1482

Kim, D., & Gharib, M. (2011). Characteristics of vortex formation and thrust performance in drag-based paddling propulsion. *Journal of Experimental Biology*, *214*(13), 2283–2291. https://doi.org/10.1242/JEB.050716

Kiørboe, T., Jiang, H., Gonçalves, R. J., Nielsen, L. T., & Wadhwa, N. (2014). Flow disturbances generated by feeding and swimming zooplankton. *Proceedings of the National Academy of*

Sciences of the United States of America, *111*(32), 11738–11743. https://doi.org/10.1073/pnas.1405260111

Koutsiaris, A. G. (2012). Digital Micro PIV (μPIV) and Velocity Profiles In Vitro and In Vivo. In *The Particle Image Velocimetry - Characteristics, Limits and Possible Applications*. InTech. https://doi.org/10.5772/36724

Kreps, T. A., Purcell, J. E., & Heidelberg, K. B. (1997). Escape of the ctenophore Mnemiopsis leidyi from the scyphomedusa predator Chrysaora quinquecirrha. *Marine Biology 1997 128:3*, *128*(3), 441–446. https://doi.org/10.1007/S002270050110

Kurt, M., Mivehchi, A., & Moored, K. (2021). High-Efficiency Can Be Achieved for Non-Uniformly Flexible Pitching Hydrofoils via Tailored Collective Interactions. *Fluids*, *6*(7), 233. https://doi.org/10.3390/fluids6070233

Larson, M., Kiger, K. T., Abdelaziz, K., & Balaras, E. (2014). Effect of metachronal phasing on the pumping efficiency of oscillating plate arrays. *Experiments in Fluids 2014 55:5*, *55*(5), 1–13. https://doi.org/10.1007/S00348-014-1741-5

Li, Y., Shen, X.-X., Evans, B., Dunn, C. W., & Rokas, A. (2020). Rooting the animal tree of life. *BioRxiv*, 2020.10.27.357798. https://doi.org/10.1101/2020.10.27.357798

Lighthill, M. J. (1960). Note on the swimming of slender fish. *Journal of Fluid Mechanics*, *9*(2), 305–317. https://doi.org/10.1017/S0022112060001110

Lim, D., Lahooti, M., & Kim, D. (2019a). Inertia-driven flow symmetry breaking by oscillating plates. *AIP Advances*, *9*(10), 105119. https://doi.org/10.1063/1.5122966/1.5122966.MM.ORIGINAL.V2.AVI

Lim, D., Lahooti, M., & Kim, D. (2019b). Inertia-driven flow symmetry breaking by oscillating plates. *AIP Advances*, *9*(10), 105119. https://doi.org/10.1063/1.5122966

Lim, J. L., & DeMont, M. E. (2009). Kinematics, hydrodynamics and force production of pleopods suggest jet-assisted walking in the american lobster (homarus americanus). *Journal of Experimental Biology*, *212*(17), 2731–2745. https://doi.org/10.1242/jeb.026922

Lionetti, S., Lou Zhipeng, Herrera-Amaya, A., Byron, M. L., & Li, C. (n.d.). A new propulsion enhancement mechanism in metachronal rowing at intermediate Reynolds numbers. *Journal of Fluid Mechanics (Under Review)*.

Liu, C. (2007). Micromachined biomimetic artificial haircell sensors. *Bioinspiration and Biomimetics*, *2*(4), S162. https://doi.org/10.1088/1748-3182/2/4/S05

Liu, Y., Lozano, A. D., Hedrick, T. L., & Li, C. (2021). Comparison of experimental and numerical studies on the flow structures of hovering hawkmoths. *Journal of Fluids and Structures*, *107*, 103405. https://doi.org/10.1016/J.JFLUIDSTRUCTS.2021.103405

Loth, E. (2008). Drag of non-spherical solid particles of regular and irregular shape. *Powder Technology*, *182*(3), 342–353. https://doi.org/10.1016/j.powtec.2007.06.001

Lucas, K. N., Dabiri, J. O., & Lauder, G. V. (2017). A pressure-based force and torque prediction technique for the study of fish-like swimming. *PLOS ONE*, *12*(12), e0189225. https://doi.org/10.1371/journal.pone.0189225

Mackie, G. O., Mills, C. E., & Singla, C. L. (1992). Giant Axons and Escape Swimming in Euplokamis dunlapae (Ctenophora: Cydippida) . *The Biological Bulletin*, *182*(2), 248–256. https://doi.org/10.2307/1542118

Marais, C., Thiria, B., Wesfreid, J. E., & Godoy-Diana, R. (2012). Stabilizing effect of flexibility in the wake of a flapping foil. *Journal of Fluid Mechanics*, *710*, 659–669. https://doi.org/10.1017/jfm.2012.390

Matsumoto, G. I. (1991). Swimming movements of ctenophores, and the mechanics of propulsion by ctene rows. *Hydrobiologia*, *216–217*(1), 319–325. https://doi.org/10.1007/BF00026481

Mchenry, M. J., Pell, C. A., & Long, J. H. (1995). Mechanical Control Of Swimming Speed: Stiffness And Axial Wave Form In Undulating Fish Models. *Journal of Experimental Biology*, *198*(11), 2293–2305. https://doi.org/10.1242/JEB.198.11.2293

Milana, E., Gorissen, B., De Borre, E., Ceyssens, F., Reynaerts, D., & De Volder, M. (2023). Out-of-Plane Soft Lithography for Soft Pneumatic Microactuator Arrays. *Soft Robotics*, *10*(1), 197–204. https://doi.org/10.1089/soro.2021.0106

Milana, E., Zhang, R., Vetrano, M. R., Peerlinck, S., de Volder, M., Onck, P. R., Reynaerts, D., & Gorissen, B. (2020). Metachronal patterns in artificial cilia for low Reynolds number fluid propulsion. *Science Advances*, *6*(49). https://doi.org/10.1126/SCIADV.ABD2508/SUPPL_FILE/ABD2508_SM.PDF

Moroz, L. L., Kocot, K. M., Citarella, M. R., Dosung, S., Norekian, T. P., Povolotskaya, I. S., Grigorenko, A. P., Dailey, C., Berezikov, E., Buckley, K. M., Ptitsyn, A., Reshetov, D., Mukherjee, K., Moroz, T. P., Bobkova, Y., Yu, F., Kapitonov, V. V., Jurka, J., Bobkov, Y. V., … Kohn, A. B. (2014). The ctenophore genome and the evolutionary origins of neural systems. *Nature*, *510*(7503), 109–114. https://doi.org/10.1038/nature13400

Morris, S. G. (1996). Middle Cambrian ctenophores from the Stephen Formation, British Columbia, Canada. *Philosophical Transactions of the Royal Society of London. Series B: Biological Sciences*, *351*(1337), 279–308. https://doi.org/10.1098/RSTB.1996.0024

Murphy, D. W., Adhikari, D., Webster, D. R., & Yen, J. (2016). Underwater flight by the planktonic sea butterfly. *Journal of Experimental Biology*, *219*(4), 535–543. https://doi.org/10.1242/JEB.129205

Murphy, D. W., Webster, D. R., Kawaguchi, S., King, R., & Yen, J. (2011). Metachronal swimming in Antarctic krill: gait kinematics and system design. *Marine Biology*, *158*(11), 2541–2554. https://doi.org/10.1007/s00227-011-1755-y

Murphy, D. W., Webster, D. R., & Yen, J. (2013). The hydrodynamics of hovering in Antarctic krill. *Limnology and Oceanography: Fluids and Environments*, *3*(1), 240–255. https://doi.org/10.1215/21573689-2401713

Niimoto, K. T. M., Kuball, K. J., Block, L. N., Lenz, P. H., & Takagi, D. (2020). Rotational Maneuvers of Copepod Nauplii at Low Reynolds Number. *Fluids 2020, Vol. 5, Page 78*, *5*(2), 78. https://doi.org/10.3390/FLUIDS5020078

Norberg, U., & Rayner, J. M. V. (1987). Ecological morphology and flight in bats (Mammalia; Chiroptera): wing adaptations, flight performance, foraging strategy and echolocation. *Philosophical Transactions of the Royal Society of London. B, Biological Sciences*, *316*(1179), 335–427. https://doi.org/10.1098/RSTB.1987.0030

Olsen, M. G., & Adrian, R. J. (2000). Out-of-focus effects on particle image visibility and correlation in microscopic particle image velocimetry. *Experiments in Fluids*, *29*(7), S166–S174. https://doi.org/10.1007/s003480070018

Ovryn, B., & Izen, S. H. (2000). Imaging of transparent spheres through a planar interface using a high-numerical-aperture optical microscope. *Journal of the Optical Society of America A*, *17*(7), 1202. https://doi.org/10.1364/josaa.17.001202

Park, H., Park, Y.-J., Lee, B., Cho, K.-J., & Choi, H. (2016). Vortical structures around a flexible oscillating panel for maximum thrust in a quiescent fluid. *Journal of Fluids and Structures*, *67*, 241–260. https://doi.org/10.1016/j.jfluidstructs.2016.10.004

Purcell, E. M. (1977). Life at low Reynolds number. *American Journal of Physics*, *45*(1), 3–11. https://doi.org/10.1119/1.10903

Quinn, D. B., Lauder, G. V., & Smits, A. J. (2014). Scaling the propulsive performance of heaving flexible panels. *Journal of Fluid Mechanics*, *738*, 250–267. https://doi.org/10.1017/jfm.2013.597

Raffel, M., Willert, C. E., Scarano, F., Kähler, C. J., Wereley, S. T., & Kompenhans, J. (2018). *Particle Image Velocimetry: A Practical Guide*. Springer International Publishing. https://doi.org/10.1007/978-3-319-68852-7

Ren, Z., Zhang, M., Song, S., Liu, Z., Hong, C., Wang, T., Dong, X., Hu, W., & Sitti, M. (2022). Soft-robotic ciliated epidermis for reconfigurable coordinated fluid manipulation. *Science Advances*, *8*(34). https://doi.org/10.1126/SCIADV.ABQ2345/SUPPL_FILE/SCIADV.ABQ2345_MOVIES_S1_TO_S7.ZIP

Rockenbach, A., Mikulich, V., Brücker, C., & Schnakenberg, U. (2015). Fluid transport via pneumatically actuated waves on a ciliated wall. *Journal of Micromechanics and Microengineering*, *25*(12), 125009. https://doi.org/10.1088/0960-1317/25/12/125009

Rockenbach, A., & Schnakenberg, U. (2017). The influence of flap inclination angle on fluid transport at ciliated walls. *Journal of Micromechanics and Microengineering*, *27*(1), 015007. https://doi.org/10.1088/0960-1317/27/1/015007

Ruszczyk, M., Webster, D. R., & Yen, J. (2022). Trends in Stroke Kinematics, Reynolds Number, and Swimming Mode in Shrimp-Like Organisms. *Integrative and Comparative Biology*, *00*(0), 1–14. https://doi.org/10.1093/ICB/ICAC067

Saffaraval, F., & Goudarzi, N. (2021). Effects of symmetry breaking in the viscous pumping of an oscillating plate in the intermediate Reynolds numbers. *Bioinspiration and Biomimetics*, *16*(2), 26001. https://doi.org/10.1088/1748-3190/abbdcb

Santiago, J. G., Wereley, S. T., Meinhart, C. D., Beebe, D. J., & Adrian, R. J. (1998). A particle image velocimetry system for microfluidics. *Experiments in Fluids 1998 25:4*, *25*(4), 316–319. https://doi.org/10.1007/S003480050235

Santos, S. O., Cuenca-Jiménez, F., Gomez-Valdez, P. A., Morales-Lopez, O., & Wilhelmus, M. M. (2022). *RoboKrill : a metachronal drag-based swimmer robot*. http://arxiv.org/abs/2202.01037

Sareh, S., Rossiter, J., Conn, A., Drescher, K., & Goldstein, R. E. (2013). Swimming like algae: Biomimetic soft artificial cilia. *Journal of the Royal Society Interface*, *10*(78). https://doi.org/10.1098/rsif.2012.0666

Schaub, H., & Junkins, J. L. (2018). Analytical Mechanics of Space Systems, Fourth Edition. *Analytical Mechanics of Space Systems, Fourth Edition*. https://doi.org/10.2514/4.105210

Schultz, D. T., Haddock, S. H. D., Bredeson, J. V., Green, R. E., Simakov, O., & Rokhsar, D. S. (2023). Ancient gene linkages support ctenophores as sister to other animals. *Nature*. https://doi.org/10.1038/s41586-023-05936-6

Semati, A., Amani, E., Saffaraval, F., & Saffar-Avval, M. (2020a). Numerical simulation of oscillating plates at the visco-inertial regime for bio-inspired pumping and mixing applications. *Physics of Fluids*, *32*(10), 101906. https://doi.org/10.1063/5.0023539

Semati, A., Amani, E., Saffaraval, F., & Saffar-Avval, M. (2020b). Numerical simulation of oscillating plates at the visco-inertial regime for bio-inspired pumping and mixing applications. *Physics of Fluids*, *32*(10), 101906. https://doi.org/10.1063/5.0023539

SENSENIG, A. T., KIGER, K. T., & SHULTZ, J. W. (2009). The rowing-to-flapping transition: ontogenetic changes in gill-plate kinematics in the nymphal mayfly Centroptilum triangulifer (Ephemeroptera, Baetidae). *Biological Journal of the Linnean Society*, *98*(3), 540–555. https://doi.org/10.1111/j.1095-8312.2009.01314.x

Sensenig, A. T., Kiger, K. T., & Shultz, J. W. (2010). Hydrodynamic pumping by serial gill arrays in the mayfly nymph *Centroptilum triangulifer*. *Journal of Experimental Biology*, *213*(19), 3319–3331. https://doi.org/10.1242/jeb.039271

Shavit, U., Lowe, R. J., & Steinbuck, J. V. (2006). Intensity Capping: a simple method to improve cross-correlation PIV results. *Experiments in Fluids 2006 42:2*, *42*(2), 225–240. https://doi.org/10.1007/S00348-006-0233-7

Shiganova, T. A., Mirzoyan, Z. A., Studenikina, E. A., Volovik, S. P., Siokou-Frangou, I., Zervoudaki, S., Christou, E. D., Skirta, A. Y., & Dumont, H. J. (2001). Population development of the invader ctenophore Mnemiopsis leidyi, in the Black Sea and in other seas of the Mediterranean basin. *Marine Biology*, *139*(3), 431–445. https://doi.org/10.1007/s002270100554

Shih, C. C., & Buchanan, H. J. (1971). The drag on oscillating flat plates in liquids at low Reynolds numbers. *Journal of Fluid Mechanics*, *48*(2), 229–239. https://doi.org/10.1017/S0022112071001563

Sitti, M. (2018). Miniature soft robots - road to the clinic. In *Nature Reviews Materials* (Vol. 3, Issue 6, pp. 74–75). Nature Publishing Group. https://doi.org/10.1038/s41578-018-0001-3

Snyder, J. B., Nelson, M. E., Burdick, J. W., & MacIver, M. A. (2007). Omnidirectional Sensory and Motor Volumes in Electric Fish. *PLOS Biology*, *5*(11), e301. https://doi.org/10.1371/JOURNAL.PBIO.0050301

Sutherland, K. R., Costello, J. H., Colin, S. P., & Dabiri, J. O. (2014). Ambient fluid motions influence swimming and feeding by the ctenophore Mnemiopsis leidyi. *Journal of Plankton Research*, *36*(5), 1310–1322. https://doi.org/10.1093/plankt/fbu051

Sutherland, K. R., Gemmell, B. J., Colin, S. P., & Costello, J. H. (2019). Maneuvering Performance in the Colonial Siphonophore, Nanomia bijuga. *Biomimetics*, *4*(3), 62. https://doi.org/10.3390/biomimetics4030062

Svendsen, J. C., Banet, A. I., Christensen, R. H. B., Steffensen, J. F., & Aarestrup, K. (2013). Effects of intraspecific variation in reproductive traits, pectoral fin use and burst swimming on metabolic rates and swimming performance: a study on the Trinidadian guppy (*Poecilia reticulata* Peters). *Journal of Experimental Biology*. https://doi.org/10.1242/jeb.083089

Tack, N. B., & Gemmell, B. J. (2022). A tale of two fish tails: does a forked tail really perform better than a truncate tail when cruising? *Journal of Experimental Biology*, *225*(22). https://doi.org/10.1242/jeb.244967

Takagi, D. (2015). Swimming with stiff legs at low Reynolds number. *Physical Review E - Statistical, Nonlinear, and Soft Matter Physics*, *92*(2), 023020. https://doi.org/10.1103/PhysRevE.92.023020

Tamm, S. L. (1980). Cilia and Ctenophores. *Oceanus*, *23*(2), 50–59.

Tamm, S. L. (2014). Cilia and the life of ctenophores. *Invertebrate Biology*, *133*(1), 1–46. https://doi.org/10.1111/ivb.12042

Thielicke, W., & Stamhuis, E. J. (2014). PIVlab – Towards User-friendly, Affordable and Accurate Digital Particle Image Velocimetry in MATLAB. *Journal of Open Research Software*, *2*(1). https://doi.org/10.5334/jors.bl

Toonder, J. M. J. den, & Onck, P. R. (2013). Microfluidic manipulation with artificial/bioinspired cilia. In *Trends in Biotechnology* (Vol. 31, Issue 2, pp. 85–91). Elsevier Current Trends. https://doi.org/10.1016/j.tibtech.2012.11.005

Truong, C., Harris, J., & McPhail, M. J. (2018, January 8). The effect of out-of-plane shear within the depth of correlation in macroscopic planar particle shadow velocimetry. *2018 AIAA Aerospace Sciences Meeting*. https://doi.org/10.2514/6.2018-2035

van de Hulst, H. C. (1957). *Ligth Scattering by Small Particles*. Wiley.

Vogel, S. (1994). *Life in Moving Fluids* (Second). Princenton university Press.

Walker, J. A. (2000). Does a rigid body limit maneuverability? *Journal of Experimental Biology*, *203*(22), 3391–3396. https://doi.org/10.1242/jeb.203.22.3391

Walker, J. A., & Westneat, M. W. (2000). Mechanical performance of aquatic rowing and flying. *Proceedings of the Royal Society B: Biological Sciences*, *267*(1455), 1875–1881. https://doi.org/10.1098/rspb.2000.1224

Webb, P. W. (1994). The biology of fish swimming. *The Mechanics and Physiology of Animal Swimming*, 45–62. https://doi.org/10.1017/CBO9780511983641.005

Webb, P. W., & Fairchild, A. G. (2001). Performance and maneuverability of three species of teleostean fishes. *Canadian Journal of Zoology*, *79*(10), 1866–1877. https://doi.org/10.1139/z01-146

Whelan, N. V., Kocot, K. M., Moroz, T. P., Mukherjee, K., Williams, P., Paulay, G., Moroz, L. L., & Halanych, K. M. (2017). Ctenophore relationships and their placement as the sister group to all other animals. *Nature Ecology and Evolution*, *1*(11), 1737–1746. https://doi.org/10.1038/s41559-017-0331-3

Xu, N., & Dabiri, J. (2022). Bio-Inspired Ocean Exploration. *Oceanography*, 35–48. https://doi.org/10.5670/oceanog.2022.214

Zastawny, M., Mallouppas, G., Zhao, F., & van Wachem, B. (2012). Derivation of drag and lift force and torque coefficients for non-spherical particles in flows. *International Journal of Multiphase Flow*, *39*, 227–239. https://doi.org/10.1016/J.IJMULTIPHASEFLOW.2011.09.004

Zhang, C., Guy, R. D., Mulloney, B., Zhang, Q., & Lewis, T. J. (2014). Neural mechanism of optimal limb coordination in crustacean swimming. *Proceedings of the National Academy of Sciences of the United States of America*, *111*(38), 13840–13845. https://doi.org/10.1073/pnas.1323208111

Zhang, R., den Toonder, J., & Onck, P. R. (2021). Transport and mixing by metachronal waves in nonreciprocal soft robotic pneumatic artificial cilia at low Reynolds numbers. *Physics of Fluids*, *33*(9), 92009. https://doi.org/10.1063/5.0054929/1064330

VITA

Adrian Herrera-Amaya

EDUCATION

Pennsylvania State University

Ph D., Department of Mechanical Engineering 2018- 2023

University of Guanajuato (Mexico)

M.S., Department of Mechanical Engineering 2015-2017
University of Guanajuato (Mexico)

B.S.E., Department of Mechanical Engineering 2010-2015

PEER-REVIEWED JOURNAL PUBLICATIONS

Herrera-Amaya, A., Seber, E. K., Murphy, D. W, Patry, W. L., Knowles, T.S, Bubel, M. M., Mass, A. E., & Byron, M. L. (2021). Spatiotemporal Asymmetry in Metachronal Rowing at Intermediate Reynolds Numbers. *Integrative and Comparative Biology*, 61(5), 1-15. https://doi.org/10.1093/ICB/ICAB179

Lara-Castro, M., **Herrera-Amaya, A**., Escarola-Rosas, M. A., Vázquez-Toledo, M., López-Huerta, F., Aguilera-Cortés, L.A, & Herrera-May, A.L. (2017). Design and modeling of polysilicon electrothermal actuators for a MEMS mirror with low power consumption. *Micromachines*, 8(7). https://doi.org/10.3390/mi8070203

MANUSCRIPTS IN PREPARATION, SUBMITED, AND UNDER REVIEW

Lionetti, S., Lou, Z., **Herrera-Amaya, A.,** Byron, M. L, & Li, C. Vortex dynamics and propulsion enhancement mechanism in metachronal rowing at intermediate Reynolds numbers. (UNDER REVIEW).

Herrera-Amaya, A., & Byron, M. L. Metachronal coordination enables omnidirectional swimming via spatially distributed propulsion. (UNDER REVIEW).
bioRxiv 2023.01.23.525300; doi: https://doi.org/10.1101/2023.01.23.525300

Herrera-Amaya, A., & Byron, M. L. Performance evaluation of a flexible appendage for metachronal rowing at intermediate Reynolds numbers. (IN PREP)

PEER-REVIEWED CONFERENCE PUBLICATIONS

Lou, Z., **Herrera-Amaya, A.,** Byron, M. L, & Li, C. (2022). Hydrodynamics of Metachronal Motion: Effects of Spatial Asymmetry on the Flow Interaction Between Adjacent Appendages. *Proceedings of the ASME/FEDSM 2022*. Toronto, August 3-5, 2022.